# Theoretical Understanding and Design of Supported Metal Heterogeneous Nanocatalysts

**MIAO ZHOU**

*(B.Sc., Chongqing University)*

**A THESIS SUBMITTED**

**FOR THE DEGREE OF DOCTOR OF PHILOSOPHY**

**DEPARTMENT OF PHYSICS**

**NATIONAL UNIVERSITY OF SINGAPORE**

**2012**

# Acknowledgements

I would like to thank my supervisors, **Prof. Feng Yuan Ping** and **Dr. Zhang Chun** for giving me the opportunity to explore my research interests and the guidance throughout my research during the past years. Prof. Feng and Dr. Zhang have provided a lot of help and suggestions on my study, work, and life. I feel the support and encourage from them from many aspects. It is a great experience for me to do research under their instructions and it is also a precious treasure for me in my future research career.

I owe my deep gratitude to Dr. Zhang Aihua, Dr. Lu Yunhao for helping me in my early stage of research. It is a pleasure to thank the previous and current group members in S13-04-13, Dr. Yang Ming, Dr. Shen Lei, Dr. Cai Yongqing, Dr. Argo Nurbawono, Dr. Zeng Minggng, Dr. Wu Rongqin, Dr. Sha Zhengdong, Dr. Dai Zhenxiang, Dr. Yang Kesong, Dr. He Aling, Mr. Bai Zhaoqiang, Mr. Wu Qingyun, Ms. Li Shuchun, Ms. Chintalapati Sandhya, Ms. Qin Xian, Ms. Linhu Jiajun for their help and valuable discussion.

I would also like to thank my parents, relatives and friends. Particularly, I express my deepest appreciation to my parents, for their everlasting support, tolerance, and love, and my elderly sister, Madam Zhou Xian, for being nice and enlightening with me since childhood.

# Table of Contents

# Abstract

Nanocatalysis, an exciting subfield of nanoscience, is a subject of outmost importance in present days, due to its great potential in modern manufacture of chemical products, and also in other fields such as pollution and environment control. Among various kinds of nanocatalysts, metal clusters supported on a substrate are particularly interesting in the context of heterogeneous catalysis, for which the interaction between the reactive center and the underlying substrate plays an essential role in the catalytic performance of supported clusters. Current research in controlling the catalytic activity of these catalysts has been focused on tuning the size, dimensionality, charging state of supported metal clusters, and/or the thickness, morphology, chemical composition of the underlying substrate. Despite the great sophistication achieved by many experimental techniques used in catalyst studies, it is still difficult, and sometimes impossible, to obtain a precise picture of the catalysts under operating conditions and the catalyzed reaction mechanisms at an atomic level, without any theoretical support. In this thesis, quantum mechanical calculations were carried out to illustrate and discuss the subject of nanocatalysis, to show how some basic concepts in physics, chemistry and material sciences can be employed to understand and design new catalysts, and to find novel and practical methodologies to control their catalytic performance.

Our first proposal was to control the physical and chemical properties of supported gold nanocatalysts by metal-insulator transition (MIT) in transition metal (TM) oxide substrate. TM oxides are normally insulating with a definite bandgap and MIT in oxides, an important concept in condensed matter physics, is often discussed outside the field of catalysis chemistry. For the first time, we showed that MIT in $SrTiO_3$ substrate driven by Nb-doping has strong effects on the adsorption of metal clusters, leading to a dimensionality crossover of the lowest-energy state of the supported Au cluster (from the 3-dimensional structure to a planar one), and at the same time, greatly enhances the stability and catalytic activity of these clusters. In view of the most recent experimental progress on initiating MIT in oxides, our findings pave a practical methodology to control the structural, morphology, electronic and catalytic properties of TM-oxide supported metal nanoclusters.

Secondly, we proposed to control the stabilization and catalytic capability of graphene-supported metal nanoclusters by applying mechanical strain in the substrate. Graphene, a 2D network of conjugated carbon atoms, has excellent mechanical properties that a tensile strain up to 15% can be introduced in experiments. Our results revealed that the applied strain can increase the adsorption energies of various kinds of metal clusters on graphene, which is highly desired for the durability of catalysts in practical applications. The charging state of those clusters can be efficiently tuned by applying strain in the graphene substrate and interestingly, with the adsorption of gold clusters, even the p-type or n-type doping of graphene can be controlled. We also investigated the strain effects on the catalytic performance of those supported clusters, and results showed that the reaction barrier for catalyzed CO oxidation can be greatly reduced by strain, thus

providing new opportunities for the future development of supported metal nanocatalysts.

In addition, the effects of defects in graphene on supported nanocatalysts were also investigated and it was found that defects play an essential role in the anchoring and activating of supported metal clusters. The simplest single-carbon-vacancy defect was found to strongly adsorb Au and Pt clusters due to the hybridization of carbon 2p and Au/Pt 5d orbitals. Compared to the cases of pristine graphene, defective graphene supported metal clusters have enhanced catalytic activity towards $O_2$ molecule. Further calculations showed that CO oxidation can occur at a very low barrier ($< 0.2$ eV). Similar effects are also expected to exist in other types of defects in graphene, such as multiple carbon vacancies, topological line defects and grain boundaries. Results presented are helpful to explain and understand the experimentally observed high electrocatalytic activity of Pt nanoclusters supported on graphene, owing to the fact that defects are always inevitable during graphene fabrication.

On the way to search for high-performance nanocatalysts with low-cost, we explored the use of single metal atom embedded graphene as a possible single-atom nanocatalyst. The geometrical, electronic and magnetic properties of small gas molecules adsorption on pristine and various transition-metal embedded graphene have been systematically investigated and discussed. Our analysis suggested that the reactivity of graphene can be increased in general by embedding metal elements, and among all the metal atoms studied, Ti and Au may be the best choices towards molecular $O_2$ activation due to the largest expansion of O-O bond and charge transfer upon $O_2$ adsorption. By using Au-embedded graphene as model catalyst system and CO oxidation as a benchmark probe, we examined the reaction mechanism of CO oxidation to gain a better understanding

of this system. Calculations illustrated that the reaction is most likely to proceed with Langmuir-Hinshelwood mechanism followed by Eley-Rideal reaction, with a reaction barrier around 0.3 eV. These findings may shed light on the great potential of using metal-embedded graphene as a possible single-atom nanocatalyst, as well as in other fields such as graphene-based gas sensing and spintronics.

# Publications

[1] **M. Zhou**, Y. P. Feng, and C. Zhang, "Gold clusters on Nb-doped $SrTiO_3$: Effects of Metal-insulator Transition on Heterogeneous Au Nanocatalysis", *Phys. Chem. Chem. Phys.* 14, 9660, (2012).

[2] **M. Zhou**, Y. H. Lu, C. Zhang, and Y. P. Feng, "Adsorption of gas molecules on transition metal-embedded graphene: A search for high-performance graphene-based catalysts and gas sensors", *Nanotechnology* 22, 385502, (2011).

[3] **M. Zhou**, A. H. Zhang, Z. X. Dai, Y. P. Feng, and C. Zhang, "Strain-Enhanced Stabilization and Catalytic Activity of Metal Nanoclusters on Graphene", *J. Phys. Chem. C.* 114, 16541, (2010).

[4] **M. Zhou**, A. H. Zhang, Z. X. Dai, C. Zhang, and Y. P. Feng, "Greatly enhanced adsorption and catalytic activity of Au and Pt clusters on defective graphene", *J. Chem. Phys.* 132, 194704, (2010).

[5] **M. Zhou**, Y. H. Lu, C. Zhang, and Y. P. Feng, "Strain effects on hydrogen storage capability of metal-decorated graphene: A first-principles study", *Appl. Phys.* Lett. 97, 103109, (2010).

[6] **M. Zhou**, Y. Q. Cai, M. G. Zeng, C. Zhang, and Y. P. Feng, "Mn-doped thiolated

$Au_{25}$ nanoclusters: Atomic configuration, magnetic properties, and a possible high-performance spin filter", *Appl. Phys. Lett.* 98, 143103, (2011).

[7] **M. Zhou**, R. Z. Hou, A. H. Zhang, A. Nurbawono, Z. S. Wang, Y. P. Feng, and C. Zhang, "Electric field control of smallest single molecular motor on Ag (100) surface", *manuscript in preparation*.

[8] Y. H. Lu, **M. Zhou**, C. Zhang, and Y. P. Feng, "Metal-Embedded Graphene: A Possible Catalyst with High Activity", *J. Phys. Chem. C.* 113, 20156, (2009).

[9] Y. Q. Cai, **M. Zhou**, M. G. Zeng, C. Zhang, and Y. P. Feng, "Adsorbate and defect effects on electronic and transport properties of gold nanotubes", *Nanotechnology* 22, 215702, (2011).

[10] M. Yang, **M. Zhou**, A. H. Zhang and C. Zhang, "Graphene Oxide: An Ideal Support for Gold Nanocatalysts", *J. Phys. Chem. C.* 116, 22336, (2012).

[11] T. C. Niu, **M. Zhou**, J. L. Zhang, Y. P. Feng, and W. Chen, "Dipole Orientation Dependent Symmetry Reduction of Chloroaluminum Phthalocyanine on Cu(111)", *submitted*.

[12] M. G. Zeng, L. Shen, **M. Zhou**, C. Zhang, and Y. P. Feng, "Graphene-based bipolar spin diode and spin transistor: Rectification and amplification of spin-polarized current", *Phys. Rev. B* 83, 115427, (2011).

[13] Z. Q. Wang, R. G. Xie, M. Zhou, Y. P. Feng, B. W. Li, and J. T. L. Thong, "Reversible Doping of Graphene by Electrically-Controlled Gas Adsorption", *submitted*.

[14] Z. X. Dai, A. Nurbawono, A. H. Zhang, **M. Zhou**, Y. P. Feng, G. W. Ho, C. Zhang, "C-doped ZnO nanowires: Electronic structures, magnetic properties, and a possible

spintronic device", *J. Chem. Phys* 134, 104706, (2011).

[15] Y. H. Wu, Y. Wang, J. Y. Wang, **M. Zhou**, A. H. Zhang, C. Zhang, Y. J. Yang, Y. N. Hua, B. X. Xu, "Electrical transport across metal/two-dimensional carbon junctions: Edge versus side contacts", *AIP ADVANCES* 2, 012132, (2011).

# Abbreviations

| | |
|---|---|
| DFT | Density Functional Theory |
| USPP | ultra-soft pseudopotential |
| PAW | Projector Augmented-Wave |
| LDA | Local Density Approximation |
| GGA | Generalized Gradient Approximation |
| PBE | Perdew-Burke-Ernzerhof |
| VASP | Vienna Ab-initio Simulation Package |
| MEP | minimum energy path |
| NEB | Nudged Elastic Band |
| MIT | Metal-insulator Transition |
| DOS | Density of States |
| HOMO | Highest Occupied Molecular Orbital |
| LUMO | Lowest Unoccupied Molecular Orbital |
| LH | Langmuir-Hinshelwood |
| ER | Eley-Rideal |
| h.c. | hermitian conjugate |

# List of Tables

# List of Figures

# Chapter 1

# Introduction

Human beings are curious to study the unknown. For centuries, scientific and technological research efforts have been made both to gain fundamental knowledge about the unknown and to develop an application out of the unknown. For the subjects of interest which are generally complex, one point of view is often insufficient, and a multidisciplinary approach will give a more profound understanding. One typical example is the field of catalysis, which involves the utilization of knowledge from various disciplines, including physics, chemistry, material science, chemical engineering, among many others. Heterogeneous catalysts, of which the phase of catalyst differs from that of the reactants, play an essential role in modern chemical industry, as well as in pollution and environmental control. Metals have been widely used in catalysts on a large scale for many important processes such as the refining of petroleum, hydrogenation of fats, and conversion of automobile exhaust. However, metals (often from the transition series) used are usually expensive and may constitute only around 1 wt% of the

catalytic materials. For practical use, they are applied in a finely dispersed form as particles on a support (carrier), and the majority of the reactions take place at these active sites. The efficiency of such catalytic process is thus largely determined by the quality of the catalysts fabricated, such as the surface area of active sites and the stability. With the advancement of nanoscience and nanotechnology, these metal particles now enter the "nano" scale, where phenomena length scales become comparable to the size of the structure. Consequently, novel physical, chemical and electronic properties of these nanomaterials have been discovered and investigated. In the field of nanocatalysis, the catalytic performance of metal nanoclusters is often controlled by quantum size effects owing to the reduced dimensions of these structures, in contrast with the conventional catalysts at larger sizes. These unique properties of metal nanoparticles that cannot be extrapolated or deduced through scaling arguments from knowledge of these properties in the bulk limit, present new opportunities for the search of new catalysts. In the following sections, we will review in detail the previous multi- and inter-disciplinary research work on supported-metal nanoparticles in heterogeneous catalysis.

## 1.1 Green chemistry–Environmental-friendly catalysis

In a catalytic process, the rate of a chemical reaction is increased by a catalyst without the consumption of the catalyst itself, as was stated by Berzelius over 150 years ago. The exploration of catalysis has been developed continuously and led to wide-spread applications in people's daily life. Industrial production relies crucially on catalysts, and catalysis is becoming increasingly important in energy production and pollution

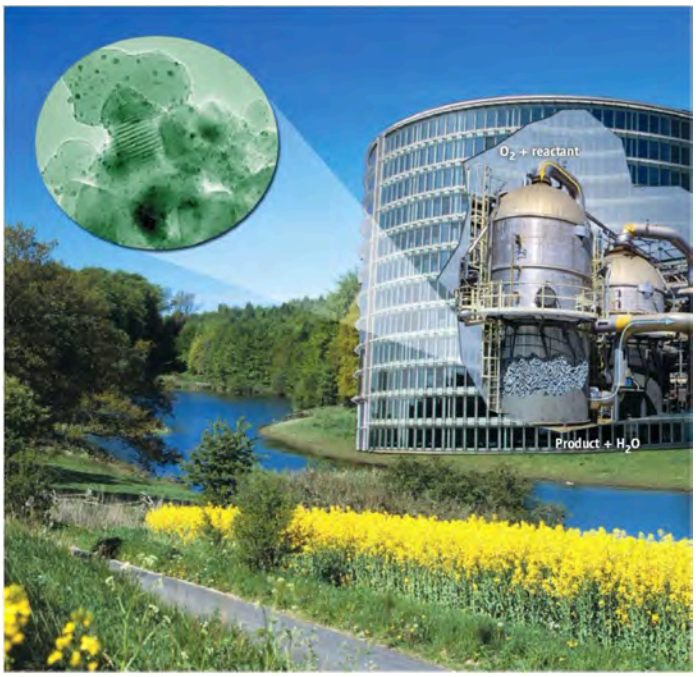


Figure 1.1: Green chemistry. The ultimate green catalytic oxidation process uses atmospheric air as the oxidant and forms water as the only by-product. Reprinted with permission from Ref.[5]

control.[1] However, in the last decades, it has become obvious that the practice of industrial chemistry has some strong drawbacks, aside from the desired products. These are severe environmental "costs", and affect the sustainable development of human society. In recognition of the environmental effects of the chemical industry, many laws have been passed and implemented all over the world to regulate chemical processes and products.

The term "Green Chemistry" was coined in the early 1990s by Anastas[2] and colleagues of the US Environmental Protrction Agency (EPA). In 1993 the EPA officially adopted the name "US Green Chemistry Program" which has served as a focal point

for activities in United States, and the guiding principle is *benign by design* of both products and processes.[3] The essence of green chemistry can be reduced to a working definition: Green chemistry efficiently utilizes (preferably renewable) raw materials, eliminates wastes and avoid the use of toxic and/or hazardous reagents and solvents in the manufacture and application of chemical products (see Fig. 1.1).[4, 5] As green chemistry is a philosophy that puts forward sustainable concepts, advanced catalysts, whether heterogeneous/homogeneous catalysts or enzyme are searched for a long time to address this problem.

In heterogeneous catalysis, in which the phase of the reactants/products (gaseous or liquid) and of the catalyst (usually solid) is different, the ease separation of the reaction products from the catalyst makes heterogeneous catalyst an advantage over its homogeneous counterpart.[7] In the industrial world, heterogeneous catalysis alone has been estimated to be a prerequisite for more than 20% of all production.[8] In the efforts to develop a more sustainable chemical industry, there is an urgent need to study and develop more efficient heterogeneous catalysts with supreme activity, selectivity, stability and with nontoxic nature.

## 1.2 Supported metals in nanocatalysts

An important group of heterogeneous catalysts is the group of supported metal catalysts, generally containing small metal particles dispersed over a porous substrate. The substrate, or in industrial terms, the *carrier* is expected to meet several requirements, such as exposing a high surface area, exhibiting high mechanical and thermal resistance.

Transition metal particles, especially the VIII group metals (Fe, Co, Ni, Ru, Rh, Pd, Os, Ir, and Pt) and noble group metals (Cu, Ag, Au), are of particular importance, as they catalyze oxidation, (de)hydrogenation, cyclization, isomerization, among other important reactions.[9, 10] The advantages of having metal particles supported include the following several aspects: (1) The catalyst is easily and safely handled compared to the particles in the gas phase. (2) The catalysts may be used in a variety of reactors, and if used in a liquid medium they may be recovered by filtration. (3) Because metal particles are well separated from each other, they do not grow in size by sintering when heated to hight temperature in a reducing atmosphere.[11] (4) The support provides a means of bringing promoters into close contact with the particles. There are also other advantages specific to particular catalyst systems, which we will not go to details. Here, it is instructive to show the correlation between exposed (specific) surface area and the size of the metal particles. Suppose the catalytic active phase (density $\rho$ in kg/m$^3$) consists of uniform spherical metal particles. The specific area can be estimated as:

Volume of one particle, $V = 1/6\pi d^3$ (m$^3$)

Weight of one particle, $W = 1/6\rho\pi d^3$ (kg)

Surface area of one particle, $S_P = \pi d^2$ (m$^2$)

Specific surface area, $S_A = S_P/W = \pi d^2/(\rho * 1/6\rho\pi d^3)$ (m$^2$/kg)

It is obvious that smaller particles will have larger specific surface area, or higher *dispersion*, which may result in an enhancement of catalytic activity.

Although the consequences of the smaller size of metal particles in catalysis seem quite straightforward, in most cases this scenario is more complex than we expected. In fact, at sufficiently small sizes, which most often lie in the nanoscale regime, the dependence of the material's property on size becomes non-scalable, and then small becomes different

in an essential way, where the physical and chemical properties become emergent in nature, that is, they can no longer be deduced or extrapolated from those known for larger sizes when size of the materials is comparable or less than the de Broglie wavelength of electrons. Gold is an excellent example, which is also one of the most commonly studied metal nanocatalysts in the last decade. Gold occupies a position at one extreme of the range of metallic properties, and its legendary chemical inertness is attributable to the Lanthanide Contraction and the relativistic effect, which becomes significant when atomic number Z exceeds about 50. When the 1s orbital of Au shrinks, the s orbitals of higher quantum number have to contract in sympathy in order to maintain orthogonality. In reality, the 6s orbital shrinks relatively more than the 1s, which also operates on the p electrons but to a less extent. d and f electrons are hardly affected because they never come close to the nucleus. This energetic stabilization of the 6s and 5d shells because the 4f electrons do not adequately shield them from the increasing nuclear charge would lead to the disposition of their orbitals: 5d and 6s electrons are drawn towards the nucleus. Therefore, gold is much more inert compared to its neighboring metals such as Cu, Ag and Pt.

While bulk gold is a chemical inert material, interestingly, nanoscaled gold particles exhibits surprisingly reactivity. Haruta and coworkers' pioneering work[12] showed the exceptional catalytic activity of Au nanoparticles of 2-5 nm in diameter deposited on oxides towards CO oxidation at temperature as low as -76 °C, close to the coldest ambient temperature on this planet (-89.2 °C at Vostok in Antartica).[12] Since then, there has been an explosion of interest in Au nanocatalyisis and it leads to the so-called "Gold-Rush Era" in heterogeneous catalysis.[13–20] However, up to now, there has been no common consensus about the origin of such high catalytic activity of nanogold, and it

is generally accepted that the catalytic activity of Au depends to a large extent on the size of the Au particles, and other effects, such as the nature of the substrate, and particle/support interface, charge transfer between metal particles and support, were also proposed to be of fundamental importance.[21–23] Aside from oxides, many other materials such as metal carbides, carbon, metal-organic frameworks (MOFs) and even biomaterials were also studied for supporting metal nanoparticles. In the following, we will review some of the important materials as supports.

### 1.2.1 Metal oxides and carbides

In general, metal oxides offer high thermal and chemical stabilities combined with a well-developed structure and high surface areas ($>$100 $m^2g^{-1}$), meeting the requirement of most applications. Model catalysts, which consist of metal oxide surfaces onto which metal particles are deposited, have been used in experiments for most of the time. For instance, the Haruta and coworkers' discovery of gold nanoparticles that are very active for CO oxidation were supported on oxides of 3d transition metals of group VIII, namely, Fe, Co, and Ni.[12] Goodman et al. suggested on the basis of studies involving a bilayer gold model catalyst supported on $TiO_X$ that the thickness, shape, and oxidation state of gold nanoparticles are responsible for the high catalytic activity.[24] For the oxide support, it is now generally accepted that reducible (active) oxides such as $TiO_2$, $CeO_2$, or $Fe_2O_3$, which have a lower ionic character and a small bandgap, are superior to nonreducible (inert) oxides such as MgO, $Al_2O_3$, or $SiO_2$ that have a marked ionic character and a wide bandgap, under similar conditions.[25–27] This may be accounted for by the fact that the interaction between active oxides and supported metal clusters

is relatively stronger, and the support-mediated oxygen transport, that is, oxygen is released from the oxidic support which diffuses over the support surface to the edges of the metal particles, where the CO oxidation reaction happens.

In the way to search for new catalysts, one may wonder whether metal particles deposited on supports other than metal oxides may provide alternative catalysts with different properties. Recently, Illas et al.[28] found that small gold nanoclusters in contact with TiC(001) could cleave both S-O bonds of $SO_2$ at temperature as low as 150 K, making Au/TiC an excellent catalyst for hydrogenation processes. As for compounds, the transition-metal carbides are less ionic than the metal oxides, and some transition metal carbides can display a chemical behavior which is reminiscent of Pt, Pd, Ru or Rh and in addition can exhibit important advantages over these bulk metals in terms of catalytic selectivity and resistance to poisoning during the transformation of carbon-containing molecules.[29] Systematic studies showed that the surfaces of metal carbides such as ZrC(001), VC(001), TaC(001) and $\delta$-MoC(001) may be able to activate nanogold.[30, 31] Joint experimental and theoretical studies have shown that the Au/carbide interface exhibits little ionic character,, and there is a substantial polarization of electrons around Au that significantly affects its chemical properties.[32]

### 1.2.2 Carbonaceous nanomaterials

Carbon-related materials, such as activated carbon,[33], carbon black,[34] graphite and graphitized materials,[35, 36] offer great advantages as catalyst supports due to their abundance and well-defined porosities. Deactivated catalyst metals can also be easily recovered by simply burning the carbon. Recently, the carbon-based nanomaterials have

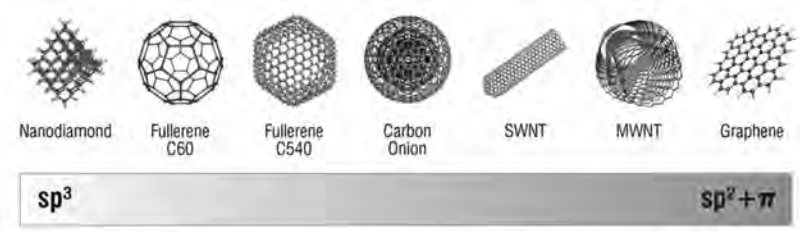


Figure 1.2: Various kinds of carbonaceous nanostructures corresponding to different hybridization states. Reprinted with permission from Ref.[37].

attracted considerable interest by their unique and tunable properties for identifying and addressing electronics and environmental challenges. The physical, chemical, and electronic properties of carbonaceous nanomaterials are strongly coupled to carbon's structural conformation, thus, its hybridization states. The ground-state orbital configuration of carbon's six electrons is $1s^2 2s^2 2p^2$. The energy gap between 2s and 2p electron shells is quite narrow, so one s orbital electron can easily promote to higher energy p orbital which is empty in ground state. This promotion allows carbon hybridize into a sp, $sp^2$, or $sp^3$ configuration depending on the neighboring atoms. These mutable hybridizations account for diverse organic compounds as well as different bulk configurations of carbon (see Fig. 1.2): Trigonometric $sp^3$ configuration of diamond is thermodynamically favorable at high temperature or pressures, while planar $sp^2$ conformation is preferred at lower heats of formation. In $sp^2$ configuration, monolayer sheet is bound by three $\sigma$ covalent bonds and a single $\pi$ bond, such as in fullerenes,[38] carbon nanotubes (CNTs)[39] and recently discovered graphene.[40]

Among all kinds of carbon materials, graphene seems to be particularly attractive due to its unique 2-dimensional honeycomb (2D) structure that leads to unusual electronic and mechanical properties and may provide an ideal support for metal nanocatalysts.[41, 42]

Indeed, experiments have shown that graphene-supported transition-metal nanoclusters may show greatly enhanced reactivity. As an example, Yoo et al.[43] showed by a well-designed experiment the unusually high catalytic activity of small Pt nanoclusters supported on graphene, which is a valuable contribution to the graphene-based metal nanocatalysis. A major obstacle in using graphene as support for metal nanocatalysis is that graphene itself is chemically inert due to the strong $sp^2$ and $\pi$ binding between carbon atoms in the graphene plane, which leads to two major limitations in real applications. First, because of the weak interaction between graphene and supported metal clusters, the effects of underlying graphene on reactivity of supported metal clusters are not expected to be strong so that it is not easy to control the catalytic performance via tuning the interaction between the reactive centers and the underlying support. Second, as a series of scanning tunneling miscroscopy (STM)[44, 45] and transmission electron microscopy[46] studies have reported, due to the weak adsorption of metal clusters on graphene, those supported clusters are highly mobile. In many cases, they tend to diffuse along the surface and form bigger clusters, leading to eventual catalyst sintering, which definitely is not wanted for real applications.[47, 48] Therefore, despite its desirable properties such as excellent electrical conductivity and structural stability, pristine graphene is unlikely to be a suitable support unless appropriate strategies can be devised to stabilize and immobilize supported metal clusters/particles.

### 1.2.3 Metal-organic framework and other materials

Metal-organic framework (MOFs) have emerged as a particular class of multifunctional materials because of their high specific surface area, porosity and chemical tunability, which has lead to many applications concerning gas storage, separations, chemical sensing, drug-release, among many others.[49–51] Recent reports on catalytic studies on MOFs, especially on MOF supported noble metal nanoparticles, have attracted increasing attention.[52–54] Indeed, the spatial construction of metal ions and organic linkers in MOFs leads to the rationally designed networks with nanosized channels and pores that may accommodate metal particles as catalytic centers. Fischer et al.[55] loaded $[Zn_4O(bdc)_3]$ (bdc = 1,4-benzene-dicarboxylate; MOF-5 or IRMOF-1) with Pd nanopartcles to yield Pd@MOF-5 materials, which showed superior activity in olefin hydrogenolysis. Similarly, Cu@MOF-5 showed surprising activity on methanol synthesis from CO and $H_2$.[56] More recently, MOF-supported gold nanoparticles were synthesized by using a simple colloid method and it was found that this material can act as a highly active heterogeneous catalysis for CO oxidation.[57] However, difficulties arise during fabrication of MOFs with tunable length of linkers, and now it has generally proven difficult to demonstrate that clusters/nanoparticles are actually encapsulated within the MOF cavities, as sometimes the metal particle sizes clearly exceeds the dimensions of single MOF cavities.[53]

Apart from MOFs, other materials such as zeolites, polymers, biomaterials and biomass have also been reported as supports for metal nanoparticles. Due to their rather large and complicated structures, we will not discuss them in detail. Readers may see a recent review article in this direction.[58].

## 1.3 Controlling the performance of nanocatalysts

One of the principal goals of modern research in heterogeneous nanocatalysis to understand the nature of active sites, and to develop new and practical methods to control the performance of catalysts. The so-called strong metal-support interaction (SMSI) is often seen as critical to sustain high stability and catalytic activity under demanding operation conditions (i.e., high temperature, high vapor pressure, etc.), due to the fact that SMSI has been directly linked to properties of the supported metal particles.[59] It has been well documented that by manipulating the properties of oxide substrate, the stability and catalytic performance of supported metal clusters can be largely modified and controlled.[60–62] In literature, it has been shown that the catalytic activity of supported metal clusters can be effectively controlled by tuning the interaction between clusters and the underlying substrate via modifying the size, dimensionality, charging state of these cluster and/or the thickness, morphology, or chemical composition of the substrate. So far, scientists from physics, chemistry and material sciences have been actively devoted in this field and many exciting results have been reported.

The most widely studied case is the presence of defects, such as vacancies, impurities, interstitials, kinks, steps and grain boundaries in oxide substrate, of which some defects can be prepared with ease on the surface of reducible oxides such as $CeO_2$ and $TiO_2$. Anchoring the active metal components to these defects may lead to strong interaction between metal clusters and oxides, which fundamentally determines the dispersion, morphology, and, therefore the catalytic activity. For example, Chen and Goodman[63] have described the formation of stable, two-dimensional (2D) Au clusters on a $TiO_2$ substrate with rich oxygen vacancies, which have high catalytic activity compared to

these clusters deposited on substrate with poor oxygen vacancies. The result was also demonstrated by theoretical calculations.[64] On nonreducible surfaces, Landman and coworkers[21] showed that the charging of a $Au_8$ cluster from F-center defects of MgO support plays a key role in the activating of clusters, as $O_2$ molecule does not bind to $Au_8$ in the gas phase or deposited on pristine MgO (001) surface, it can be greatly activated on defect-rich MgO surface supported Au clusters. Other defects can be introduced by post treatment of the oxide surface, such as creation of trapped electrons, $(H^+)(e^-)$ centers by exposure to atomic H or $H_2$ under UV light, addition of promotion elements (alkali metals) and hydroxylation of oxide surfaces.[65–68] The effects of these defects have also been extensively reported in literature and results have been diverse. Nevertheless, a crucial problem exists in introducing defects to supports, that is, it is rather difficult to produce such defects in a controllable manner due to their complexity, and further understanding the electronic structures of these defects as well as their effects on the performance of catalysts are also needed.

The second commonly used approach is to tune the thickness of the oxide substrate. Oxide ultrathin films are essential components of several modern technologies, such as $SiO_2$ films in field effect transistors, ferroelectric ultrathin film capacitors, and solar energy materials.[69–71] Recently, it was theoretically predicted that the adsorption morphology, binding energies and charging state properties of metal clusters may continuously change as a function of the thickness of oxide film, which itself supported on metal surface.[72] Zhang et al.[73] further showed that on a very thin defect-free MgO film grown on metal surface, supported Au clusters exhibits very high activity for the oxidation of CO. The enhanced wetting propensity and catalytic activity of these Au nanoclusters can be visualized in a quantum tunneling picture (see Fig. 1.3), in which

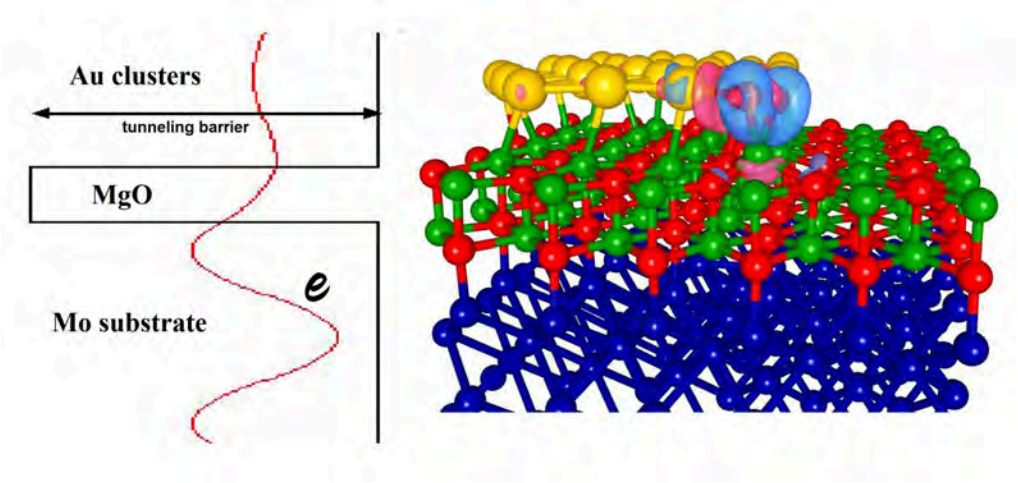


Figure 1.3: Electron quantum tunneling picture of a two dimensional $Au_{20}$ island adsorbs on 2-layer MgO film supported on Mo (100) surface, with a coadsorbed $O_2$ molecule. Superimposed is the isosurface of the excess electronic charge illustrating the activation of the adsorbed molecule through population of the antibonding $2\pi^*$ orbital. Reprinted with permission from Ref.[73]. The possibility of electrons that can tunnel through MgO barrier will be increased when the thickness of MgO film is reduced, leading to an enhancement of catalytic activity for the supported Au clusters.

the electrons tunnel from Mo (100) surface to the clusters when the MgO film thickness is decreased to 2 layers (thus the tunneling barrier is reduced), and then populated to the $2\pi^*$ orbital of $O_2$ molecule. These predictions were later nicely confirmed by STM experiments, which showed an increased wetting propensity of metal clusters supported ultrathin oxide film compared to bulk oxides, and intriguing quantum well states were also observed in these 2D gold clusters on MgO thin films.[74, 75] These results indicate that electron quantum tunneling through ultrathin oxide films may provide vast and unforeseen opportunities in supported heterogeneous catalysis.

Some other methods to control the performance of metal nanocatalysts include externally applying electric or electromagnetic fields,[76] changing the chemical composition of substrate or using mixed oxides (such as alloyed oxides) as supports.[77, 78] In additional, effects of moisture, organic ligand that protects metal clusters during chemical synthesis were also reported.[79, 80] These results show that the environmental parameters during catalyst fabrication could also be taken into consideration when we want to control the catalytic properties of nanocatalysts.

## 1.4 Objectives and scope of this thesis

With significant progress has been achieved in the past decades toward the fundamental understanding of the factors that influence the properties and performance of nanocatalysts, much remains to be learned. Research in nanocatalysts by using supported metal is challenging for several reasons. First, as supported metal clusters or nanoparticles are hybrid systems that are often not well-defined, it is complicated to obtain a clear view of the structure of supported metal clusters or nanoparticles under operating conditions. Second, with the current experimental techniques, it is rather difficult to identify the active sites and reaction mechanism of these catalysts toward specific reactions. So there is a large "material gap" between experiments and theory regarding the issue of what really happens in a catalyzed chemical reaction. Last but not least, to find new and practical ways to control catalysts' activity and selectivity, and to design new catalysts remains a long-standing challenge.

The present work is motivated by the following facts:

1. Although advanced experimental techniques such as STM, TEM could be used to investigate the structures of metal nanoclusters, the ground-state properties, and interaction between the clusters and substrate cannot be fully understood without a theoretical approach.

2. It has been shown that the catalytic activity of metal nanoclusters may be controlled by tuning the thickness of the oxide substrate[72] or applying an electric field.[76] However, the requirement of an ultrathin film or a rather strong field makes these approaches impractical in industrial applications.

3. Despite the previous experimental reports in using graphene as support for metal nanoclusters with enhanced catalytic activity towards CO oxidation, the catalytic mechanism remains unknown.[43] Moreover, there are few studies on how to control the physical and chemical properties of metal clusters on graphene substrate.

The main aim of this thesis is to understand and predict the supported metal nanocatalysis by first-principles calculations. State-of-art computer-aided experiments were applied to probe the geometric and electronic structures of supported metal nanoclusters as catalysts and to elucidate mechanisms of catalytic reactions. The specific objectives of this research were to:

1. Investigate structural, physical and chemical properties of metal nanoclusters and their supports (oxides, carbonaceous nanomaterials, etc.), as well as their hybrid structures as catalytic systems.

2. Study the interaction between metal nanoclusters and substrate, with special attention paid to how the structural, morphological, electronic properties of supported

metal clusters could be influenced by modifying the underlying substrate.

3. Design new catalysts, and find novel and practical methodologies to control their catalytic performance towards important chemical reactions (for example, CO oxidation), with the evaluation of reaction barriers and catalytic mechanisms.

Although experimental methods tend to become more expensive with time, computational methods become much cheaper as computers become faster. By using this theoretical modeling and computational approach, the present study presents a detailed analysis of the physical and chemical properties of supported metal nanocluster hybrid systems, which may contribute a better understanding of heterogeneous nanocatalysis from a theoretical point of view, and may provide new ways to design and control novel, low-cost supported metal catalysts with high efficiency. In this thesis, metal nanoclusters supported on oxides and carbonaceous nanomaterials such as graphene are chosen as model systems, and the prototype example of CO oxidation, one of the best-known heterogeneous reactions,[81] is used to explore the catalytic performance of these supported metal nanocatalysts. Other chemical reactions such as splitting of $H_2O$, oxidation of alcohols or olefines are also important, but they have rather complex reaction steps and hence are beyond the scope of this thesis.

This thesis is organized as following:

In Chap.2, we briefly introduce the theoretical frame work used in this study, which is the first-principles calculations based on density functional theory (DFT). The methodologies to determine the reaction barriers during catalyzed reactions will also to briefly

discussed. In Chap.3, we explore the effects of metal-insulator trancition in oxide materials, which is an important concept in condensed matter physics, on the binding, morphology, charging and catalytic properties of supported Au nanoclusters. In Chap.4, we propose for the first time, the mechanic strain engineered catalytic performance of metal nanoclusters on graphene, which may also be applicable to other stretchable substrate. In Chap.5, we investigate the effects of defect, the single carbon vacancy in particular, in graphene on the stabilization and catalytic activity of metal clusters on graphene support. In Chap.6, the physical and chemical properties of metal-embedded graphene are studied in the context of heterogeneous catalysis, and we propose metal-embedded graphene as a possible novel nanomaterial for single-atom nanocatalyst. Finally, in Chap.7, we present the summary of this thesis and suggest directions for future work.

# Chapter 2

# First-principles methods

Most of low-energy physics, chemistry, biology and material sciences can be explained by modern quantum theory. It has been demonstrated that the ability of quantum mechanics to predict the total energy of a system of electrons and nuclei enable one to reap a tremendous benefit. The First-principles, or *ab initio* approach based on density functional theory (DFT), can provide important quantities such as atomic structures and bonding energies, and may further provide key information on the electronic structures of catalysts and chemical reactions during a catalytic process.

## 2.1 Born-Oppenheimer approximation

Prediction of the structural and electronic properties of a material requires calculations of the solution of the time-dependent Schrödinger equation of the many-body system.

However, the complexity of the many-body problem, resulting from the interaction between an extremely large number of electrons and nucleus ($\sim 10^{23}$), makes it impossible to solve the Schrödinger equations exactly. Therefore, some important approximations have to be made. The first approximation is the Born-Oppenheimer approximation.[82] Because the nuclei are much heavier and move much slower than the electrons, we can "freeze" them at fixed positions and assume the electrons to be in instantaneous equilibrium with them. This "adiabatic principle" reduces the many body problem to the solution of the dynamics of the electrons in some frozen-in configuration of the nuclei. To perform the total energy calculation accurately and efficiently, further approximations are introduced, including density functional method to model the electron-electron interaction, psuedopotential to treat electron-ion interation, supercell to model periodic systems, and iterative scheme to minimize the total energy function. These will be described in following sections.

In the Born-Oppenheimer non-relativistic approximation, only the electrons are kept as players in our many body problem. In this context, the Schrödinger equation of an isolated N-electron atomic or molecular system is given by

$$\hat{H}\Psi = E\Psi \tag{2.1}$$

where $E$ is the electronic energy, $\Psi = \Psi(\mathbf{r}_1, \mathbf{r}_2, ..., \mathbf{r}_N)$ is the wave function, and $\hat{H}$ is the Hamiltonian operator,

$$\hat{H} = \sum_{i=1}^{N}(-\frac{\hbar^2}{2m}\nabla_i^2) + \sum_{i=1}^{N} U(\mathbf{r}_i) + V(\mathbf{r}_1, \mathbf{r}_2, ..., \mathbf{r}_N) \tag{2.2}$$

in which

$$U(\mathbf{r}_i) = -\sum_a \frac{Z_a e^2}{r_{ia}} \tag{2.3}$$

is the external potential acting on electron i due to nuclei charges $Z_a$. And,

$$V(\mathbf{r}_1, \mathbf{r}_2, ..., \mathbf{r}_N) = \sum_{i<j}^{N} \frac{e^2}{|\mathbf{r}_i - \mathbf{r}_j|} \tag{2.4}$$

is the electron-electron repulsion energy.

The Born-Oppenheimer approximation makes it possible to break the wavefunction of a complicated system into its electronic and nuclear (vibrational, rotational) components. These two components can be calculated in two less complicated consecutive steps. However, due to the electron-electron interaction, the equation remains difficult to solve.

## 2.2 Density functional theory (DFT)

Density functional theory (DFT), developed by Hohenberg-Kohn (1964), Kohn and Sham (1965),[85, 86] provided a simple method for describing the effects of exchange and correlation in an electron gas. This is a remarkable theory that allows one to replace the complicated N-electron wave function $\Psi = \Psi(\mathbf{r}_1, \mathbf{r}_2, ..., \mathbf{r}_N)$ and the associated Schrödinger equation by the much simpler electronic density $n(\mathbf{r})$ and its associated calculational scheme. Since its formulation, DFT has used extensively in condensed matter physcis/chemistry and material sciences. It has become a runaway success, enabling advances in practical First-Principles calculations.The density functional theory is based on the following two theorems of Hohenberg-Kohn:

First theorem: *There is a one-to-one correspondence between ground-state density* $n(\boldsymbol{r})$ *of a many-electron system (atom, molecule, solid) and the external potential V(**r**).* This

theorem demonstrates that the ground state electron density can be served as the fundamental quantity instead of the wave function. Since $n(\mathbf{r})$ determines the external potential and the number of electrons, it also determines the Hamiltonian and all other ground-state electronic properties.

$$\begin{aligned} E = E(n(\mathbf{r})) &= T[n(\mathbf{r})] + E_{ne}[n(\mathbf{r})] + E_{ee}[n(\mathbf{r})] \\ &= \int n(\mathbf{r}) V_{ne}(\mathbf{r}) dr + F_{HK}[n(\mathbf{r})] + E_{corr}[n(\mathbf{r})] \end{aligned} \tag{2.5}$$

where

$$F_{HK}[n(\mathbf{r})] = T[n(\mathbf{r})] + E_{exc}[n(\mathbf{r})] + E_{coul}[n(\mathbf{r})] \tag{2.6}$$

where $T[n(\mathbf{r})]$ is the kinetic energy and $E_{ee}[n(\mathbf{r})]$ is the electron-electron interaction energy which contains the Coulomb interactions $E_{coul}[n(\mathbf{r})]$ given by:

$$E_{coul}[n(\mathbf{r})] = \frac{e^2}{2} \int \int \frac{n(\mathbf{r}_1) n(\mathbf{r}_2)}{\mathbf{r}_{12}} d\mathbf{r}_1 d\mathbf{r}_2 \tag{2.7}$$

Second theorem: *There is a universal functional of* $n(\boldsymbol{r})$*, E(* $n(\boldsymbol{r})$*), which is minimized by the ground state density* $n(\boldsymbol{r})$. Therefore, the ground-state energy can be found by varying the electron density $n(\mathbf{r})$ to minimize the energy $E(n_0(\mathbf{r}))$, supposed we know the form of the functional $E(n(\mathbf{r}))$, or at least have a good approximation for it.

However, accurate calculational implementations of the density functional theory are far from easy to achieve due to the fact that the functional $F_{HK}[n(\mathbf{r})]$ is hard to come by in explicit form. While the Hohenberg-Kohn theorem rigorously established that we may use the density alone, as a variable to find the ground-state energy of an N-electron problem, it does not provide any useful computational scheme. Kohn and Sham showed that it is possible to replace the many-body problem with an exact equivalent set

of self-consistent one-electron equations [86, 87]. The Kohn-Sham (KS) total-energy functional for a set of doubly occupied electronic states $\Psi_i$ can be written as

$$E[\Psi_i] = 2\sum_i \int (\Psi_i[-\frac{\hbar^2}{2m}]\nabla^2\Psi_i)d^3\mathbf{r} + \int V_{ion}(\mathbf{r})n(\mathbf{r})d^3\mathbf{r} + \frac{e^2}{2}\int \frac{n(\mathbf{r})n(\mathbf{r}')}{\mathbf{r}_{12}}d^3\mathbf{r}d^3\mathbf{r}' + E_{xc}[n(\mathbf{r})] + E_{ion}(R_I) \tag{2.8}$$

where $V_{ion}$ is the static total electron-ion potential, $E_{xc}[n(\mathbf{r})]$ is the exchange-correlation functional, and $E_{ion}$ is the Coulomb energy associated with interactions among the nuclei (or ions) at positions $R_I$.

It is necessary to determine the set of wave functions $\Psi_i$ that minimizes the Kohn-Sham total-energy functional. These are given by the self-consistent solutions to the Kohn-Sham equations:

$$[(-\frac{\hbar^2}{2m}\nabla_i^2) + V_{ion}(\mathbf{r}) + V_H(\mathbf{r}) + V_{xc}(\mathbf{r})]\Psi_i(\mathbf{r}) = \varepsilon_i(\mathbf{r})\Psi_i(\mathbf{r}) \tag{2.9}$$

where $\Psi_i(\mathbf{r})$ denotes the wave function of electronic state *i*, $\varepsilon_i$ is the KS eigenvalue, and $V_H(\mathbf{r})$ is the Hartree potential of the electrons given by

$$V_H(\mathbf{r}) = \int \frac{e^2 n(\mathbf{r}')}{|\mathbf{r}-\mathbf{r}'|}d^3\mathbf{r}' \tag{2.10}$$

The exchange-correlation potential $V_{xc}(\mathbf{r})$ is given by the functional derivative

$$V_{xc}(\mathbf{r}) = \frac{\delta E_{xc}(\mathbf{r})}{\delta n(\mathbf{r})} \tag{2.11}$$

In the KS equations, the effective potential is the KS potential:

$$V_{KS}(\mathbf{r}) = V_H(\mathbf{r}) + V_{xc}(\mathbf{r}) = \int \frac{e^2 n(\mathbf{r}')}{|\mathbf{r}-\mathbf{r}'|}d^3\mathbf{r}' + \frac{\delta E_{xc}(\mathbf{r})}{\delta n(\mathbf{r})} \tag{2.12}$$

The KS equations represent a mapping of the interacting many-electron system onto a system of noninteracting electrons moving in the KS effective potential due to all the

other electrons. The KS equations must be solved self-consistently so that the occupied electronic states generate a charge density that produces the electronic potential that is used to construct the KS equations. However, the above equations are still in a intractable form because exact expression for the exchange-correlation energy functional remain unknown.

## 2.3 LDA and GGA

To solve the problem of unknown exchange-correlation energy functional, Kohn and Sham proposed the local density approximation (LDA).[86] In LDA, the exchange-correlaton energy of an electronic system is constructed by assuming that the exchange-correlation energy per electron at position $\mathbf{r}$ in the electron gas, $\varepsilon_{xc}(\mathbf{r})$, is equal to the exchange-correlation energy per electron in a homogeneous electron gas that has the same density as the electron gas at point $\mathbf{r}$. Thus

$$E_{xc}(\mathbf{r}) \approx E_{xc}^{LDA} = \int n(\mathbf{r})\varepsilon_{xc}(\mathbf{r})d\mathbf{r} \tag{2.13}$$

and

$$\varepsilon_{xc}(\mathbf{r}) = \varepsilon_{xc}^{\mathrm{hom}}(n(\mathbf{r})) \tag{2.14}$$

$\varepsilon_{xc}^{\mathrm{hom}}(n(\mathbf{r}))$ can be further split into exchange and correlation contributions,

$$\varepsilon_{xc}^{\mathrm{hom}}(n(\mathbf{r})) = \varepsilon_{x}^{\mathrm{hom}}(n(\mathbf{r})) + \varepsilon_{c}^{\mathrm{hom}}(n(\mathbf{r})) \tag{2.15}$$

A Hartree-Fock description of electron gas leads to a simple form of the exchange energy functional $\varepsilon_{x}^{\mathrm{hom}}(n(\mathbf{r})) \propto n(\mathbf{r})^{4/3}$. A much more accurate exchange-correlation energy for the homogeneous electron gas as a function of density may be derived from quantum

Monte Carlo simulations and used to construct exchange-correlation functionals within the framework of the LDA. The LDA, in principle, ignores corrections to the exchange-correlation energy at a point **r** due to the nearby inhomogeneities of the electron density. Nevertheless, LDA has proven to be a good approach for the calculation of structures, vibrational frequencies, elastic moduli and phase stability. On the other hand, several problems are also encountered with the LDA. For example, LDA underestimates the band gap of semiconductor and insulator. LDA also tends to overbind (typically by 20-30%), so the calculated lattice constant is underestimated and the cohesive energy is overestimated.

A natural extension of the LDA is the generalized gradient approximation (GGA) [88, 89], in which there is an explicit dependence of the exchange-correlation functional on the gradient of the electron density. The exchange-correlation functional can be written as:

$$\varepsilon_{xc}[n(\mathbf{r})] = \int f(n, \nabla n) d^3\mathbf{r}, \tag{2.16}$$

The GGAs proposed by Perdew et al. have been widely used and have proved to be quite successful in correcting some of the deficiencies of the LDA [88, 89]. For instance, the GGA improves binding and dissociation energies, especially for systems containing hydrogen. Many properties of 3*d* metals are greatly improved. However, the GGA is far from ideal, and finding an accurate and universally-applicable $E_{\mathrm{xc}}$ remains a great challenge in DFT. Nowadays, practical $E_{\mathrm{xc}}$ functionals are the major approximation made to DFT: they are not derived from first principles, but are postulated from physically reasonable assumptions, and their use is justified a posteriori by their success [90].

## 2.4 Implementation of DFT

### 2.4.1 Bloch's theorem

With the density functional theory, the many electron Schrödinger equation can be mapped onto the N one-electron Kohn-Sham equations. However, it remains a formidable task to handle an infinite number of non-interacting electrons in the static potential of an infinite number of nuclei or ions. Two problems must be solved: a wave function must be calculated for each of the infinite number of electrons in the system, and the basis set required to expand each wave function is infinite since each electronic wave function extends over the entire solid. Fortunately, we can reduce the problems to a finite periodic systems based on the Bloch's theorem.

For a system of electron moving in a periodic potential, Bloch's theorem states that the corresponding wavefunction of the electron has the form:

$$\Psi_k(\mathbf{r}+\mathbf{R}) = e^{i\mathbf{k}\cdot\mathbf{r}}u_k(\mathbf{r}), \tag{2.17}$$

where $u_k(\mathbf{r})$ has the same periodicity as the potential. For a crystal lattice potential satisfies the translation invariance:

$$u_k(\mathbf{r}+\mathbf{R}) = u_k(\mathbf{r}), \tag{2.18}$$

where **R** is the real space lattice vector. Based on this theorem, the wavefunction of a single atom in a lattice can be written as the product of the plane wave and the periodic function $u_k(\mathbf{r})$. Moreover, the wavevector **k** can always be folded into the first Brillouin zone ($1^{st}$ BZ) in the context of electronic property calculations since the electron energy

is periodic in the **k**-space and each **k**-point outside the $1^{st}$BZ cam ne mapped onto a **k**-point inside.

Many real systems do not have periodic symmetry along all three dimensions. For instance, a surface system only has periodic symmetry parallel to the surface directions; a nanocluster/particle or molecule is completely aperiodic. To study these systems, two schemes are feasible. One is to model the system with a cluster of atoms, so-called Cluster model, and another is to model a periodic symmetry on the aperiodic dimension, so-called Supercell method. Periodic supercell is widely used for the surface/interface system modeling. which is implemented by modeling the surface/interface with periodically arranged slabs which are separated by vacuum layers. To minimize the artificial Coulomb interactions between two neighboring surfaces/interfaces, the vacuum layer should be thick (typically $>$10 Å). The thickness of the slabs is dependent on the specific case, and usually the slab with smaller interlayer spacing should be thicker.

### 2.4.2 Plane-wave basis sets

Bloch's theorem states that the electronic wave functions at each **k**-point can be expanded in terms of a discrete plane-wave basis set:

$$\psi_{n,\mathbf{k}}(\mathbf{r}) = \sum_{\mathbf{G}} c_{n,\mathbf{k}+\mathbf{G}} \exp[i(\mathbf{k}+\mathbf{G})\cdot\mathbf{r}]., \tag{2.19}$$

where **G** are reciprocal lattice vectors. After expansion of the wavefunctions, the Kohn-Shan equation can be reduced to a secular equation:

$$\sum_{\mathbf{G}'}[\frac{\hbar^2}{2m}|\mathbf{k}+\mathbf{G}|^2\delta_{\mathbf{G}\mathbf{G}'} + V(\mathbf{G}-\mathbf{G}') + V_H(\mathbf{G}-\mathbf{G}') + V_{xc}(\mathbf{G}-\mathbf{G}')]c_{n,\mathbf{k}+\mathbf{G}'} = \varepsilon_{n,\mathbf{k}} c_{n,\mathbf{k}+\mathbf{G}}. \tag{2.20}$$

In principle, an infinite plane-wave basis set is required to expand the electronic wave-functions. Fortunately, the coefficient $c_{n,\mathbf{k}+\mathbf{G}}$ for the plane-wave with small kinetic energy $\frac{\hbar^2}{2m}|\mathbf{k}+\mathbf{G}|^2$ are typically more important than those with large kinetic energy. Thus, the plane-wave basis set can be truncated to include only plane-waves that have kinetic energies less than some particular cutoff energy $E_{cut} = \frac{\hbar^2}{2m}|\mathbf{k}+\mathbf{G}_{cut}|^2$. The truncation of the plane wave basis set at a finite cutoff kinetic energy will lead to an error in the total energy of the system. However, it is possible to make this error arbitrarily small by increasing the size of the basis set by allowing a larger energy cutoff.

### 2.4.3 Brillouin zone sampling

Electronic states are allowed only at a set of **k**-points determined by the boundary conditions that apply to the bulk solid. The sensity of allowed **k**-points is proportional to the volume of the solid. The infinite number of electrons in the solid are accounted for by an infinite number of **k**-points, and only a finite number of electronic states are occupied at each **k**-point. The Bloch's theorem changes the problem of calculating an infinite number of electronic wave functions to one of calculating a finite number of electronic wave functions at an infinite number of **k** points. The occupied states at each K point contribute to the electronic potential in the bulk solid so that an infinite number of calculations are needed to compute this potential. However, because the change in $\Psi_{n,\mathbf{k}}$ with **k** becomes negligible for **k**-points that are close together, a great simplification is available by calculating at a finite number of k-points, i.e., **k**-point sampling. Various methods have been proposed for the **k**-points sampling, like the one by Monkhorst-Pack, Lehmann and Taut, Blochl-Jepsen-Andersen, Methfessel and coworkers, Muller

and Wilkins, etc. The Monkhorst-Pack[91] is the most widely used scheme, of which the basic idea is to construct equally spaced **k**-points ($N_1 \times N_2 \times N_3$) in $1^{st}$BZ according to

$$\mathbf{k} = \frac{n_1 + 1/2}{N_1}\mathbf{b}_1 + \frac{n_2 + 1/2}{N_2}\mathbf{b}_2 + \frac{n_3 + 1/2}{N_3}\mathbf{b}_3, \tag{2.21}$$

where $n_1$, $n_2$, and $n_3$ = 0,$\cdots$, $N_i$-1 ($i$ = 1$\sim$3). Symmetry is used to map equivalent k-points to each other, which can reduce the total number of k-points significantly generated by Eq. 2.23. The computed total energy will converge as the density of **k** points increases, and the error due to the K-point sampling then approaches zero. In some systems, such as metal, a dense set of **k** points is required to determine the Fermi surface precisely. Sometimes **k**·**p** method is used to reduce the computational cost of performing a very dense **k**-points sampling.

### 2.4.4 Pseudopotential method

Although Bloch's theorem states that the discrete plane waves can be used as the electronic wave functions, a plane-wave basis set is very poorly suited to the expansion of electronic wave functions because a very large number of plane waves are needed to expand the tightly bound core orbitals and to follow the rapid oscillations of the wave functions of the valence electrons in the core region. An extremely large plane-wave basis set would be required to perform an all-electron calculation and a vast amount of computational time would be required, which is even impractical for real large systems. Thanks to the pseudopotential approximation, it allows the expansion of electronic wavefunctions with much smaller number of plane wave basis sets.[92–94]

In most cases, the core electrons are not important in describing, for example, the nature

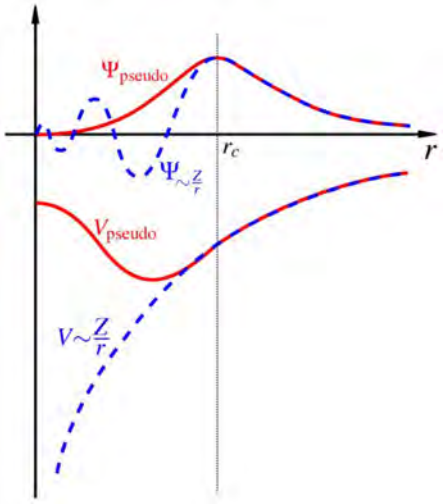


Figure 2.1: Schematic illustration of all electron (dash line) and pseudopotentials (solid line) and their corresponding wavefunctions.

of the bonding between atoms in a crystal; only the valence electrons surrounding the core region contribute to it. The pseudopotential method neglects the core electrons and strong ionic potential in the calculation, and replaces them by a fixed effective potential that acts on a set of pseudo wavefunctions rather than the true valence wavefunctions, as shown in Fig. 2.1.[95] The pseudopotential is introduced in such a way that there are no radial nodes in the pseudo valence states in the core region while the pseudopotential and pseudo wavefunctions are identical to the true electron wavefunction and potential outside a cutoff $\mathbf{r}_c$.

One of the most frequently used pesudopotentials in first-principles calculations is the norm-conserving pseudopotential developed by Bachelet et. al[96]. With norm-conserving pseudopotentials, inside $\mathbf{r}_c$, the pseudo wavefunctions differ from the true wavefunctions as stated above, but the norm is constrained to be the same as the true valence states:

$$\int_0^{r_c} |\psi^{ps}_{n,\mathbf{k}}(\mathbf{r})|^2 d\mathbf{r} = \int_0^{r_c} |\psi_{n,\mathbf{k}}(\mathbf{r})|^2 d\mathbf{r} \tag{2.22}$$

Norm-conserving pseudopotentials are very successful for solids of *s*, *p*-bond main group elements, but they do not show very good results for first-row elements, transition metals and rare-earth elements due to the highly localized valence orbitals in these elements, In 1990, Vanderbilt and co-workers proposed another type of pseudopotential which is named as ultrasoft pseudopotential.[97] In this pesudopotential, the norm-conservation constraint is removed and the pseudo wavefunctions inside $r_c$ are required to be as soft as possible, which greatly reduces the plane wave cutoff needed in calculations. In 1994, Blöchl developed the idea of "soft pseudopotential" in Vanderbilt's scheme, and proposed the "projector augmented wave" (PAW) method,[98] which has smaller radii cutoffs (core radii), and also exactly reconstructs the valance wave function with all nodes in the core region, thus it is widely adopted to calculate systems including *3d* and *4f* electrons.[99]

### 2.4.5 Minimization of the Kohn-Sham energy functional

To perform a total energy pseudopotential calculation, it is necessary to find the electronic states that minimize the KS energy functional. Indirect searching for the self-consistent KS Hamiltonian can lead to instability because of the discontinuous changes in KS Hamiltonian from iteration to iteration. These instabilities would be avoided if the KS energy functional is minimized directly because the KS energy functional normally has a well-defined energy minimum. It is necessary to find a computational method that allows direct minimization of the KS functional in a tractable and efficient way.

The conjugate-gradients (CG) technique provides a simple and effective procedure for the implementation of such a minimization approach. To locate the energy minimum, the initial search direction is taken to be the negative of the gradient at the starting point. A subsequent conjugate direction is then constructed from a linear combination of the new gradient and the previous direction that minimizes the functional. Although the CG technique provides an efficient method for locating the minimum of a general functional, it is important to implement the technique in such a way as to maximize computational speed and to minimize the memory requirement. A CG method that fulfills these criteria has been developed by Teter et al [100].

## 2.5 Transition state determination

In computational chemistry or condensed matter physics, the calculation of transition rates, such as rates for diffusion or chemical reactions, is an important task. This kind of calculation requires the investigation of the minimum energy path (MEP) between the initial and final states. Once the MEP has been mapped out, the saddle point (the maximum along the potential energy surface) and the activation energy barrier can also be identified and evaluated (see Fig. 2.2). In such as way, it is possible to obtain accurate estimates of the transition rates by using a purely statistical approach, namely, transition state theory (TST).[101, 102]

In recent years, two different approaches to locate transition state have been successfully used for studying surface reaction: (i) constrained minimization method.[103, 104] and (ii) nudged elastic band (NEB) method.[105, 106] The idea of the first method is very

simple: some subset of coordinates in the system of interest is used to define a reaction progress variable (for instance, through linear interpolation of two end points). This variable with one degree of freedom is changed stepwise from the initial value to the final value, and at each step a full minimization is performed over the remaining $3N$-1 degree of freedom. To get a relatively accurate activation barrier, a very dense interpolation near the the saddle point is needed. In NEB method, a chain of states (images) of the system is generated between the initial and final states, and all the intermediate images are then optimized simultaneously to search for the MEP. While the NEB method gives a discrete representation of MEP, the energy of saddle points needs to be obtained by interpolation. When the energy barrier is narrow compared with the length of MEP, few images exist around the saddle point and the interpolation can be inaccurate. An improved NEB method, called the climbing image NEB (CI-NEB) method was proposed.[107] In CI-NEB method, the climbing image moves up the potential surface along the elastic band and down the potential surface perpendicular to the band, and the other images in the band serve to define the one degree of freedom for which a maximization of energy is performed. As long as the CI-NEB method converges, the climbing image will converge to the saddle point, which gives a good approximation of the barrier.

## 2.6 VASP software package

Vienna Ab-initio Simulation Package (VASP)[108] is developed for performing first-principles calculations based on DFT using pseudopotentials and a plane wave basis set. The interaction between ions and electrons is described by ultra-soft Vanderbilt pseudopotentials (USPP) or by the projector-augmented wave (PAW) method. The basic

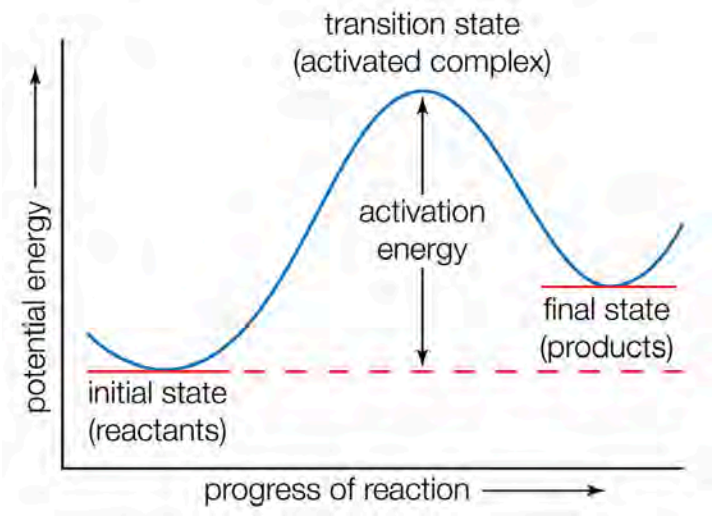


Figure 2.2: Potential-energy curve. The activation energy represents the minimum amount of energy required to transform reactants into products.

methodology is DFT, but VASP code also allows use of post-DFT corrections such as hybrid functionals mixing DFT and Hartree-Fock exchange, many-body perturbation theory (the GW method) and dynamical electronic correlations within the random phase approximation. Forces and the full stress tensor can be calculated and used to relax atoms into their instantaneous ground-state. VASP uses efficient matrix diagonalisation schemes and an efficient Pulay/Broyden charge density mixing. VASP can perform both the static and molecular dynamics simulations, offering information about total energies, forces and stresses on an atomic system. VASP can also be used to optimize geometries, to study the electronic, optical and phonon properties of materials.

Current, both transition state determination methods, i.e., constrained minimization method and NEB method, have been successfully incorporated and implemented in the VASP code, which enable its wide usage in theoretical community, especially in the field of computational design of catalysis.

# Chapter 3

# Effects of metal-insulator transition on supported Au nanocatalysts

## 3.1 Introduction

Transition-metal (TM) oxides are often semiconducting or insulating with a definite bandgap despite the fact that the TM compounds normally have partially filled $d$ bands. Metal-insulator transition (MIT) in TM oxides has been a continuous interest of research in condensed matter physics due to its importance in both fundamental and technological sides.[109] Current strategies in making such a transition in oxide materials, whether in bulk or thin film form, can be realized by several ways: a) Chemical doping to shift the Fermi energy ($E_F$) to conduction band or valence band owing to the infusion of charge carriers, or to directly modulate the bandgap by altering electronic structures;[110, 111] b) Reducing the ratio between on-site Coulomb interaction ($U$) and bandwidth of the

system (*W*) to close the bandgap, which may be triggered by atomic-scale substitutions or by application of external parameters such as pressure, heat, electric or magnetic fields;[112, 113] c) By introducing structural disorder, such as spatial fluctuations in strong electrostatic potential, to produce so-called Anderson transition even in a system of non-interacting electrons.[114]

Strontium titanate ($SrTiO_3$), a typical perovskite-type oxide compound and one of the most widely used ceramic materials, is an excellent example for the study of MIT in oxides. Experiments have shown that it exhibits fascinating variety of electronic properties, ranging from insulating, semiconducting, metallic to superconducting behavior.[115, 116] Electron-doping in $SrTiO_3$, with dopants such as La or Nb which substitute on Sr and Ti sites, respectively, is a facile and widely-used technology to achieve such transitions.[115, 117–122] For instance, experiments have clearly demonstrated that the Nb/La doping concentration in $SrTiO_3$ can be easily tuned, and the mobility of electrons after MIT can be precisely controlled.[119] Recently, electron mobilities exceeding 30,000 $cm^2V^{-1}S^{-1}$ in La-doped $SrTiO_3$ thin films were observed by Son et al.,[122] indicating its great potential applications in electronics.

On the other hand, in the emerging field, nanocatalysis, where TM oxides are widely used as supports or substrates for metal nanoclusters, effects of MIT in TM-oxide substrate on catalytic activity of supported metal clusters have never been discussed. In this chapter, via first principles methods based on density functional theory (DFT), we investigated the chemical reaction of CO oxidation catalyzed by TM-oxide supported metal nanoclusters. Special attention is paid to effects of doping-induced MIT on adsorption geometry, stabilization and catalytic activity of Au clusters.

In this work, $Au_8$ clusters supported on $SrTiO_3$ (001) surface are chosen as model catalysts for CO oxidation. Gold octamers ($Au_8$) are probably the most studied Au nanocatalysts, [21, 79, 123] due to their stability and unique catalytic activity identified in experiments.[21, 130, 131] We investigated effects of the Nb-doping induced MIT in $SrTiO_3$ on the morphology, bonding geometry, and catalytic activity of $Au_8$ clusters supported on (001) surface of $SrTiO_3$. We found that the MIT has strong effects on adsorption of Au clusters, leading to a dimensionality crossover of the lowest-energy state of the supported Au cluster (from the 3-dimensional structure to a planar one), and at the same time, greatly enhances the catalytic activity of supported Au clusters, resulting in the low barrier of catalyzed CO oxidation. These results open a new avenue for tuning the catalytic activity of TM-oxide supported metal clusters.

## 3.2 Computational details

Our calculations were performed using the VASP code based on DFT,[108] with the projector augmented-wave method and general gradient approximation in Perdew-Burke-Ernzerhof format.[124] Plane-waves with a kinetic energy cutoff of 400 eV were used as the basis set. DFT is well known to significantly underestimate the bandgap of TM oxides. We therefore used the GGA+U approach [125] to describe strong electron-electron interactions between localized Ti $d$-electrons. It was found that GGA+U calculations with U=8.5 eV and J=1 eV yield a reasonable bandgap of 3.0 eV for bulk $SrTiO_3$ that agrees well with the experimental value, 3.2 eV.[126] The $SrTiO_3$ (001) surface was modeled using a periodic slab with a mirror symmetry consisting of five alternating SrO and $TiO_2$ layers. We also tested 7 and 9 layers which give similar results. The $4\times4$

surface supercell was chosen for Nb doping and $Au_8$ cluster adsorption, and a vacuum region of at least 20 Å in the direction normal to the surface was adopted. A 5×5×1 Monkhorst-Pack grid for of k-point sampling in the Brillouin zone was employed in calculations. Reaction barriers were calculated by incorporating the constrained energy minimization method[103, 104] into VASP. In this method, reaction barriers were calculated in such a way that all degrees of freedom except the reaction coordinate are allowed to be relaxed. In our calculations, the reaction coordinate is the distance between the C atom of the CO and the nearest oxygen atom of the oxygen molecule. All atomic coordinates were fully relaxed until the force is less than 0.01 eV/Å.

## 3.3 Nb-doping induced metal-insulator transition in $SrTiO_3$

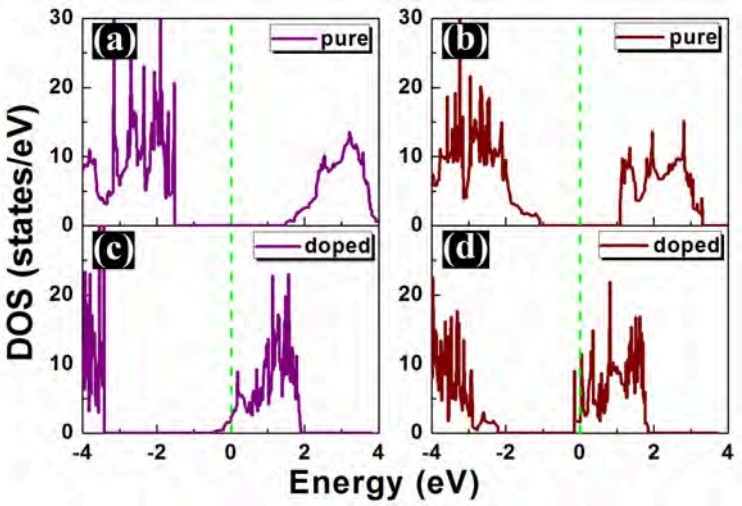


Figure 3.1: (a) Density of states (DOS) for pristine $SrTiO_3$ (001) surfaces (a,b) and Nb-doped surfaces (c,d). Left panels (a,c) are for SrO-termination and right panels (b,d) for $TiO_2$-termination.Fermi energy has been set to zero.

Electronic structures of Nb-doped bulk $SrTiO_3$ have been extensively explored in both experimental and theoretical work.[127, 128] While, in theoretical studies, more reliable GGA+U calculations of (001) surfaces of doped $SrTiO_3$ have not been reported before. We first carried out GGA+U calculations for both the pristine and Nb-doped SrTiO3 (001) surfaces with SrO or $TiO_2$ termination. In Fig. 3.1, we show the density of states (DOS) for different cases. To simulate the doped surface with SrO ($TiO_2$) termination, Ti atoms in the second (third) layer of the surface slab are substituted by Nb atoms with a doping concentration of 0.52% (0.48%). Our calculations show that the pristine surfaces are essentially insulating (Figs. 3.1(a) and 3.1(b)), which agrees with previous theoretical studies[129] but with nearly 0.5 eV larger bandgaps due to the inclusion of the onsite Hubbard repulsion. With the doping of Nb atoms, as shown in Fig. 3.1(c) and 3.1(d), for both types of surface terminations, the Fermi level is shifted into the conduction bands, resulting in the metal-insulator transition. Higher doping concentrations were also studied, and it is found that in general, higher doping concentrations lead to the further shift of Fermi level into the conduction band and "more" metallicity. We also performed standard LDA+GGA (without U) calculations, and results show that the doping-induced MIT is independent of U term, although with significantly underestimated bandgaps for the undoped cases. Work function (WF) is an useful physical quantity in evaluating the reactivity of the surface. We calculated WFs of these surfaces as the difference between the vacuum level and Fermi level, and found that there is a gradual decrease of WFs with increasing Nb doping concentrations. For instance, when the doping concentration increases from 0% to 2.08% (1.92%) for SrO ($TiO_2$)-terminated surface, WF decreases from 3.8 eV (4.7 eV) to around 1.4 eV (3.3 eV), suggesting the enhanced reactivity of these $SrTiO_3$ (001) surfaces due to the MIT.

## 3.4 MIT-controlled dimensionality crossover of supported gold nanoclusters

After examining the Nb-doping induced MIT in $SrTiO_3$, we then studied the adsorption of $Au_8$ clusters on $SrTiO_3$ (001) surfaces. Two isomers of $Au_8$, a three dimensional (3D) one and another planar (P) one, as shown in Figs. 3.2(a) and 3.2(b), were considered. Literatures have shown that in the gas phase, $Au_8$ with planar structure is more table than the 3D one.[123] However, when absorbed on metal oxides, the 3D isomer is normally the most stable structure,[72, 74, 131] which is attributed to the bonding and charge transfer effects. We have considered various adsorption sites and configurations in searching for ground-state structures. The most stable (ground-state) adsorption structures are presented in Figs. 3.2(c-f). Our calculations show that for $Au_8$ clusters adsorbed on pristine surfaces, 3D isomer is always energetically favored over the planar one, in agreement with literatures. On SrO-terminated surface, the 3D $Au_8$ is adsorbed with three Au atoms binding with O atoms in the surface (see Fig. 3.2 (c)), with an adsorption energy around 3.07 eV. For the case of $TiO_2$ termination (Fig. 3.2(d)), the adsorption is weaker with the adsorption energy 1.22 eV. The different adsorption energies on two surfaces are consistent with their different work functions: The WF of SrO-terminated surface is 0.9 eV lower than that of the $TiO_2$-terminated one. In comparison, the adsorption energies of the P isomer is much lower than their 3D counterparts, being 2.56 eV and 0.84 eV for SrO and $TiO_2$ terminations, respectively. When adsorbed on Nb-doped $SrTiO_3$ surfaces, interestingly, the planar isomer becomes more stable. Lowest-energy configurations with the doping concentration 2.08% for SrO termination and 1.96% for $TiO_2$ termination are shown in Figs. 3.2(e) and 3.2(f), respectively. In

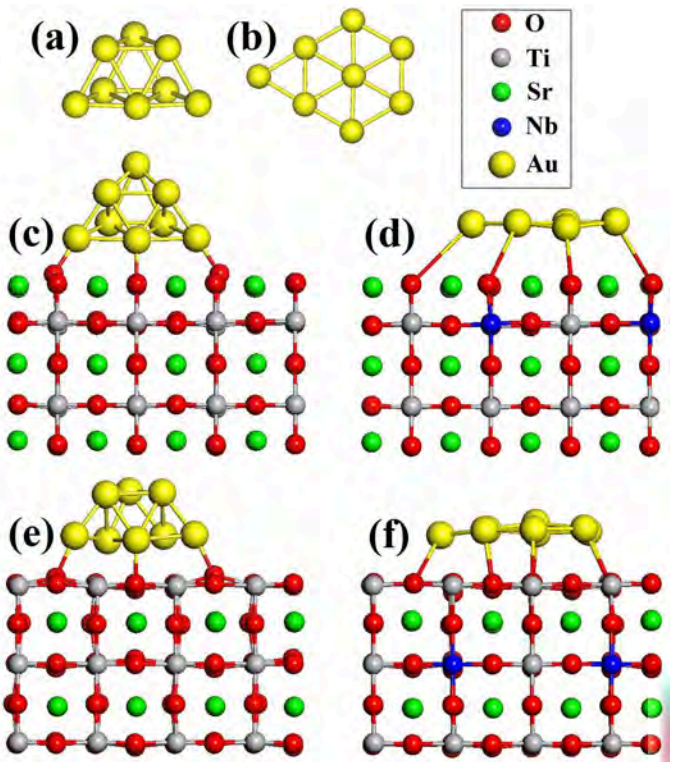


Figure 3.2: Atomic configurations of 3D (a) and P (b) isomers of $Au_8$ clusters in gas phase. Lowest-energy absorption structures on SrO or $TiO_2$ terminated $SrTiO_3$ (001) surfaces with or without Nb doping (c-f). Note that for both termination types, without doping, the 3D isomer is more stable (c,e), and when doped with Nb with the doping concentration 2.08% for SrO termination and 1.96% for $TiO_2$ termination, the P isomer is more stable (d,f).

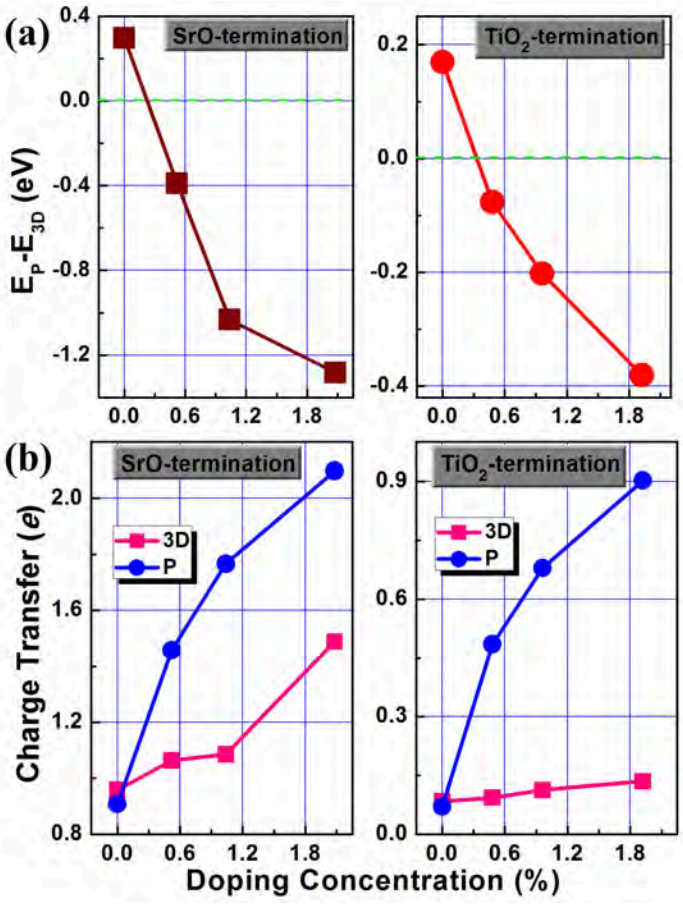


Figure 3.3: (a) Total energy difference between 3D and P isomers of $Au_8$ clusters adsorbed on SrO (left panel) or $TiO_2$ (right panel) terminated $SrTiO_3$ (001) surfaces under different Nb doping concentrations. The energy difference is defined as $E_p$-$E_{3D}$. (b) Charge transfer from the surface to the supported cluster as a function of doping concentration.

these cases, all Au atoms are bonded with O atoms in the surface, and the adsorption energy is higher than their 3D counterparts by 1.1 eV and 0.22 eV for SrO and $TiO_2$ terminations, respectively.

The increase in the doping concentration was found to increase the energy difference between the planar and 3D structures, indicating the doping enhanced stability of the planar isomer relative to that of the 3D one. In Fig. 3.3(a), we showed the variation of the total energy difference between two isomer adsorption, $E_p$-$E_{3D}$, as a function of Nb doping concentration for both of the two surface terminations. For both termination types, without doping, the 3D one is more stable as suggested by the positive value of the energy difference. For both terminations, the energy difference becomes negative with a Nb doping concentration around 0.3%, indicating that the planar isomer becomes more stable. When the doping concentration further increases from 0.5% to around 1.9%, the absolute value of the energy difference increases from 0.4 eV to more than 1.2 eV for SrO termination, and from 0.1 eV to about 0.4 eV for $TiO_2$ termination. The variation of the energy difference is consistent with the change of the charge transfer (analyzed by Bader method[132]) between $SrTiO_3$ and supported Au clusters as shown in Fig. 3.3(b), from which we can see that when the doping concentration increases, the charge transfer between the P isomer and $SrTiO_3$ increases significantly faster than that of the 3D case, resulting in enhanced stability of the supported system with P isomer. Specifically, for $Au_8$ adsorption on SrO termination, without Nb doping, about $0.95e$ ($1.0e$) is transferred from oxide substrate to the supported metal clusters with 3D (P) structure. With increasing doping of Nb, charge transfer increases significantly for both structures and becomes about $1.5e$ ($2.1e$) for 3D (P) structure. Similar effects were also observed on $TiO_2$ termination, of which the charge transfer from $SrTiO_3$ to $Au_8$ is about

0.1$e$ for both 3D and P cases. When more Nb atoms are doped, charge transfer to the P structure increases rapidly and reaches 0.9$e$ when the doping concentration is 1.8%, but for 3D structure, the charge transfer increases just minimally and remains about 0.15$e$ with increasing dopants.

Table 3.1: Adsorption energies (in eV) of $Au_8$ clusters on SrO or $TiO_2$ terminated $SrTiO_3$ (001) surfaces under different Nb doping concentrations.

| Nb concentration | SrO | | | $TiO_2$ | |
|---|---|---|---|---|---|
| | 3D | P | | 3D | P |
| 0% | -3.07 | -2.56 | 0% | -1.21 | -0.84 |
| 0.52% | -3.16 | -3.35 | 0.48% | -1.12 | -0.98 |
| 1.04% | -3.32 | -4.15 | 0.96% | -1.17 | -1.18 |
| 2.08% | -3.65 | -4.73 | 1.92% | -1.07 | -1.29 |

In Table 3.1, we list the adsorption energies of both 3D and P isomers for different surface terminations and doping concentrations. Here, the adsorption energy $E_{ad}$ is calculated from, $E_{ad}$=$E_{Au8/SrTiO3(001)}$-($E_{Au8}$+$E_{SrTiO3(001)}$), where $E_{Au8/surface}$, $E_{Au8}$ and $E_{surface}$ denote the energies of the relaxed $Au_8$-substrate systems, of $Au_8$ clusters in the gas phase, and of the the clean surfaces, respectively. We can see that the adsorption energies for both 3D and P structures on SrO termination is larger than on the $TiO_2$ termination, by around 1.8 eV and 1.7 eV for two structures, due to the different reactivity of the two terminations. In addition, there is an enhanced stabilization of metal clusters with Nb doping in general, from 3.07 eV (2.56 eV) to 3.65 eV (4.73 eV) for 3D (P) structure on SrO termination, and from 0.84 eV to 1.29 eV for P structure on $TiO_2$ termination. Interestingly, the adsorption energy of P isomer on both terminations increases much faster than the 3D counterparts, thus resulting in a doping induced dimensionality crossover.

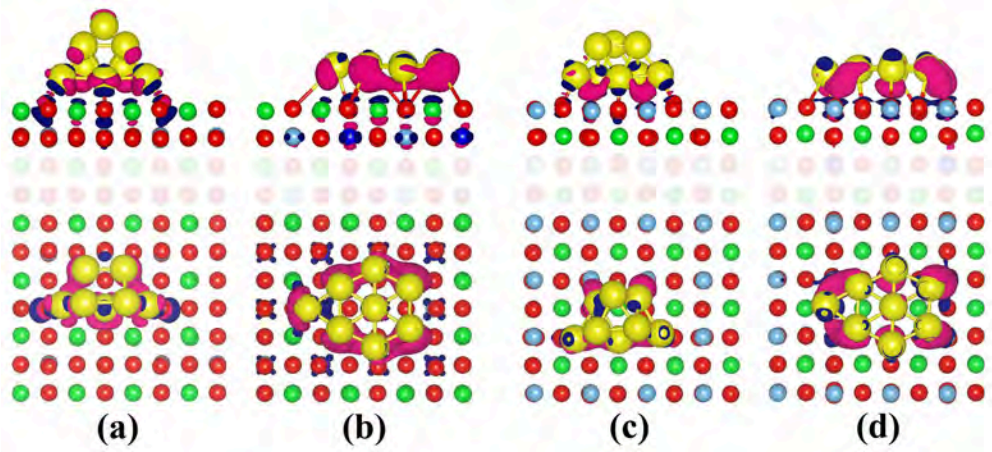


Figure 3.4: Side (upper panels) and top (lower panels) views of isosurfaces of differential charge density (isovalue=0.02 $e$/Å$^3$) for lowest-energy states of $Au_8$ clusters adsorbed on SrO (a, b) and $TiO_2$ (c,d) terminated surfaces. Note that the 3D and P isomer of $Au_8$ cluster correspond to cases with and without Nb doping, respectively. The differential charge density is calculated by: $\Delta\rho=\rho_{(Au_8@SrTiO_3(001))}-(\rho_{Au_8}+\rho_{SrTiO_3(001)})$. Blue and red colors indicate electron depletion and accumulation, respectively.

To see more clearly the MIT effects on the electronic structures of $SrTiO_3$ supported metal clusters, we plot the charge redistribution of the ground-state configurations for both pristine and Nb-doped surfaces in Fig. 3.4. It clearly shows that the supported Au clusters are negatively charged, and the charge redistribution mainly occurs at the contact region for all cases. The bonding between Au clusters and $SrTiO_3$ (001) surfaces involves d orbitals of Au atoms and 2p orbitals of neighboring O atoms, as shown in the interfacial region. It is also clear that compared to the case of Au clusters adsorbed on insulating surfaces (undoped cases), when adsorbed on metallic $SrTiO_3$ surfaces (doped cases), significantly more electrons are accumulated on $Au_8$ clusters (P configuration in this case), which is consistent with the Bader charge analysis (Fig. 3.3(b)). Note that this MIT-induced charge redistribution is different from Au nanoclusters adsorbed

on MgO/Mo(001) or other thin film systems, for which the charge accumulation of Au clusters and/or cluster-oxide interfacial region originates from the electron tunneling through oxide thin film from the underlying metal substrate,[72]; It also differs from the external electrical field driven charge distribution in oxide-supported metal cluster systems.[76]

## 3.5 Effects on the catalytic activity of supported Au clusters

It is widely accepted that the activation of molecular oxygen ($O_2$) is a crucial step for the aerobic oxidation reaction over gold catalysts, as shown in previous theoretical studies.[133, 134] The electronic charge transfer from gold nanoclusters to adsorbed $O_2$ results in the formation of peroxo- and superoxo-like species that are capable for selective oxidation of many chemical substances. Therefore, we then examine how the doping induced metal-insulator transition affects the $O_2$ adsorption on $Au_8$@$SrTiO_3$ (001) system. Our results show that the adsorption of $O_2$ can be greatly enhanced by Nb-doping induced metal-insulater transition. Taking $TiO_2$-terminated surface that is often observed in experiments as an example, without doping, the $O_2$ molecule does not bind to $Au_8$ clusters supported on the surface, similar to the case of $Au_8$ on pristine MgO (001) surface, [21, 79] and after doping, $O_2$ binds strongly on the Au cluster, with an adsorption energy around 0.9 $eV$ under the doping concentration of 1.92%. The effects of MIT on $O_2$ adsorption can be understood by electronic structures of the adsorbed

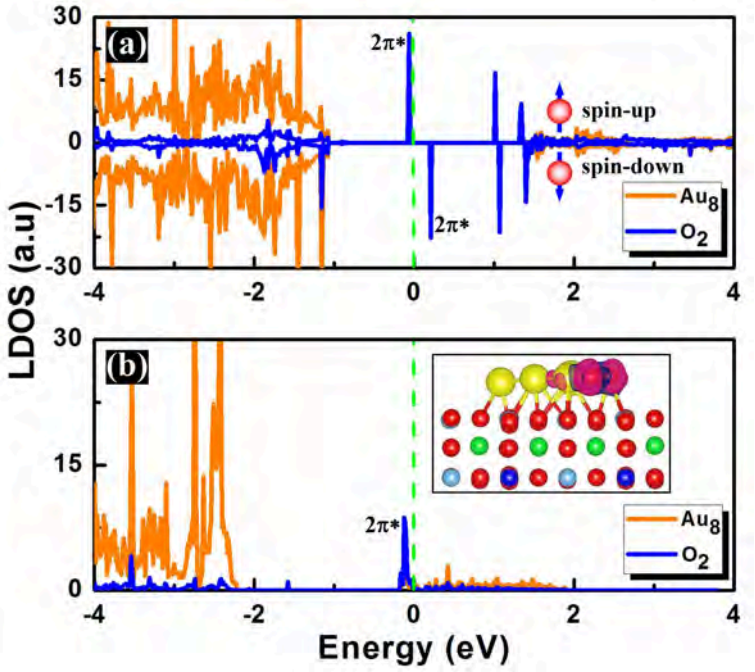


Figure 3.5: Local density of states (LDOS) projected onto the $O_2$ molecule and the $Au_8$ cluster for $O_2$@$Au_8$@$SrTiO_3$(001) for $TiO_2$-terminated surface without doping (a) and with Nb doping (1.92% of concentration) (b). Note that for the case without doping, the $O_2$ molecule is spin polarized. In the inset, the isosurface of charge redistribution is shown. The charge redistribution is calculated by: $\Delta\rho$=$\rho_{(Au_8@SrTiO_3(001))}$-($\rho_{Au_8}$+$\rho_{SrTiO_3(001)}$). Blue (red) color indicate electron depletion (accumulation). Fermi energy is set to zero.

system as plotted in Fig. 3.5. Local density of states (LDOS) projected on the Au cluster and $O_2$ molecule for the case of $Au_8$@$SrTiO_3$ without Nb doping are shown in Fig. 3.5(a). In this case, the Au cluster adsorbed surface is insulating with a bandgap around 2.5 $eV$. Both HOMO and LUMO orbitals of the $O_2$ molecule ($2\pi^*$ orbital of both spin channels) are deep inside the bandgap, close to the Fermi energy and far away from the valence and conduction bands of the supported Au cluster. The similar electronic

structures of $O_2$ compared to that of the molecule in the gas phase, suggests that the interaction between the molecule and the cluster is very weak. On the other hand, after doping, the Fermi energy of the surface is shifted into conduction bands, leading to the metal-insulator transition. As a consequence, the LUMO orbital of $O_2$ molecule (unoccupied $2\pi^*$ of spin-down channel) lies inside the conduction bands of the surface and the Au cluster also. The strong interaction between the unoccupied $2\pi^*$ orbital of $O_2$ and Au conduction bands leads to the population of electrons from Au cluster to $O_2$, pulling the $2\pi^*$ of $O_2$ down below the Fermi energy, as shown in LDOS of Fig. 3.5(b). Note that in this case, the $O_2$ molecule is not spin-polarized any more, like a peroxo-type structure. This metal-insulator-transition induced charge transfer can be further confirmed by the isosurface of charge redistribution plotted in the inset of the figure, from which the charge transfer from Au to $2\pi^*$ of $O_2$ can be clearly seen. Our calculations show that nearly 0.9 electrons transferred to $O_2$ in this case. Due to the charge transfer, the O-O bond is elongated to 1.43 Å from the gas phase value of 1.23 Å.

On the $SrTiO_3$ (001) surface with SrO termination, our calculations show that $O_2$ molecule can be adsorbed on the $Au_8$ cluster with an adsorption energy of 0.82 eV and O-O bond around 1.38 Å. With 2.08% of Nb dopant in the surface, the adsorption energy is further increased to 1.36 eV and O-O bond of $O_2$ molecule is enlarged to 1.52 Å. These results indicate that the doping induced MIT in $SrTiO_3$ has strong effects on the reactivity of supported metal clusters towards $O_2$ activation, no matter whether the surface is SrO- or $TiO_2$-terminated.

The significantly elongated O-O bond suggests the activation of the $O_2$ molecule. We then calculated the reaction barrier of catalyzed CO oxidation. The full cycle of the catalyzed CO oxidation has two steps. The first step is the reaction that breaks the O-O

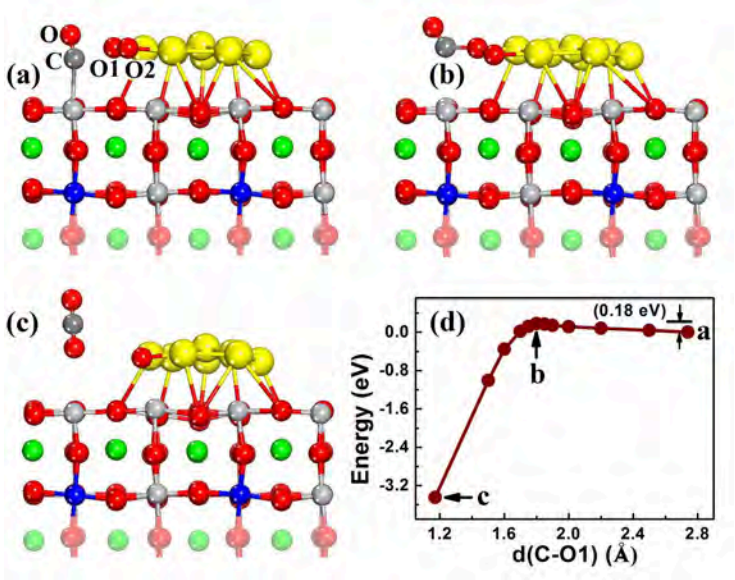


Figure 3.6: (a) The initial state of LH mechanism of CO oxidation catalyzed by $TiO_2$-terminated $Au_8/SrTiO_3$ (001) surface with Nb doping of 1.92%: d(O1-O2)=1.43 Å, d(C-O1)=2.74 Å. (b) The transition state: d(O1-O2)=1.51 Å, d(C-O2)=1.80 Å. (c) The final configuration with the formation and desorption of $CO_2$. (d) The energy profile along the reaction coordinate.

bond of $O_2$ and forms a $CO_2$ molecule, which is the major rate-limiting step and can be described as $CO+O_2 \longrightarrow CO_2+O$. The second step is the oxidation of another CO molecule that brings away the leftover O atom and restores the catalyst to its original configuration before the reaction ($CO+O \longrightarrow CO_2$). The reaction barrier of the second step normally is low. Two mechanisms of the reaction were investigated. One is the Langmuir-Hinshelwood (LH) type of reaction for which the CO molecule is adsorbed on the surface before the reaction, and the other one is the Eley-Rideal (ER) mechanism for which the CO molecule approaches the $O_2$ directly from free space. Our calculations predicted low barriers for both LH and ER reactions. In Fig. 3.6, we show the energy profile along the reaction coordinate for the first step of LH type of CO oxidation

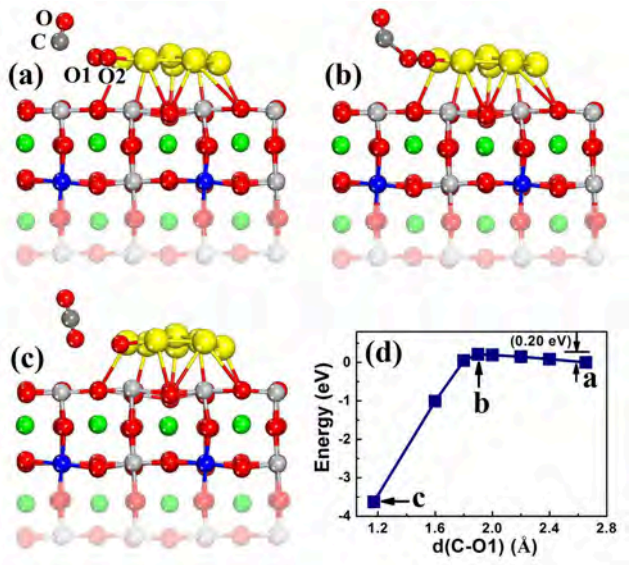


Figure 3.7: (a) The initial state of ER mechanism of CO oxidation catalyzed by the system as shown in Fig. 3.6: d(O1-O2)=1.43 Å, d(C-O1)=2.65 Å. (b) The transition state: d(O1-O2)=1.50 Å, d(C-O2)=1.90 Å. (c) The final configuration with the formation and desorption of $CO_2$. (d) The energy profile along the reaction coordinate.

catalyzed by $Au_8$ cluster (P isomer) adsorbed on $TiO_2$-terminated $SrTiO_3$ (001) surface (with 1.92% of Nb doping). Atomic configurations of initial, transition and final states are also shown in the figure. The reaction barrier $E_b$ in this case is estimated to be around 0.18 eV. The first step of ER type of reaction catalyzed by the same system is predicted to have a barrier about 0.2 eV. The atomic configurations for different reaction states and the energy profile along the coordinate are shown in Fig. 3.7.

Detailed analysis of the second step of the reaction (see Fig. 3.8) shows that the barrier is low (around 0.1 eV) as expected, indicating that the remaining oxygen atom is indeed very reactive. We also calculated the reaction barriers for CO oxidation catalyzed by $Au_8$ cluster on Nb-doped SrO-terminated surface. It is found that the reaction barrier

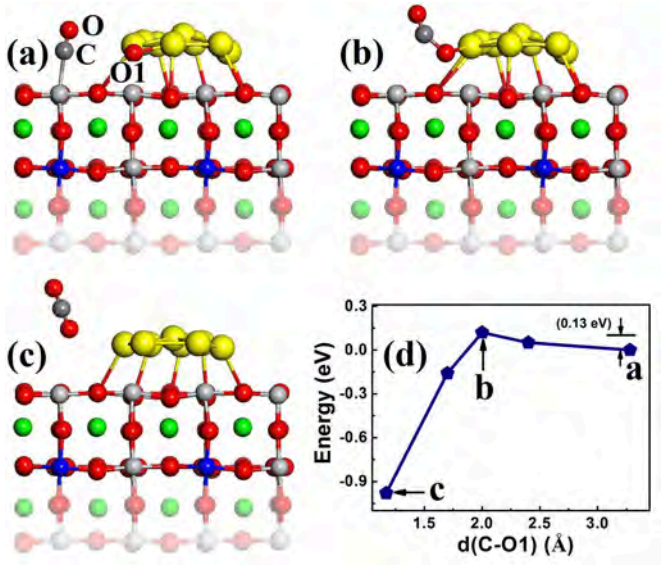


Figure 3.8: (a) The initial state of second step of CO oxidation with the remaining O atom by the system as shown in Fig. 3.6: d(C-O1)=3.28 Å. (b) The transition state: d(C-O2)=2.0 Å. (c) The final configuration with the formation and desorption of $CO_2$. (d) The energy profile along the reaction coordinate.

for the first step of CO oxidation for this case is around 0.12 (0.22) eV for the LH (ER) mechanism (see Figs. 3.9 and 3.10), and for the second step CO+O $\longrightarrow$ $CO_2$, a similar low barrier ($\sim$ 0.1 eV) as on $TiO_2$ termination is predicted.

## 3.6 Chapter summary

As metal-based heterogeneous catalysis is a subject of multi-disciplinary subject that calls for knowledge from physics, chemistry and other fields, it would be interesting and important if we can apply concepts in physics to the design and control materials in catalysis chemistry. In this work, via *ab initio* calculations, we demonstrated the effects

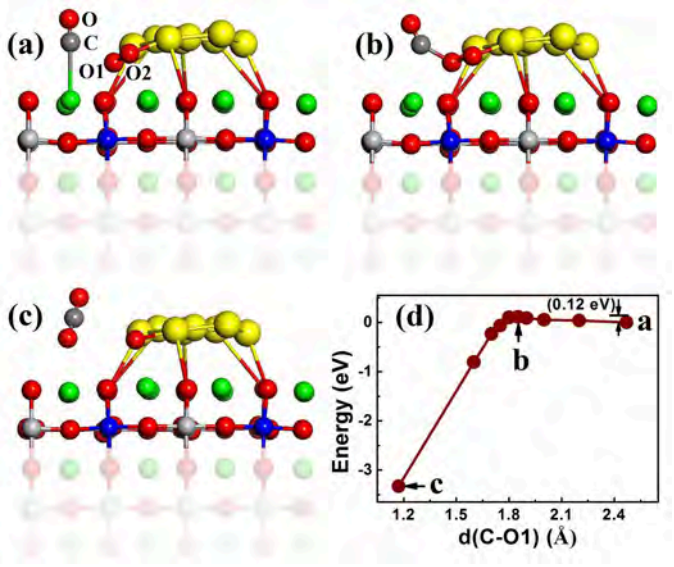


Figure 3.9: (a) The initial state of LH mechanism of CO oxidation catalyzed by SrO-terminated $Au_8/SrTiO_3$ (001) surface with Nb doping of 2.08%: d(O1-O2)=1.52 Å, d(C-O1)=2.46 Å. (b) The transition state: d(O1-O2)=1.56 Å, d(C-O2)=1.75 Å. (c) The final configuration with the formation and desorption of $CO_2$. (d) The energy profile along the reaction coordinate.

of doping induced metal-insulator transition in $SrTiO_3$, which is an important concept in condensed matter physics, on tuning the physical/chemical properties of supported Au nanocatalysts, which have never been discussed before.

We found that the Nb-doping induced metal-insulator transition significantly increases the chemical reactivity of $SrTiO_3$ surface that can be seen from the decrease of work function of the surface. The increased reactivity of the surface in turn causes the stabilization and dimensionality change of supported Au clusters. This can be understood as follows: Upon the doping induced MIT in $SrTiO_3$, the interaction between the Au clusters and the $SrTiO_3$ surface becomes much stronger, and as a result, the planar Au

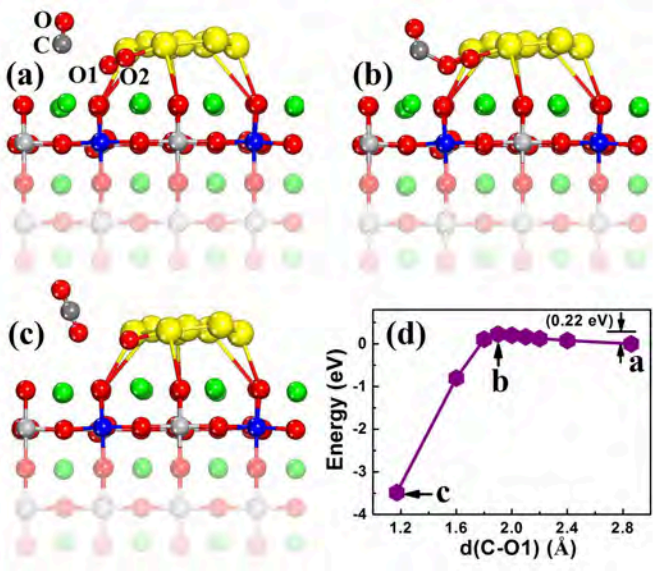


Figure 3.10: (a) The initial state of ER mechanism of CO oxidation catalyzed by the system as shown in Fig. 3.9: d(O1-O2)=1.52 Å, d(C-O1)=2.86 Å. (b) The transition state: d(O1-O2)=1.53 Å, d(C-O2)=1.90 Å. (c) The final configuration with the formation and desorption of $CO_2$. (d) The energy profile along the reaction coordinate.

clusters are preferred because of their large interface area. This mechanism is different from the methods by using an ultrathin film of MgO on an underlying metal substrate as the support or by placing the adsorbed systems in an electric field with a strength of the order of 1V/nm. Chemical-doping of oxide substrate may provide a more practical way to tune the morphology of supported clusters, and thus the mechanical, chemical, magnetic and thermal properties of these clusters can be also controlled.

The MIT in oxide were also found to greatly enhance catalytic activity of these clusters. On $Au_8$@$SrTiO_3$ for both SrO and $TiO_2$ terminations, with Nb doping, small reaction barriers of $\sim$0.2 eV were predicted for CO oxidation, indicating that this catalyzed reaction can readily happen at room temperature. Underlying the low barrier of CO oxidation

is the MIT induced interaction between $O_2$ antibonding $2\pi^*$ orbital and Au conduction bands, which leads to the population of electrons from Au to the antibonding orbital and the activation of the $O_2$ molecule. In present work we only studied $SrTiO_3$ substrate with the dopant of Nb, we believe that other oxides exhibiting MIT and using other dopants would also work. Besides doping, as discussed earlier, there are many other mechanisms that can also lead to the metal-insulator transition in oxide materials, such as defects [135], external field [136], and pressure.[137] We believe that the predicted strong effects of metal-insulator transition on catalytic activity of supported Au clusters are general (not limited to the doping mechanism), which provides a new methodology for the control of catalytic performance of TM-oxide supported metal clusters.

# Chapter 4

# Strain engineered stabilization and catalytic activity of metal nanoclusters on graphene

## 4.1 Introduction

In metal-based heterogeneous catalysis, strain is often introduced by changing the surface structure or by alloying. The effects of strain are often termed "electronic" and "geometric" effects.[138] The electronic effects originate from the local electronic structures of the surface that interact with the molecule reactants, which may be described in the *d*-band model.[139, 140] The geometric effect is "the rest", which is often related to the coordination number of adsorbate with respect to the surface atoms. The strained surfaces can be realized experimentally through ion implantation by a noble gas[141], or

involving evaporation of one metal into another (alloying).[142] For instance, pseudomorphic growth of one metal monolayer on the other yield highly strained surfaces.[143]

In this context, Nilekar et al.[144] used a combination of DFT calculations and an array of experimental techniques including in situ X-ray absorption spectroscopy to synthesize and test a class of bimetallic and ternary Pt-based alloys for oxygen reduction catalysis, and they found that strain mediated reactivity of Pt-monolayers on various supporting metals results in a optimization of oxygen binding energy in a way that the surface facilitates bond-making and bond-breaking reactions simultaneously. Kibler et al.[145] tried to tune the reaction rates of formic acid electrooxidation by lateral strain in a Pd monolayer grown on other metal surfaces. Aside from metal surface, strain effect on alloy metal nanoparticles were also reported. For instance, Strasser et al. reported the lattice-strain control of the activity in dealloyed core-shell Pt-Cu bimetallic nanoparticles, which has important applications in fuel cell catalysts.[146] More studies may be found in this direction (e.g. see Refs.[147–149]) and now lattice strain is regarded as a promising way to tune the properties of catalysts.

Despite these studies, using applied strain in the substrate to tune the performance of supported metal particles has never been discussed. For supported metal nanocatalysts, it will be interesting if we can control the properties of supported metal particles by modifying strain in the underlying support, because once the metal particles are deposited, it is difficult to directly apply strain in these clusters. In this chapter, we present an investigation aiming at controlling the stabilization and reactivity of metal nanoclusters adsorbed on substrate by tuning the mechanical strain of the underlying support. Here, graphene is chosen as catalyst support, due to the fact that it has excellent mechanical properties. Experiments have shown that a tensile strain up to 15% can be achieved in

graphene.[150, 151] Recent studies have shown that a 10% of strain can have significant effects on electronic or optical properties of graphene, which could lead to exciting new applications.[152, 153] For instance, Guinea et al. found that a designed strain could induce strong gauge fields that effectively act as a uniform magnetic field exceeding 10 T.[152] Wang et al.[154] and Wei et al.[155] found that the electric and thermal conductivity in graphene could be largely controlled by strain engineering.

In the current work, we focus on the effects of strain in graphene on the adsorption and reactivity of supported metal clusters that has never been discussed before. We show that a relatively small tensile strain (around 5%) applied in graphene can significantly enhance the stabilization of different kinds of metal clusters adsorbed on the graphene sheet and greatly reduce the reaction barrier of CO oxidation catalyzed by those nanoclusters. These findings may have important applications in the future design of graphene-based metal nanocatalysts.

## 4.2 Models and computational details

In this work, five different metal clusters, $Pt_4$, $Ag_7$, $Pd_9$, $Al_{13}$, and $Au_{16}$, which are often chosen in literature[156–158, 162, 163, 196] as examples of metal nanocatalysts, were considered. In Fig. 4.1, we show a schematic view of different metal clusters adsorbed on a stretched graphene sheet. The applied strain is defined as $\varepsilon = \Delta a/a_0$, where the lattice constants of unstrained and strained supercell equal to $a_0$ and $\Delta a + a_0$, respectively. Among all kinds of isomers of these clusters, we are mainly interested in those lowest-energy configurations as shown in the figure. The uniform tensile strain is

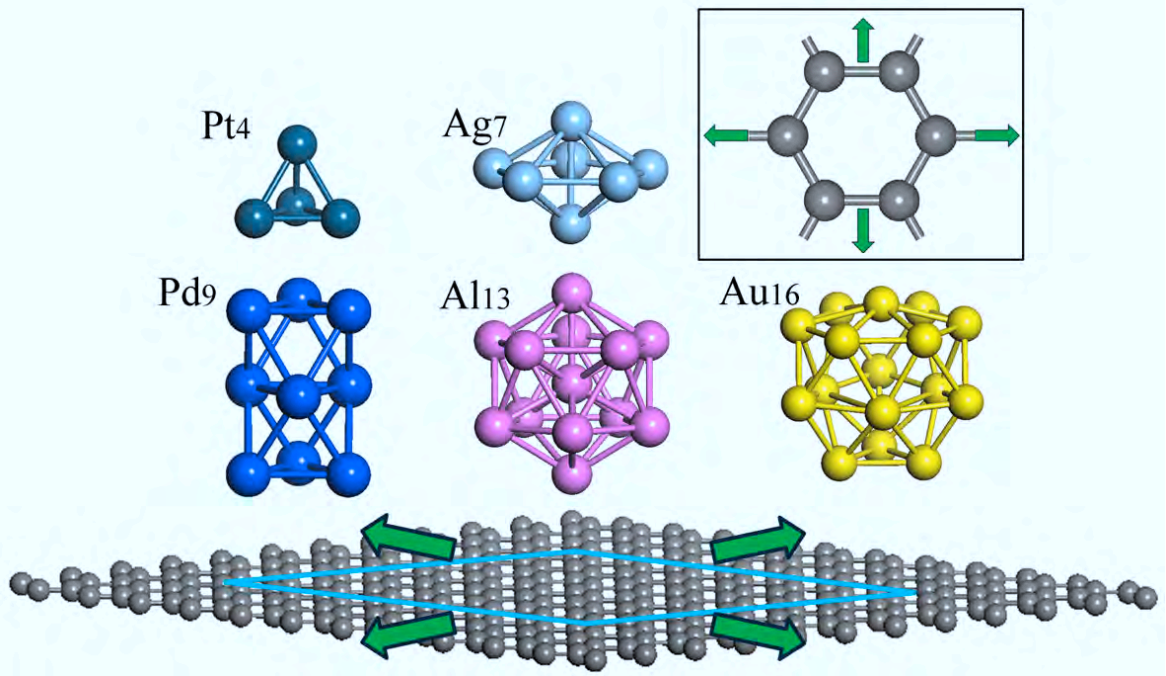


Figure 4.1: Schematic view of various metal clusters adsorbed on a stretched graphene sheet. Arrows show directions of stretching; Inset: The strain is applied uniformly in graphene along both zigzag and armchair directions.

applied in graphene along both zigzag and armchair directions as shown in the inset of the figure. We have considered different adsorption geometries and only the most stable optimized structures are considered and used for the calculation of chemical reaction.

First-principles electronic structure calculations are based on density functional theory using VASP package.[108] Reaction barriers under different strains were calculated by incorporating the constrained energy minimization method into VASP.[103, 104] The theoretical calculations were performed with a plane wave basis (30 Ry for the kinetic

energy cutoff), a 6x6 k-point sampling of Brillouin zone, and a scalar relativistic ultra-soft pseudopotential for transition metals.[97] In all calculations, the local spin density approximation and generalized gradient approximation in Perdew-Burke-Ernzerhof format[124] was included. A supercell that includes 6x6 unit cells of graphene (72 atoms) with periodical boundary conditions, and a vacuum region of 20 Å in the direction normal to the graphene plane (Z direction) was employed. In optimizing atomic structure, the force convergence criterion was set to 0.01 eV/Å.

## 4.3 Results and discussion

### 4.3.1 Strain weakening of C-C bonds in graphene

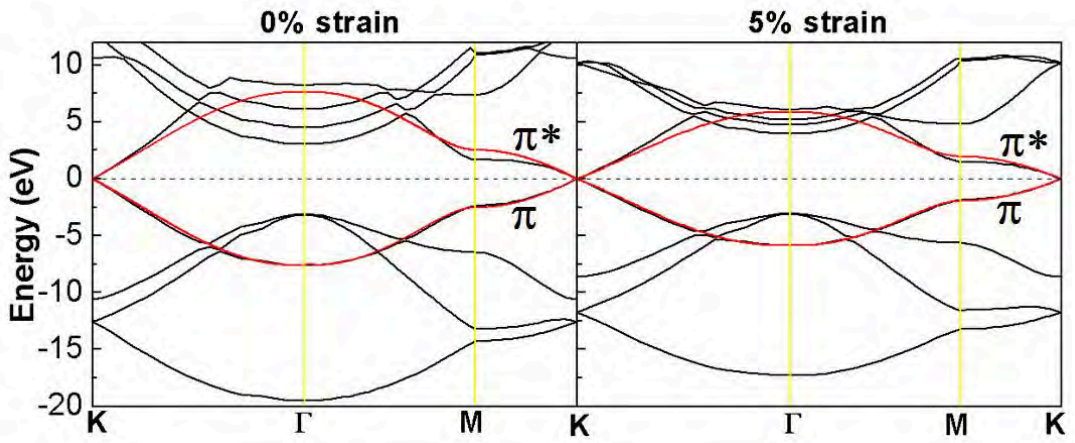


Figure 4.2: Band structures of the pristine graphene for two cases: 0% of strain (left panel), and 5% of strain (right panel). Red curves are from tight-binding calculations.

In the beginning, it is helpful to look at effects of such mechanical strain on electronic

properties and chemical reactivity of graphene that may have strong influences on catalytic activity of supported metal clusters. In Fig. 4.2, we show band structures of the pristine graphene under two different strains on the left panel (0% of strain) and the right panel (5% of strain) respectively. Black solid curves in the figure are from DFT calculations. Since the uniform strain as shown in Fig. 4.1 doesn't break the symmetry between two sublattices A and B, the graphene under strain is still gapless as we can see from the figure. The two band structures look similar except that the width of those bands significantly decreases for the case of 5% of strain. This can be understood by the fact that the interaction between carbon atoms becomes much weaker under strain. We are mostly interested in $\pi$ and $\pi$* bands near the Fermi energy which determine the chemical reactivity of graphene. In order to see strain effects on these two bands more clearly, we considered a single-orbital ($2p_z$ of carbon) nearest-neighbor tight-binding model as shown below,

$$\hat{H} = \sum_i \varepsilon_0 (a_i^\dagger a_i + b_i^\dagger b_i) - \sum_{i,j} t(a_i^\dagger b_j + h.c.), \tag{4.1}$$

where $a_i{}^\dagger$, $a_i$($b_i{}^\dagger$, $b_i$) denote the creation and annihilation of one electron in $2p_z$ orbital on the i'th carbon atom in the sublattice A (B), respectively. The hopping parameter *t* represents the coupling strength between $2p_z$ orbitals of two nearest-neighbor carbon atoms, one in sublattice A and another one in sublattice B. The term $\varepsilon_0$ is the onsite energy of the electron on the $2p_z$ orbital of each carbon atom. These two parameters, *t* and $\varepsilon_0$, can be fitted by DFT calculations. Red curves in Fig. 2a are from tight-binding calculations. Due to the neglect of hybridization between the $2p_z$ and other orbitals, the tight-binding model gives symmetrical $\pi$ and $\pi$* bands with respect to the

Fermi energy, and these bands agree well with DFT calculations around Dirac points as expected. In these calculations, the hopping parameter for the case of zero strain is set to be 2.6 eV, and under the 5% of strain, the hopping term is fitted to be 1.9 eV. The difference between these two hopping energies, 0.7 eV, is very significant and clearly suggests that a small strain of 5% in graphene greatly weakens the $\pi$ binding between carbon atoms, which may strengthen the interaction between the carbon $2p_z$ orbital and molecular orbital of adsorbed clusters, and in turn may greatly enhance the chemical reactivity of graphene.

### 4.3.2 Stabilization of metal clusters by strain

As the chemical reactivity of graphene can be affected by strain, we then examine the adsorption of various kinds of metal clusters on graphene and see how the applied strain can influence the properties of absorbed metal clusters. Without strain, except for $Pt_4$ and $Pd_9$ cluster, other three metal clusters under study are weakly adsorbed on graphene with adsorption energies around 0.4 eV, 0.2 eV, and 0.3 eV for $Ag_7$, $Al_{13}$, and $Au_{16}$, respectively. The adsorption energy of $Pt_4$ and $Pd_9$ cluster on graphene is calculated to be 1.3 eV and 1.0 eV. The difference in interaction between graphene and different metal clusters can be attributed to the intrinsic reactivity of these metal clusters, which is also found by Tomak et al.[165] Another relevant quantity besides the adsorption energy is the cluster-graphene adsorption distance that is defined as the distance between the graphene plane and the atom closest to the plane in the adsorbed cluster. This distance for the case of 0% of strain is found to be about 2.2 Å, 2.2 Å, 2.6 Å, 3.4 Å, 3.7 Å for $Pt_4$, $Ag_7$, $Pd_9$, $Al_{13}$, and $Au_{16}$ clusters, respectively. The relatively small adsorption energies

on graphene, compared to the cohesive energies in their bulk form, indicates that these clusters are highly mobile on graphene and tend to form bigger clusters. Similar results were also reported for metal clusters adsorption on other carbon nanomaterials, such as fullerene[160] and carbon nanotubes (CNTs),[161] for which the adsorption energies were found to be relatively small on pristine carbon structures, leading to clustering problems.

In Fig. 4.3, we show changes of cluster-graphene adsorption distances and adsorption energies for different metal clusters under different uniform strains. In general, for all metal clusters under study, the cluster-graphene adsorption distance decreases and the adsorption energy increases with strain. Specifically, the adsorption distances of $Al_{13}$ and $Au_{16}$ that have the largest cluster-graphene distance under zero strain, 3.4 Å and 3.7 Å, respectively, drop significantly with applied strain, reaching about 2.3 Å and 2.5 Å under a strain of 10%. The adsorption distance of $Ag_7$ cluster decreases about 0.2 Å under 10% of strain and $Pt_4$, $Pd_9$ decreases minimally ($\sim$ 0.1 Å). The shortened distance between adsorbed clusters and graphene under 10% of strain ($<$ 2.5 Å) suggests that more chemical bonds may be formed. Moreover, when the strain changes from 0% to 10%, adsorption energies of all clusters increase by at least 100%. In particular, adsorption energies increase by about 280%, 250%, 220%, 150%, 140% for $Al_{13}$, $Pt_4$, $Ag_7$, $Pd_9$, $Au_{16}$, respectively. Actually, as we can see from the figure, significant changes of cluster-graphene adsorption distances and adsorption energies start to occur at small strain of 5% for all clusters, indicating the significant strain-enhanced stabilization of these metal clusters on graphene. In Fig. 4.4, we show the detailed atomic configurations of these metal clusters adsorbed on graphene under the strain of 5%. Compared to the metal clusters adsorbed on strain-free graphene, it shows that on strained graphene,

metal clusters can be adsorbed with stronger covalent bonds.

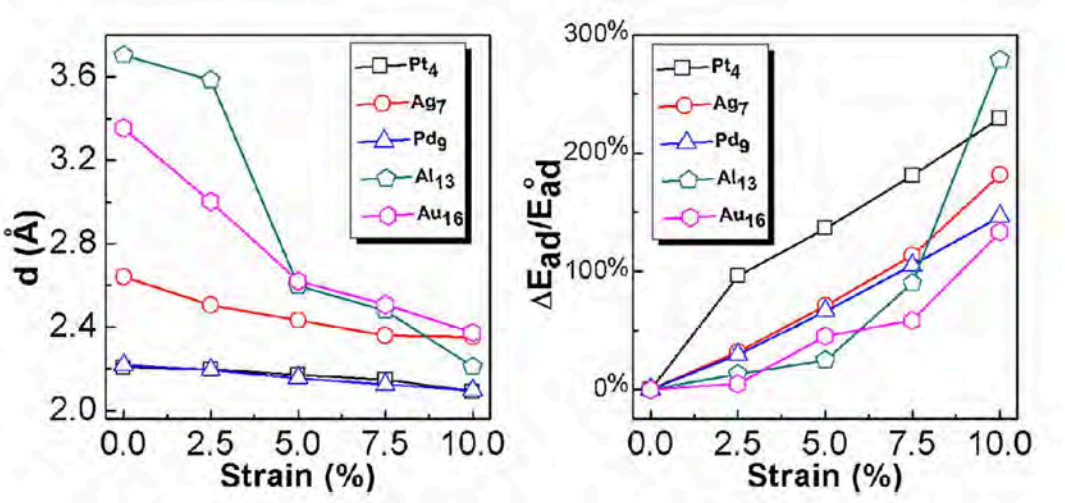


Figure 4.3: Left Panel: The variation of the adsorption distance (d) between the adsorbed cluster and graphene under different strains. Right Panel: The relative change of adsorption energy of different metal clusters on graphene. $E^0_{ad}$ is the adsorption energy for zero strain, and $\triangle E_{ad}$ is the change of the adsorption energy under strain relative to that of zero strain.

### 4.3.3 Tuning the charging state

The strong effect of strain in graphene on the adsorption of metal clusters implies the strain-dependent electronic properties of this kind of graphene-based systems. Next, we study the strain effects on electronic structures and reactivity of metal clusters supported on graphene. For support-induced reactivity, $Au_{16}$ may be the most interesting one among all clusters under study because previous studies have shown that both neutral and negatively charged $Au_{16}$ clusters are not reactive in vacuum,[163] so it is the best one to demonstrate effects of the underlying support. To illustrate the strain effects

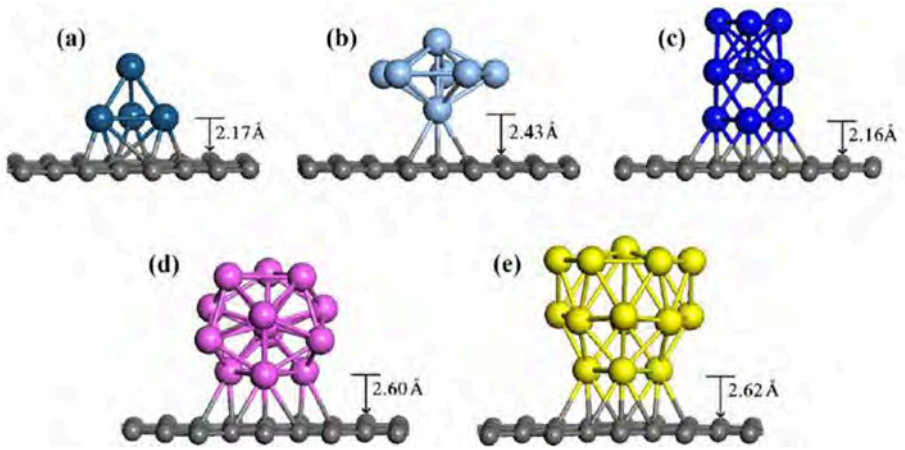


Figure 4.4: Local structures for (a) tetrahedral $Pt_4$, (b) pentagonal bipyramid $Ag_7$, (c) triangular prismatic $Pd_9$, (d) icosahedral $Al_{13}$ and (e) hollow cage $Au_{16}$ clusters adsorbed on a graphene sheet under a strain of 5%. The strain is applied in graphene both along zig-zag and armchair directions, as shown in the inset of Fig. 4.1.

on electronic properties of $Au_{16}$@graphene, we plot band structures of this system for two cases, 0% and 5% of strain, in left and right panels of Fig. 4.5(a), respectively. For 0% of strain, from the band structure, we can clearly see that in this case, electrons are transferred from graphene to $Au_{16}$, resulting in the downward shift of the Fermi energy from the Dirac point of the pristine graphene. The integration of the differential charge density above the plane cutting through the middle point of bonds between Au and graphene (see Fig. 4.5(b)) shows that around 0.2 electrons are transferred from graphene to $Au_{16}$, making Au clusters slightly negatively charged, which is in agreement with previous experimental and theoretical works.[164, 165] The enlarged view of the energy levels of HOMO, HOMO-1, HOMO-2 of the $Au_{16}$ cluster (flat bands), and the Fermi level of the whole system is also shown in Fig. 4.5(a). The linear behavior of the bandstructure around Dirac point resembles that of the pristine graphene, suggesting that the interaction between $Au_{16}$ and graphene in this case is weak. Note that

the Dirac point in this case appears at the center of the Brillouin zone due to the band folding in the supercell. Interestingly, when a 5% of strain is applied, the HOMO level of $Au_{16}$ for the case of zero strain is shifted upward to be well above the Fermi level, leading to significant charge transfer from $Au_{16}$ to graphene. Indeed, the same charge analysis shows that about 2.2 electrons in this case populated from the Au cluster to graphene, resulting in positively charged $Au_{16}$ clusters on graphene. The drastically distorted graphene band structure indicates the strong strain-induced interaction between graphene and $Au_{16}$, which breaks the symmetry between $\pi$ and $\pi$* bands at Dirac point, leading to a band gap around 0.4 eV. Thus, a small strain of 5% in graphene reverses the charge transfer between Au clusters and graphene, indicating the effective p-type or n-type doping of graphene may be efficiently controlled by Au cluster adsorption with external applied mechanical strain. Compared with other methods related to the electronic doping of graphene, such as the adsorption of organic molecules with different electron affinities,[166, 167] or the contact of metal surface with different work functions,[168], mechanical strain proposed here may provide a novel way for efficient doping of graphene.

In Fig. 4.5(b), we plot the isosurface of differential charge for $Au_{16}$@graphene under 5% of strain. In the figure, the red (blue) color denotes the accumulation (depletion) of electrons. Clearly, the strain-induced charge redistribution mainly occurs in the contact region between the cluster and graphene, originating from the strain-enhanced hybridization between carbon $2p_z$ and Au 5d orbitals, which is consistent with our analysis based on tight-binding calculations that the significantly weakened $\pi$ binding in graphene may enhance the interaction between carbon $2p_z$ orbital and adsorbed clusters.

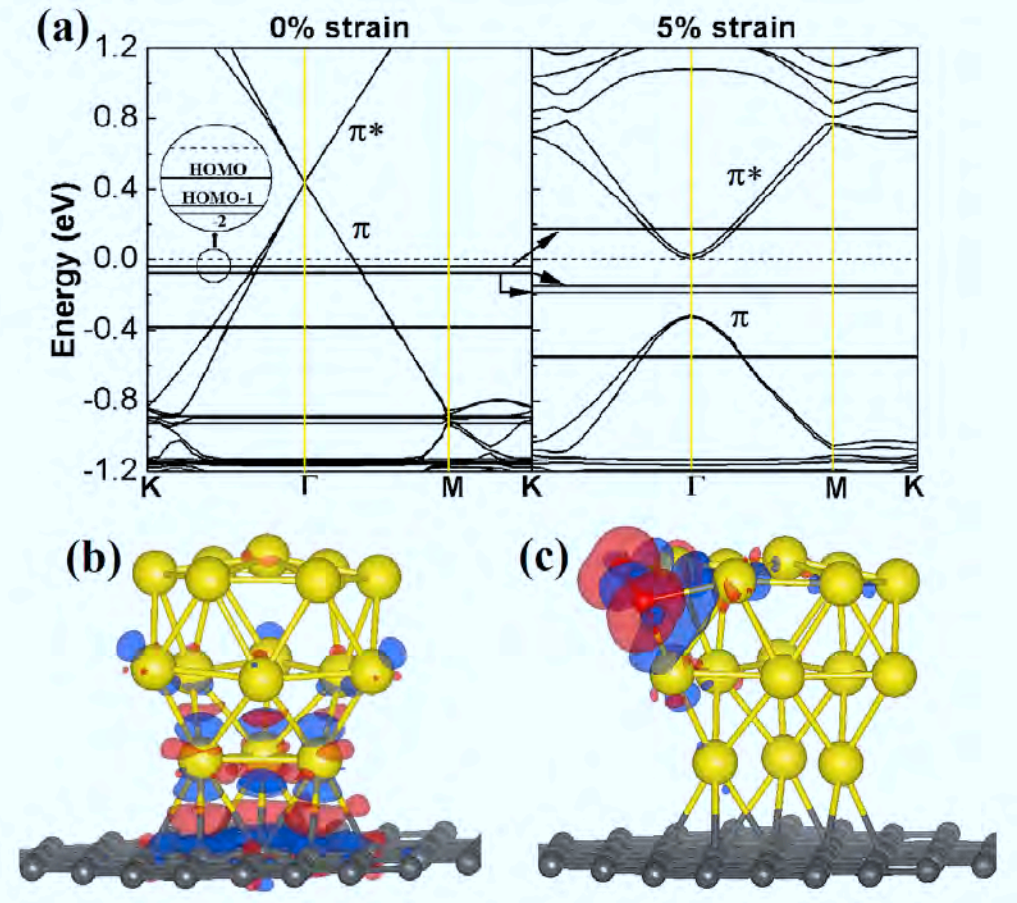


Figure 4.5: (a) The band structure of $Au_{16}$@graphene under zero strain (left panel) and 5% of strain (right panel). Inset: Enlarged view of energy levels of HOMO, HOMO-1, HOMO-2, of $Au_{16}$, and the Fermi level (dotted line) of the whole system. (b) Isosurface of the differential charge for $Au_{16}$@graphene when the graphene sheet is under a 5% of tensile strain. The differential charge density is calculated by $\Delta\rho=\rho_{(Au_{16}@graphene)}-(\rho_{Au_{16}}+\rho_{graphene})$. (c) Isosurface of charge redistribution for an $O_2$ molecule (in red) adsorbed on $Au_{16}$@graphene under the 5% of strain. The differential charge in this case is calculated by $\Delta\rho=\rho_{(O_2+Au_{16}@graphene)}-(\rho_{O_2}+\rho_{Au_{16}@graphene})$. The isovalue is set to 0.02e/Å$^3$. The accumulation (depletion) of electrons is in red (blue).

### 4.3.4 Strain engineering catalytic activity

We then probe the catalytic activity of strain-induced positively charged $Au_{16}$ clusters on graphene using the chemical reaction of CO oxidation. We first investigate the strain effects on adsorption of $O_2$ molecule on $Au_{16}$@graphene. As shown in Table 4.1, at strains less than 5%, $O_2$ molecule doesn't bind to any position of $Au_{16}$. When the strain changes from 5% to 10%, the adsorption energy of $O_2$ increases from 0.2 to around 0.5 eV. In Fig. 4.5(c), we plot the isosurface of the differential charge after the adsorption of $O_2$ on $Au_{16}$@graphene for the case of 5% of tensile strain, from which we can see the population of electrons from $Au_{16}$ onto the antibonding $2\pi$* orbital of $O_2$, leading to the greatly enlarged O-O bond length ( 1.42 Å) compared to its gas-phase value of 1.23 Å, resulting in the activation of $O_2$ molecule. The Bader charge analysis[132] shows that about 0.7 electrons transferred to $O_2$ when the strain is 5% or higher (Table 1).

After the adsorption of $O_2$, there is no co-adsorption of CO molecule on neighboring sites of $Au_{16}$. We therefore focused on the Eley-Rideal mechanism of CO oxidation, $CO+O_2 \longrightarrow CO_2+O$. For small strain (less than 5%), the reaction barrier of the CO oxidation is about the same as un-catalyzed reaction in vacuum, which is calculated to be around 3 eV, indicating that no reaction will happen at low temperature when there is no strain. When the strain is 5% or higher, the reaction barrier of ER mechanism of catalyzed CO oxidation, $E_b$, is estimated to be around 0.15 eV (see Table 1), which is regarded as a very low barrier. In Fig. 4.6, we show the energy profile along the reaction path and the detailed atomic configurations of the initial state, transition state, and final state. The low barrier of CO oxidation for strain 5% or higher is due to the strain-induced charge population onto the antibonding $2\pi$* orbital of $O_2$ as shown in Fig. 4.5(c). The

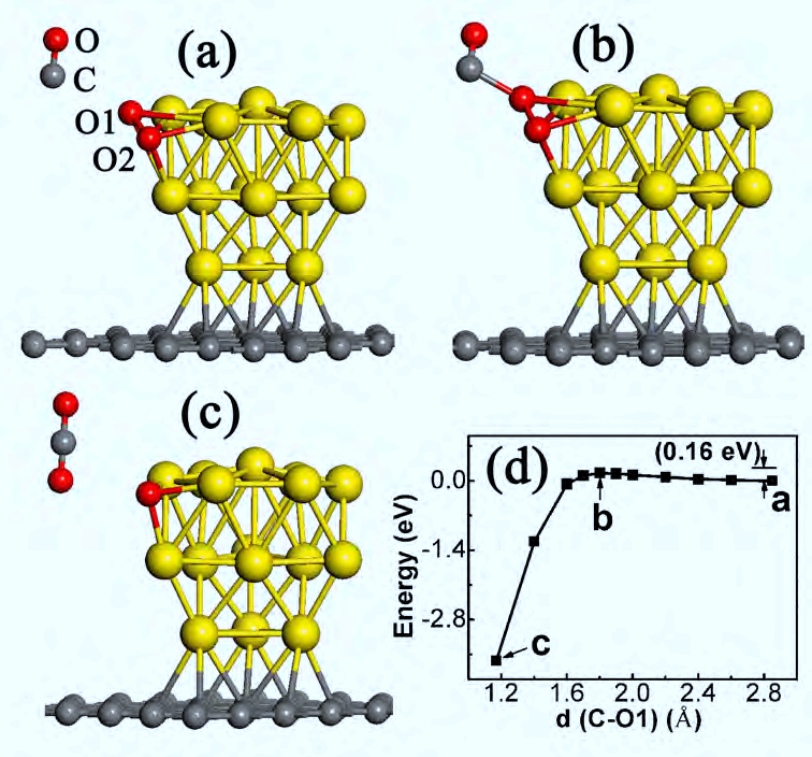


Figure 4.6: (a) The optimized initial state of ER mechanism of CO oxidation catalyzed by $Au_{16}$@graphene under a tensile strain of 5%: d(O1-O2)=1.41 Å, d(C-O1)=2.85 Å. (b) The transition state: d(O1-O2)=1.55 Å, d(C-O2)=1.80 Å. d(C-O)=1.18 Å. (c) The final configuration with the formation and desorption of $CO_2$. (d) The energy profile along the reaction coordinate.

barrier for the second step of the reaction, CO+O $\longrightarrow$ $CO_2$, turns out to be small ($<$ 0.2 eV) for all cases.

Another often-used Au nanocluster, $Au_8$ cluster, is also considered in current study. The adsorption of $Au_8$ clusters on graphene is a little bit more complicated. Unlike the case of normally used oxide supports for which $Au_8$ clusters always prefer the 3-dimensional (3D) structure,[72, 74, 131, 169] when adsorbed on graphene, the planar structure of $Au_8$ is slightly more stable with a total energy lower than the 3D one by about 0.2 eV,

Table 4.1: Strain effects on the adsorption of $O_2$ on $Au_{16}$@graphene and the reaction barrier of catalyzed CO oxidation. $d$(O-O) is the O-O bond length of the oxygen molecule; $\triangle$Q denotes the charge transferred to $O_2$ after the adsorption; $E_{ad}$ is the adsorption energy of $O_2$ calculated from $E$($O_2$+$Au_{16}$@graphene)-($E$($O_2$)+$E$($Au_{16}$@graphene)), and $E_b$ is the calculated reaction barrier of ER type of CO oxidation catalyzed by $Au_{16}$@graphene. The reaction barrier under strain 0.0% or 2.5%, 3.1 eV, corresponds to the barrier of uncatalyzed CO oxidation in gas phase.

| Strain | $d$(O-O)(Å) | $\triangle Q(e)$ | $E_{ad}$ (eV) | $E_b$ (eV) |
|---|---|---|---|---|
| 0.0% | 1.23 | 0.0 | Unbound | 3.10 |
| 2.5% | 1.23 | 0.0 | Unbound | 3.10 |
| 5.0% | 1.41 | -0.68 | 0.20 | 0.16 |
| 7.5% | 1.42 | -0.68 | 0.26 | 0.15 |
| 10% | 1.42 | -0.69 | 0.46 | 0.15 |

Table 4.2: Strain effects on adsorption of 3D $Au_8$ cluster on graphene. Note here the significant decrease of d(Au-graphene) when the strain varies from 2.5% to 5%.

| Strain | $d$($Au_8$-graphene) (Å) | $E_{ad}$ (eV) |
|---|---|---|
| 0.0% | 3.41 | 0.56 |
| 2.5% | 3.31 | 0.57 |
| 5.0% | 2.88 | 0.59 |
| 7.5% | 2.39 | 0.65 |
| 10% | 2.32 | 0.69 |

similar to the energy difference of these clusters in the gas phase. At room temperature, 3D and planar clusters may co-exist due to the small energy difference. We therefore

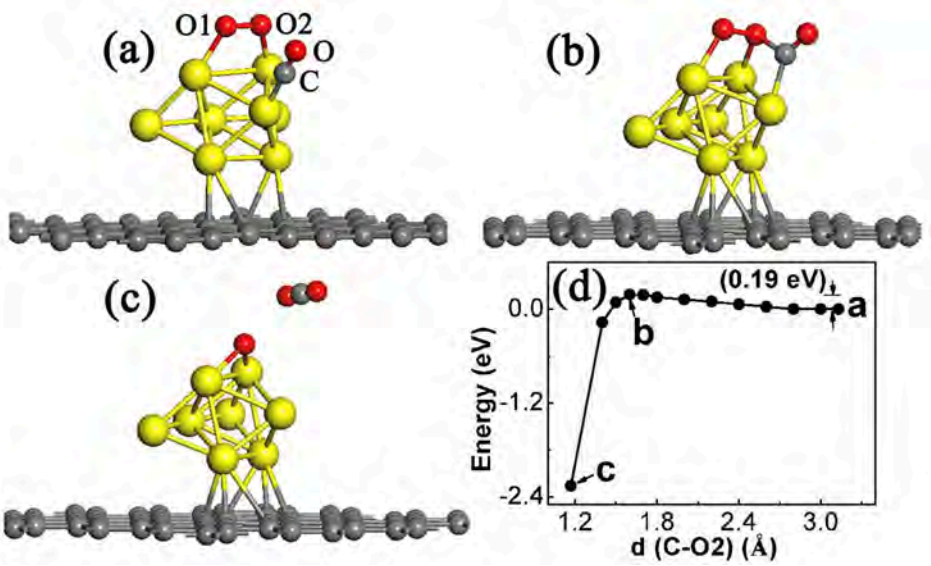


Figure 4.7: LH type of CO oxidation catalyzed by 3D $Au_8$@graphene for the case of 5% strain (a) Initial state: d(O1-O2)=1.41 Å, d(C-O)=1.15 Å, d(C-O2)=3.13 Å. (b) Transition state of the reaction: d(O1-O2)=1.46 Å, d(C-O)=1.18 Å. d(C-O2)=1.6 Å. Final state: the formation of $CO_2$. (d) Energy profile along the reaction coordinate.

investigated the strain effects on CO oxidation catalyzed by both 3D and planar $Au_8$ clusters on graphene. For the 3D $Au_8$, similar to $Au_{16}$, when the uniform tensile strain increases from 2.5% to 5%, a significant decrease of Au-graphene adsorption distance d(Au-graphene) occurs (see Table 2). Overall, the distance decreases from 3.4 Å (under no strain) to around 2.3 Å (under 10% strain). In the mean time, the co-adsorption energy of $O_2$ and CO molecules changes from around 1 eV to 1.4 eV, and the O-O bond length increases from 1.26 Å to 1.41 Å. For this case, our calculations show that the catalyzed CO oxidation prefers the Langmuir-Hinshelwood mechanism. The reaction barrier of the catalyzed CO oxidation greatly drops from 2.6 eV to less than 0.2 eV (see Table 3) when the strain varies from 0% to 5%. The optimized structures of the initial state, the transition state, and the final state and the detailed reaction profile is

Table 4.3: Strain effects on co-adsorption of $O_2$ and CO molecules, and reaction barrier of LH type of CO oxidation on 3D $Au_8$@graphene. Note here the significant increase of O-O bond length and the adsorption energy when the strain varies from 2.5% to 5%.

| Strain | $d$(O-O)(Å) | $E_{ad}$ (eV) | $E_b$ (eV) |
|---|---|---|---|
| 0.0% | 1.25 | -1.04 | 2.85 |
| 2.5% | 1.26 | -1.03 | 2.60 |
| 5.0% | 1.41 | -1.37 | 0.19 |
| 7.5% | 1.40 | -1.41 | 0.26 |
| 10% | 1.40 | -1.43 | 0.22 |

demonstrated in Fig. 4.7. For planar $Au_8$, the strong adsorption of $O_2$ occurs when the strain reaches 10%, and no co-adsorption of CO is found after the adsorption of $O_2$. The reaction barrier of ER type of catalyzed reaction under 10% of strain is estimated to be 0.12 eV.

## 4.4 Chapter summary

In this chapter, we demonstrate by first-principles investigation a novel method of controlling the stabilization and catalytic activity of metal nanoclusters supported on graphene via tuning the mechanical strain in graphene. Our calculations found that an applied strain in graphene can decrease the adsorption distance and greatly increase the adsorption energies of different metal clusters under study by at least 100% at a strain of 10%, suggesting highly enhanced stabilization of these metal clusters on graphene, which is

highly desired in real applications of metal nanocatalysts. By using tight-binding calculations together with DFT, we found that the origin of this enhanced stability is the greatly weakened $\pi$ binding in graphene that increases the interaction between carbon $2p_z$ orbital and adsorbed metal clusters.

By analyzing the electronic structures, we found that the charging state of the supported metal clusters can be tuned on graphene substrate. Interestingly, with the adsorption of Au clusters, the p-type or n-type doping of graphene can be efficiently controlled by applying a mechanical strain in graphene, opening up a new method to modify the properties of graphene for electronic applications. As a stretchable thin film, in graphene, the strain-induced reversal of charge transfer may lead to other applications, such as strain engineered hydrogen storage on metal-decorated graphene,[170] or strain-tunable magnetism if supported clusters or molecules are magnetic,[171, 172] which is of fundamental importance to design new hydrogen storage media and spintronic devices.

Furthermore, by using $Au_{16}$ and $Au_8$ clusters adsorbed on graphene as model catalysts for chemical reaction of CO oxidation, we found that a 5% of strain can decrease the reaction barrier of $CO_2$ formation from around 3 eV to less than 0.2 eV. Underlying the enhanced enhanced catalytic capability is attributed to the strain-induced charge transfer from the Au@graphene interfacial region to antibonding $2\pi^*$ orbital of the adsorbed $O_2$ molecule, leading to the activation of O-O bond. Experimentally, strain in graphene can be introduced by stretching the soft substrate (such as polydimethylsiloxane, PDMS) on which graphene is supported, or by nanoindentation with the help of atomic force microscope.[150, 151] Compared with intrinsic lattice strain in metal catalysts, which may be introduced by doping with noble gas atoms or by metal alloying, this externally applied strain is of great interest in a sense that it can reversibly control the performance

of metal nanocatalysts. We expect these novel results to provide new opportunities in the future design and applications of graphene-based supported metal nanocatalysts, as well as the further development of mechano-chemistry[173, 174] for which the focus is the interplay between the mechanical force and chemical reactions.

# Chapter 5

# Defects in graphene towards supported metal nanocatalysts

## 5.1 Introduction

Due to the imperfection of material production processes, impurities and defects are always present in crystals. Such structural imperfections have a strong influence on the electronic, optical, thermal and mechanical properties of solids. Actually, many of the characteristics of technologically important materials such as the conductance of semiconductors, the mechanical strength and ductility of metals, and the chemical reactivity of oxides are governed by defects.[175]

Defects in bulk crystals have been extensively studied for many years. Two dimensional crystal structures, however, have been considered only recently. Since the first

isolation of single-layer graphene by mechanical exfoliation,[40] there has been a surge of research pertaining to its unique properties and potential applications for the next-generation electronic devices, especially after large-scale synthesis methods like chemical vapor-deposition[150, 176] and epitaxial growth.[177, 178] The properties of graphene were expected to be outstanding, and many theoretically predicted properties have now been confirmed in experiments.[188] Some of these properties can only be observed at extremely low defect concentration, which is possible because of the high formation energies of point defects in graphene, Nevertheless, like in any other bulk materials, structural defects do exist in graphene and can dramatically alter its properties. Defects can also be deliberately introduced into graphene by irradiation or chemical treatment.

In monolayer graphene, defects can be rather complex due to the fact that the $sp^2$-hybridized carbon atoms can arrange themselves into a variety of different polygons, not only hexagons, to different structures. The nonhexagonal rings may also introduce curvature in the sheet or leave it flat when certain symmetry rules are satisfied by the polygon arrangement. These properties does not appear in other 3D bulk crystals. Point defects such as single or multiple carbon vacancies, interstitial atoms and Stone-Wales defects, are zero-dimensional, whereas dislocations of carbon atoms are one-dimensional lines of defects. Grain boundaries or stacking faults extend in two dimensions. Several experimental studies have shown the occurrence of either native or physically introduced defects in graphene, and images of defective graphene with atomic resolution have been obtained by using transmission electron microscopy (TEM)[189–192] or scanning tunneling microscopy (STM).[193, 194]

In this chapter, we studied the effect of defects in graphene on the catalytic performance of supported metal clusters. We have considered both Au and Pt nanoclusters supported

on pristine (defect-free) and defective graphene, and investigated their stability and catalytic activity towards CO oxidation. Our findings demonstrate that the single-carbon-vacancy defect in graphene, which has been observed in experiments,[195] plays an essential role in stabilization and activation of supported metal clusters. These results may also be extended to other kinds of defects in graphene.

For structural optimization and electronic structure calculations, the first principles method based on DFT was employed via the computational package VASP.[108] The reaction barrier of catalyzed CO oxidation was calculated by incorporating the constrained energy minimization method into VASP. DFT calculations were performed with a plane wave basis with a cutoff energy of 400 eV, a 6x6 K-points sampling of Brillouin zone, and a scalar relativistic ultra-soft pseudopotential for Au and Pt.[97] In all calculations, the generalized gradient approximation in Perdew-Burke-Ernzerhof format[124] was included. A supercell that includes 6x6 unit cells of graphene in graphene plane, and a vacuum region of 20 Å in the direction normal to graphene plane (Z direction) was adopted. In optimizing atomic structures, the force convergence criterion was set to 0.01 eV/Å.

## 5.2 Results and discussion

### 5.2.1 Anchoring of metal clusters by a single carbon vacancy

In this study, $Au_8$ and $Pt_4$ clusters supported on graphene were chosen to be model catalysts of the chemical reaction of CO oxidation. For Au octamer, the two isomers

including one planar structure (P2) and a 3D one as discussed in Chapter 4, as well as another planar structure (P1), which was found to be slightly more stable than P2 in the gas phase,[123] were considered. The structures for P1, P2 and 3D are shown in Figs. 5.1(a), (b) and (c), respectively. As discussed in the previous chapter, when adsorbed on metal oxide materials, $Au_8$ clusters prefer to take the form of the 3D structure as shown in Fig. 5.1(c). In contrast, when adsorbed on pristine (defect-free) graphene, our calculations found that two planar structures as shown in Figs. 5.1(a-b) are nearly degenerate, and slightly more stable than the 3D one by about 0.4 eV. Actually, the energy difference of the three systems is closely related to the energy of these clusters in the gas phase, as calculations show that in the gas phase, P clusters are slightly more stable than the 3D one by around 0.4 eV. At room temperature, they may co-exist. We therefore considered all these three $Au_8$ clusters as catalysts for chemical reaction. For $Pt_4$ clusters, here we consider the commonly used 3D tetrahedral structure, because of the fact that in experiment,[43] Pt subnanoclusters which contain only a few atoms supported on graphene sheet, were found to have high electrocatalytic activity, and in another experiment,[156] size-preselected $Pt_4$ clusters stabilized on high-surface-area supports were found to be 40-100 times more active for the oxidative dehydrogenation of propane than conventional platinum and vanadia catalysts.

Various kinds of adsorption configurations of these metal clusters were calculated and compared before analyzing their electronic structures. When the underlying graphene sheet is defect free, the adsorption energies for three configurations of $Au_8$ clusters were found to be 0.71 eV (P1), 0.65 eV (P2), and 0.52 eV (3D), and the cluster-graphene adsorption distance were found to be around 3.8 Å for the two planar structures (P1, P2) and 3.5 Å for the 3D structure. The adsorption energies were also found to be fairly

insensitive to adsorption sites, particular for the two planar structures, indicating that these clusters can diffuse pretty easily on graphene. For $Pt_4$ cluster, as also discussed in Chapter 4, there is a quite strong interaction between the cluster and graphene with an adsorption energy of 1.4 eV and adsorption length 2.2 Å. However, this adsorption energy is still much smaller than the cohesive energy of Pt in the bulk form ($\sim$ 5.84 eV[175]), which implies that bigger Pt crystals will form on pristine graphene during cluster deposition.

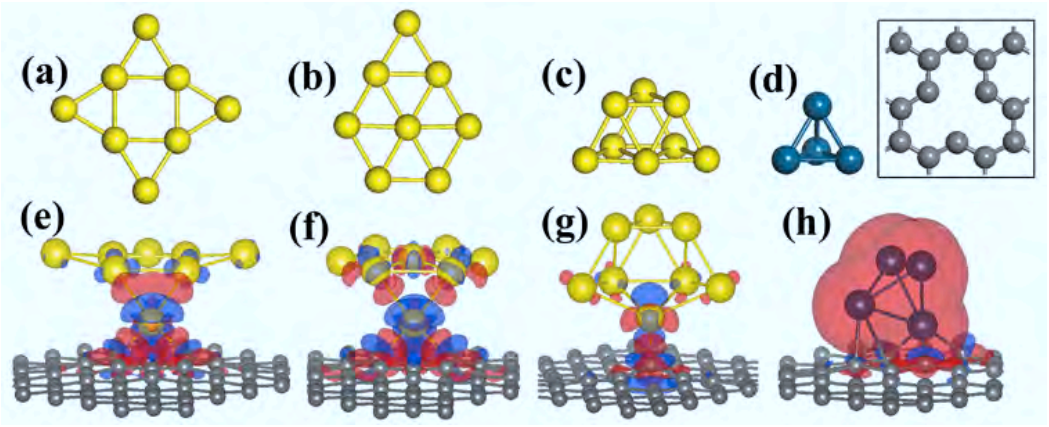


Figure 5.1: (a-c) Three most stable isomers of $Au_8$ clusters in gas phase (Au in yellow): (a) P1, (b) P2, and (c) 3D. (d) $Pt_4$ cluster (dark blue) in gas phase. (e-h) Configurations for Au and Pt clusters adsorbed on defective graphene (C in grey). Superimposed we show an isosurface of the excess electronic charge (red) and depleted electronic charge (blue), with an isosurface value of 0.02e/Å$^3$. In the inset, we show the atomic structure of a single-carbon-vacancy in graphene.

We then introduced a single-carbon-vacancy defect in a 6×6 supercell of graphene, which corresponds to a defect concentration of about 1.39% (as shown in the inset of Fig. 5.1), and focused our study on this simplest defect towards the adsorption of $Au_8$ and $Pt_4$ clusters on top of it. When a single vacancy is generated by removing one carbon atom

from graphene sheet, a partial relaxation of the defective graphene sheet is observed, with two of the three unsaturated carbon atoms at vacancy "shrink" to its two neighboring carbon atoms, resulting in a shorter optimized C-C bond (by about 0.5 Å) compared with pristine graphene. Our calculations show that this single vacancy has strong effect on the binding on adsorbed metal clusters. It is found that the nearest Au-C bond distances are between 2.05 Å to 2.1 Å for three $Au_8$ isomers, and the adsorption energies increase to 1.56 eV, 1,52 eV, 1.51 eV for P1, P2 and 3D isomer, respectively. In these relaxed structures, one of the Au atom is located directly on top of the carbon vacancy, rendering a larger adsorption energy compared to the cases of pristine graphene.(see Fig. 5.1(e-g)) The most stable configuration of the supported $Pt_4$ cluster consists of one atom interacting with the carbon vacancy (Pt-C bond distances about 1.98 Å) and another atom adsorbed on top a carbon atom near the vacancy, leading to a high adsorption energy of 7.7 eV. The origin of this greatly enhanced binding is the strong interaction between the carbon-vacancy defect in graphene and the adsorbed metal clusters originating from the defect-enhanced hybridization of carbon 2p and Au/Pt 5d orbital, which can be seen from the isosurface of charge redistribution shown in Figs. 5.1 (e-h). For $Au_8$ clusters, the significant charge redistribution only happens in the interfacial region between the defect in graphene and the adsorbed clusters, and for case of $Pt_4$ cluster, the defect drastically change the electronic structure of the whole cluster, leading to the surprisingly high adsorption energy (7.7 eV).

### 5.2.2 Activation of metal clusters

Next we turned to investigate the catalytic activity of these clusters. When the underlying graphene sheet is defect free, our calculations showed that the $O_2$ molecule doesn't bind to the $Au_8$ cluster adsorbed on the graphene regardless of its geometry (planar or 3D), just like the case of pristine MgO (001) surface supported $Au_8$ clusters[21, 79] as discussed in the previous chapter, indicating that $Au_8$ clusters are not catalytically active for $O_2$ for this case. Therefore, the reaction barrier of CO oxidation in this case is the gas-phase value 3.1 eV (DFT calculation). For the case of $Pt_4$ cluster, the $O_2$ molecule binds to the $Pt_4$ cluster adsorbed on defect-free graphene with a binding energy of 0.9 eV and the O-O bond length of 1.39 Å. We then investigated two types of reactions of CO oxidation catalyzed by $Pt_4$@graphene: the Langmuir-Hinshelwood type, and the Eley-Rideal type. The reaction barrier of the catalyzed CO oxidation was estimated by our calculations to be around 0.5 eV for both LH and ER types of reactions.

In light of the inactivity of $Au_8$ clusters and the relatively low reactivity (high barrier) of $Pt_4$ clusters on defect-free graphene which is against the experimental observations,[43] we studied the catalytic activity of $Au_8$ and $Pt_4$ clusters adsorbed graphene with defects. As the significant defect-induced changes of electronic structures of Au/Pt clusters are expected to have great effects on the adsorption of the $O_2$ molecule on clusters, and in turn to drastically influence the catalyzed reaction of CO oxidation.

After the carbon vacancy is introduced, the $O_2$ molecule strongly binds to all three types of $Au_8$ clusters with the adsorption energy 1.34 eV for P1, 1.26 eV for P2, and 1.18 eV for 3D structure, respectively. The adsorption energy of $O_2$ on the $Pt_4$ cluster changes

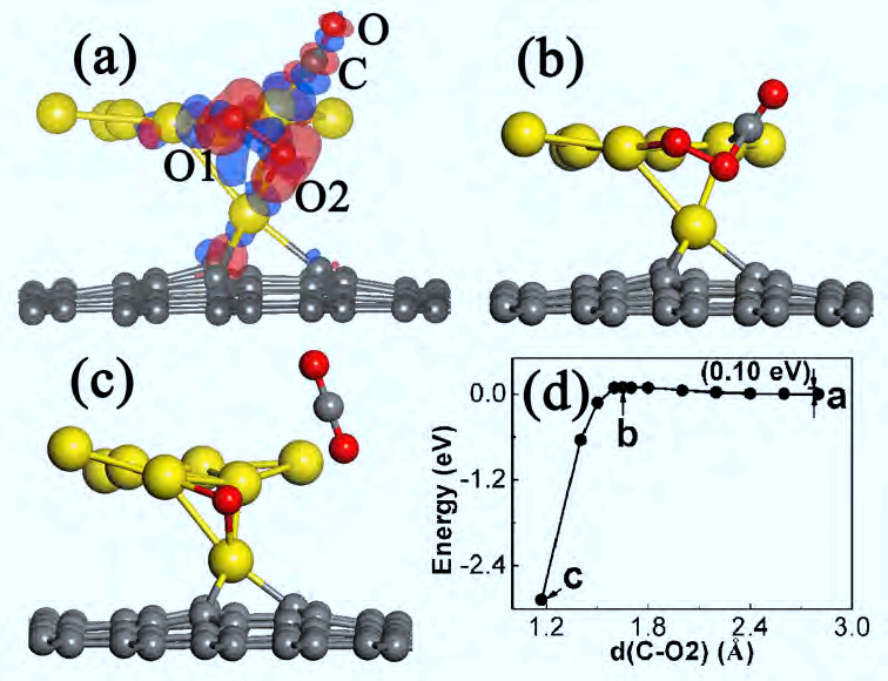


Figure 5.2: LH type of CO oxidation catalyzed by the P1 isomer of $Au_8$ on the defective graphene. (a) The initial state of the reaction: d(O(1)-O(2))=1.41 Å, d(C-O(2))=2.81 Å. The isosurface of excess (red) and depleted (blue) electronic charge is also shown here. (b) The transitional state: d(C-O(2))=1.65 Å, d(O(1)-O(2))=1.50 Å. (c) The final state of forming $CO_2$. (d) The energy profile along the reaction coordinate d(C-O(2)).

from 0.90 eV to 1.92 eV after the defect is introduced. When adsorbed on $Au_8$ ($Pt_4$) clusters on defective graphene, the O-O bond of the $O_2$ molecule is significantly elongated compared to its gas-phase value (1.23 Å). In particular, the O-O bond length, d(O-O), is around 1.41 Å for all three types of $Au_8$ clusters, and 1.44 Å for the $Pt_4$ cluster. As shown in Figs. 5.1(h) and 5.5(a), there is a dramatic structural change of $Pt_4$ cluster upon $O_2$ adsorption. This structural fluxionality is often observed in small metal clusters and may account for their unique physical and chemical properties.[179, 180] The great elongation of the O-O bond is due to electrons populated to the anti-bonding $2\pi^*$

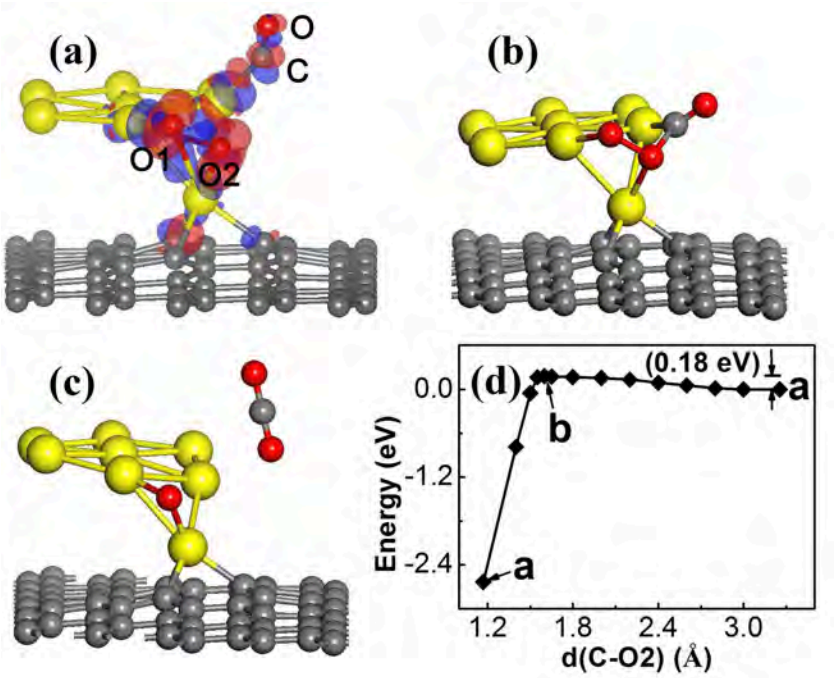


Figure 5.3: LH type of CO oxidation catalyzed by the P2 isomer of $Au_8$ on the defective graphene. (a) The initial state of the reaction: d(O(1)-O(2))=1.42 Å, d(C-O(2))=3.26 Å. The isosurface of excess (red) and depleted (blue) electronic charge is also shown here. (b) The transitional state: d(C-O(2))=1.60 Å, d(O(1)-O(2))=1.48 Å. (c) The final state of forming $CO_2$. (d) The energy profile along the reaction coordinate d(C-O(2)).

orbital of the $O_2$ molecule mainly from the metal cluster for the case of $Au_8$ and from both the metal cluster and the interfacial region for the case of $Pt_4$, as we can see from the Figs. 5.2(a), Fig. 5.3(a), and Fig. 5.4(a). The Bader charge population analysis[132] showed that about 0.7 (0.9) electrons are transferred to the $O_2$ molecule for the case of $Au_8$ ($Pt_4$) clusters.

Next we studied both LH and ER types of CO oxidations catalyzed by $Au_8$ or $Pt_4$ clusters pinned on graphene by a single-carbon-vacancy defect. In Fig. 5.2, the LH mechanism

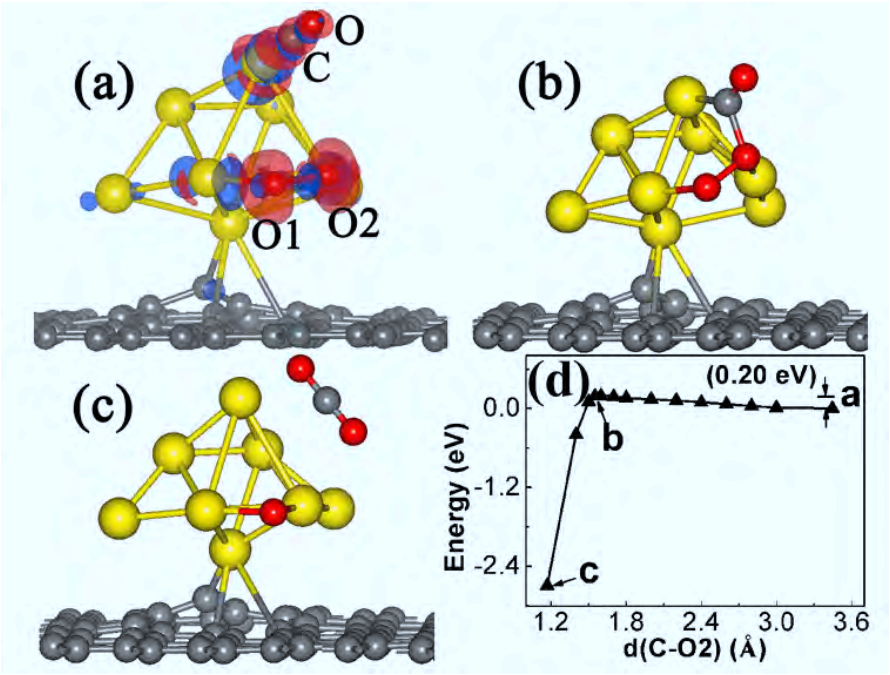


Figure 5.4: (a-c) LH type of CO oxidation catalyzed by the 3D isomer of $Au_8$ on the defective graphene. (a) The initial state of the reaction: d(O(1)-O(2))=1.42 Å, d(C-O(2))=3.45 Å. The isosurface of excess (red) and depleted (blue) electronic charge is also shown here. (b) The transitional state: d(C-O(2))=1.60 Å, d(O(1)-O(2))=1.46 Å. (c) The final state of forming $CO_2$. (d) The energy profile along the reaction coordinate d(C-O(2)).

of reaction catalyzed by the planar $Au_8$ cluster (P1) was shown. With the binding of $O_2$ molecule, the co-adsorption of CO molecule on the peripheral Au atom as shown in the figure yielded the adsorption energy around 1.2 eV. The atomic structures of the initial state, transition state, final state of the reaction, and the energy profile along the reaction coordinate are shown in Figs. 5.2(a-d), respectively. The reaction barrier was estimated to be 0.1 eV. The LH reaction catalyzed by the other planar structure of $Au_8$ (P2) was calculated to be 0.18 eV, and the atomic structures of different reaction states

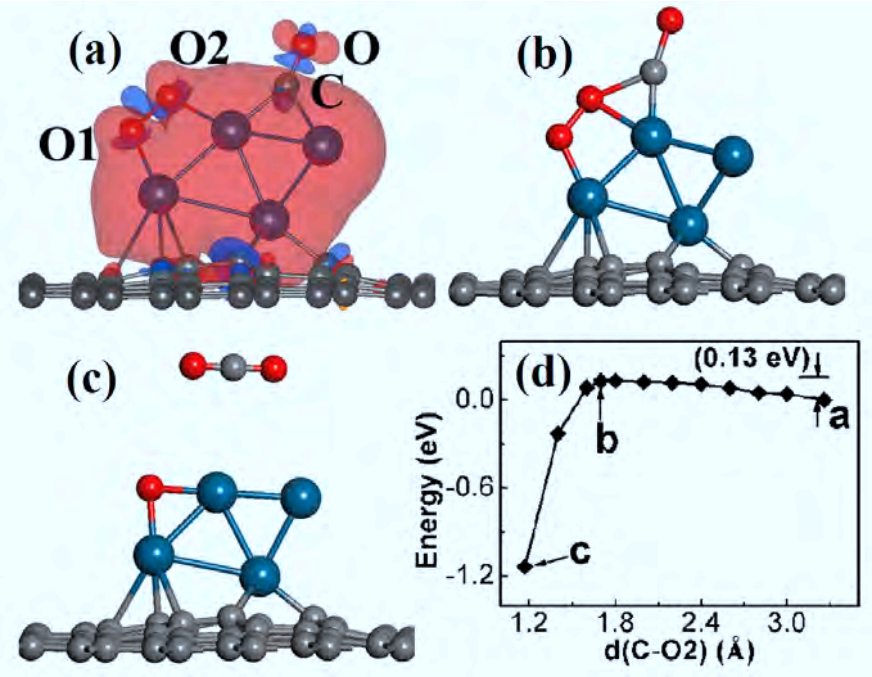


Figure 5.5: LH type of CO oxidation catalyzed by the $Pt_4$ on the defective graphene. (a) The initial state of the reaction: d(O(1)-O(2))=1.45 Å, d(C-O(2))=3.25 Å. The iso-surface of excess (red) and depleted (blue) electronic charge is also shown here. (b) The transitional state: d(C-O(2))=1.80 Å, d(O(1)-O(2))=1.47 Å. (c) The final state of forming $CO_2$. (d) The energy profile along the reaction coordinate d(C-O(2)).

with the energy profile along the reaction coordinate are shown in Figs. 5.3. The details of the LH reaction catalyzed by the 3D $Au_8$ clusters are shown in Fig. 5.4. In this case, the adsorption energy of the CO molecule after the binding of the $O_2$ is 1.1 eV, and the reaction barrier was calculated to be 0.2 eV. In Fig. 5.5, we showed the initial state, transition state, final state, and the energy profile of the LH reaction catalyzed by the $Pt_4$ cluster. In this case, the reaction barrier was estimated to be 0.13 eV. We also considered the ER mechanism of the CO oxidation catalyzed by $Au_8$ or $Pt_4$ clusters on defective graphene. Reaction barriers of ER type of CO oxidations were calculated to be

0.26 eV, 0.23 eV, 0.22 eV, and 0.16 eV, for P1-$Au_8$, P2-$Au_8$, 3D-$Au_8$, and $Pt_4$ clusters, respectively, indicating that CO oxidation can readily happen at room temperature.

### 5.2.3 Correlating with other kinds of defects in graphene

As discussed in the Introduction, defects in graphene can be diverse, ranging from zero-dimensional to one-dimensional and two-dimensional defects. Even for zero-dimensional vacancies in graphene, they can be missing of a single carbon atom, or missing of two, three and more carbon vacancies. One key question we may ask is whether these kinds of defects can have the similar effects as the single-carbon vacancy as we presented before. In this sense, recently, Wang et al.[195] used high-energy atom/ion bombardment to create defects, and vacancies including monovacancy, bivacancy and trivacancy have been clearly observed by using high-resolution transmission electron microscope (HRTEM). As shown in Fig. 5.5, the images of HRTEM (Figs. 5.5(a-c)) match very well with the atomic models (Figs. 5.5(d-f)) for different types of vacancies. Just like single-carbon-vacancy defect, vacancies with two or three carbon atom missing can also provide dangling bonds for the adsorption of metal clusters by forming strong carbon-metal covalent bonds. It is obvious that with more dangling bonds as in the case of multiple vacancies, transition metal clusters may be more strongly anchored through carbon 2p and metal d orbital bonding. Therefore, a high stability and catalytic activity of these supported metal nanoclusters can be expected.

In graphene, particularly in the presence of defects, carbon atoms can reconstruct themselves into other polygons during annealing, leading to a lower total energy.[181] For instance, graphene with bivacancy may reconstruct into a $V_2$(5-8-5) defect with two

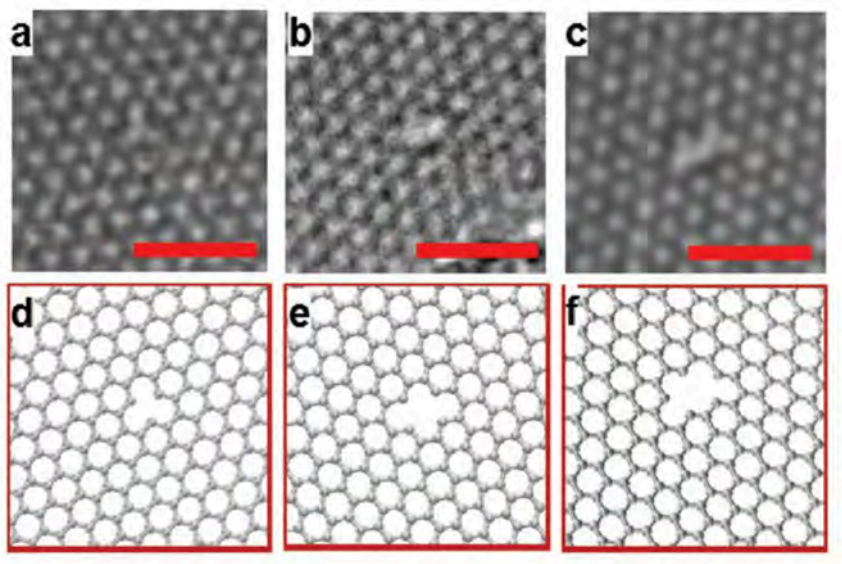


Figure 5.6: HRTEM images of (a) a monovacancy, (b) a bivacancy, and (c) a trivacancy. Scale bar: 1 nm. (d-f) are the atomic model for the three different vacancy types. Reprinted with permission from Ref.[195]

pentagons and one octagons, instead of four hexagons, and no dangling bond is present in this $V_2$(5-8-5) defect. Actually, bivacancy defect may also transform into an arrangement of three pentagons and three heptagons $V_2$(555-777), as well as $V_2$(5555-6-7777) defect. So how does these reconstructed defects affect the adsorption and catalytic of support metal clusters? Recently, Cretu et al.[182] used electron microscopy combined with DFT to show that there is a strain field around these reconstructed point defects (such as 555-777 defect). It was found that this strain field around the defects reaches far into the unperturbed hexagonal network (see Fig. 5.6) and adsorbed metal atoms or clusters have a high affinity to this nonperfect regions.[183] Moreover, metal atoms could be bonded on these reconstructed defects with energies of the order of 2 eV, and the interaction between these reconstructed defects and metal clusters was found to be

originated from an interplay of the strain in atomic network and electronic adsorption effects. As we have discussed in Chapter 4, strain has strong effect on the stabilization and catalytic properties of supported metal nanoclusters, so we conclude that these reconstructed defects without dangling bonds will also be beneficial for graphene-supported metal nanocatalysts.

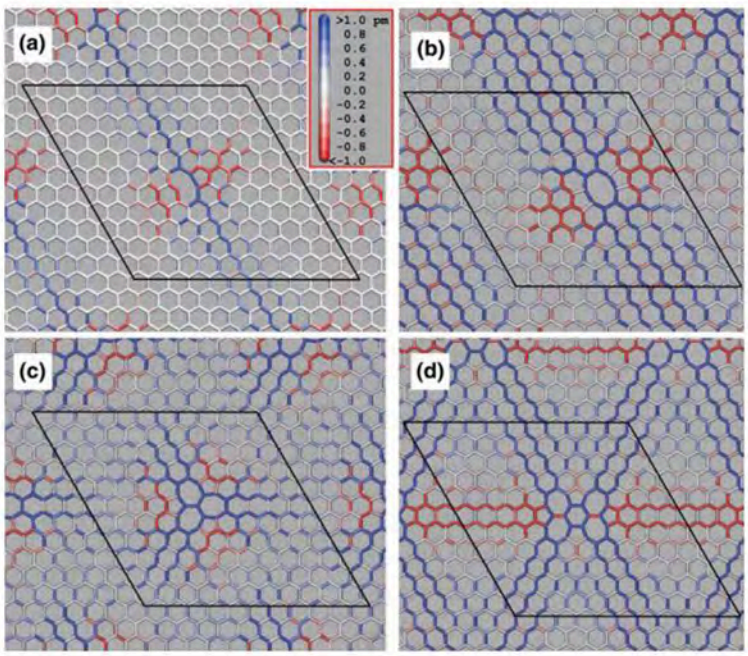


Figure 5.7: Atomic structures of a reconstructed single vacancy (a), bivacancy with 5-8-5 reconstruction (b), 555-777 reconstruction (c) and 5555-6-7777 reconstruction. The bonds are colored according to an increase (blue) or decrease (red) in the bond length (in picometers). It is evident that the strain fields exist for at least 2 nm away from the defect. Reprinted with permission from Ref.[183]

Other defects such as topological line defects, grain boundaries or stacking faults, were also studied in literature. For instance, one dimensional extended line defect in graphene was found to be a metallic wire,[184] and on this metallic wire, metal atoms were found

to have strong hybridization between d orbitals of metal atoms and $p_z$ orbital of carbon, resulting in an enhanced adsorption energy and charge transfer.[185] Grain boundaries with different dangling bond density were found to have interesting chemical reactivity compared to pristine graphene,[186, 187] suggesting that metal clusters can also interact strongly with these defects.

These results show that our discussion based on single-carbon vacancy can be extended to different kinds of defects, which are also expected to have strong influence on stability and catalytic activity of supported metal nanocatalysis.

## 5.3 Chapter summary

In summary, we present in this chapter a detailed study on the effect of defects in graphene on the catalytic performance of supported metal nanoclusters by first principles calculations based on DFT. Compared to the case of pristine graphene, the simplest single-carbon-vacancy defect in graphene was found to enhance the adsorption and stabilization of supported $Au_8$ and $Pt_4$ clusters. Specifically, the adsorption energies increase from 0.71 eV, 0.65 eV and 0.52 eV (on pristine graphene) to 1.56 eV, 1.52 eV and 1.51 eV for $Au_8$ P1, P2 and 3D insomers. For $Pt_4$ cluster, the significant electronic structure change of the system initiated by the carbon vacancy leads to a high adsorption energy of 7.7 eV. The anchoring of those clusters were found to be the defect-induced hybridization of carbon 2p and Au/Pt 5d orbitals around the defect region.

Results also show that on pristine graphene, supported three isomers of $Au_8$ under study are inactive for CO oxidation, and $Pt_4$ cluster have a relatively high barrier for this

reaction. On graphene with a single carbon vacancy, all these metal clusters were found to have a lower barrier ($\sim$ 0.2 eV) for CO oxidation. The origin of this lower barrier reaction is due to the defect-induced charge transfer to the antibonding $2\pi$* orbital of $O_2$ molecule from metal cluster for the case of $Au_8$ and from the metal cluster and the interfacial region for the case of $Pt_4$, leading to an activation of O-O bond in $O_2$ molecule.

Conclusions on the stability and catalytic activity of supported metal clusters drawn from the study of a single carbon vacancy may be extended to other types of defects, such as multiple carbon vacancies, Stone-Wales type reconstructed defects, topological line and grain boundary defects. In addition, based on the results of the previous chapter, local strain created by the defect may also be beneficial to catalysis. Experimentally, because defects are inevitable in the synthesis and preparation of graphene sheets, results presented in this work may be useful in explaining recent experiments, and helpful for the future design of graphene-supported metal nanocatalysts.

# Chapter 6

# Metal-embedded graphene: A possible single-atom nanocatalyst

## 6.1 Introduction

In supported metal catalysts, metals are finely dispersed on a support with a high surface area for the maximum exposure of catalytic active components. The size of metal particles is therefore one of the most important factors that decide the performance of a catalyst. Recent experimental and theoretical work showed that subnanometer clusters, which include just a few atoms, have better catalytic activity and/or selectivity that larger metal nanoparticles.[43, 156, 196] As catalytic active sites usually constitute just low-coordination, unsaturated atoms, downsizing the metal particles to single atoms is highly desirable for practical applications. However, this is hampered for two

reasons. First, the fabrication of such single-atom catalyst is a significant challenge because single atoms are typically unstable, as they are too mobile and easy to sinter under operational reaction conditions. Also, it remains unclear whether such single atoms are catalytical active or have better performance than their cluster counterpart because of the non-scalable physical/chemical properties at this nanoscaled region.

Recently, single-metal-atom-embedded graphene structures have been fabricated, and different elements (Au, Pt, Co, and In) have been successfully doped in the single-atom form in graphene.[46, 195] Therefore, the diffusion of single metal atoms in the graphene plane can be controlled. Substitution of single metal atom in monolayer graphene can be achieved by a two-step process: create vacancies by high energy atom/ion bombardment, and then fill these vacancies with desired metal dopants.[195] These metal-embedded graphene structures are very stable and have been clearly observed by an aberration-corrected and monochromated transmission electron microscope (TEM).[195] In this context, Krasheninnikov et al.[197] investigated different transition-metal-atom-embedded graphene structures by using density functional theory and they found that the electronic and magnetic properties of these systems are determined by the strong bonding (binding energy up to 7 eV) between single transition metal atom and the neighboring carbon atoms. Therefore, the chemically inert graphene may be transformed to a very active catalyst with single-atom catalytic active site through the interaction of the metal atom and the carbon vacancy.

In this chapter, we present a systematic investigation on geometrical and electronic structures of graphene embedded by various transition metal elements, including Sc, Ti, V, Cr, Mn, Fe, Co, Ni, Cu, Zn, Ag, Pt, Au, and the adsorption of small gas molecules ($O_2$, CO, $NO_2$ and $NH_3$) on these metal-embedded graphene. The adsorption structures,

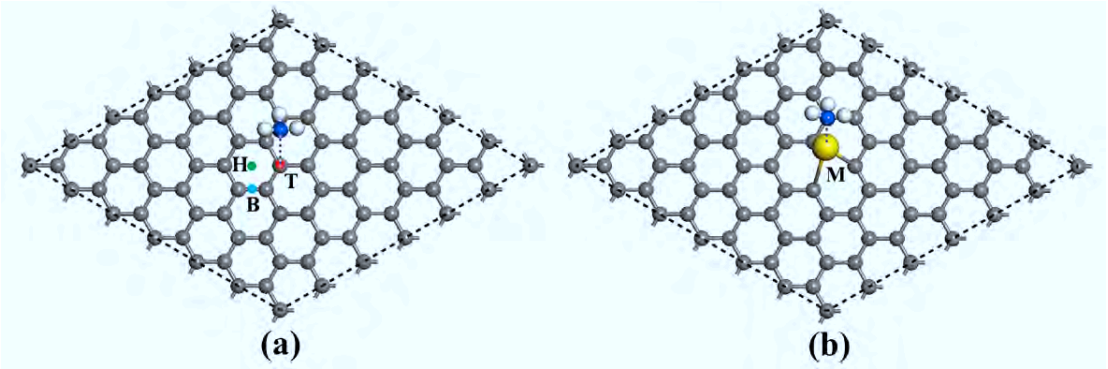


Figure 6.1: Schematic view of a single gas molecule ($NH_3$) adsorption on pristine graphene (a) and TM-graphene (b). T: top site, B: bridge site, H: hollow site, M: transition metal atom (Au). Carbon atom in grey, H in white, N in blue and Au atom in yellow.

adsorption energies, charge transfer and magnetic properties of the adsorbed systems were extensively explored. Our calculations explicitly suggest that among all transition metals under study, Ti and Au are best choices for the applications of oxidation catalysis. By using Au-embedded graphene as a model system, we studied its catalytic activity towards CO oxidation. Our calculations suggest that Au-embedded graphene is an excellent candidate for single-atom heterogeneous catalyst, which has a great potential to reduce the high cost of commercial noble-metal catalysts in industry. Detailed analysis of the electronic structures and magnetic properties of these metal-embedded graphene systems may also be useful for future design of graphene-based gas sensors and spintronic devices.

In Fig. 6.1, we show schematic views of a gas molecule adsorbed on the pristine graphene and a molecule on the transition-metal-embedded graphene (TM-graphene).

For the case of pristine graphene, three possible adsorption sites were considered: hollow site (H) at the center of a carbon hexagon, bridge site (B) in the middle of C-C bond, and top site (T) on the top of a carbon atom (Fig. 6.1(a)). For TM-graphene, the molecule is initially placed on top of the metal atom which substitutes a carbon (Fig. 6.1(b)). Different molecular orientations were considered and calculated to find the most stable adsorption configuration that has the lowest total energy and the highest adsorption energy. The adsorption energy, $E_{ad}$, is defined as

$$E_{ad} = E_{molecule} + E_{graphene} - E_{molecule@graphene} \tag{6.1}$$

where $E_{molecule}$, $\boldsymbol{E}_{graphene}$, and $E_{molecule@graphene}$ denote the energies of the isolated gas molecule, graphene (or TM-graphene) substrate, and the combined molecule-graphene system, respectively.

For the structural optimization and electronic structure calculations, the first principles method based on DFT was employed via the computational package VASP,[108] with the exchange and correlation energy included through a generalized gradient approximation in PBE format[124]. Projected augmented-wave potentials[98] are employed to describe the ion-electron interaction. A plane-wave basis set with a cut-off energy of 400 eV and Γ-point sampling of the Brillouin zone is used in structure optimization. The mesh of K space is increased to $6\times6\times1$ to obtain accurate energies, electronic structures, and magnetic properties. A supercell that includes 6x6 unit cells of graphene in graphene plane, and a vacuum region of 20 Å in the direction normal to graphene plane (Z direction) was adopted. In optimizing atomic structures, the force convergence criterion was set to 0.02 eV/Å. The calculation of reaction barriers towards CO oxidation

was done with $DMol_3$ package,[198, 199] with DFT semicore pseudopotentials (DSPPs) and a double numerical basis set. The minimum-energy pathway for elementary steps was computed using the nudged elastic band method.[106]

## 6.2 Results and discussion

### 6.2.1 Metal-embedded graphene: Structures and properties

As a preliminary test, we optimized the atomic geometries of these small gas molecules within a $16\times17\times18$ $Å^3$ box by using aforementioned DFT method. Our calculations produced the bond lengths, 1.144 Å, 1.234 Å, 1.214 Å, and 1.024 Å, for CO, $O_2$, $NO_2$, and $NH_3$ molecules, respectively. The bond angles of $NO_2$, and $NH_3$, denoted by Φ(O-N-O) and Φ(H-N-H), were estimated to be 133.7° and 106.3°, respectively. All these results are in good agreement with previously published results.[200–202]

Before we study the adsorption of gas molecules, it is helpful to look at first the physical properties of metal-embedded graphene itself. Figure 6.2(a) shows the optimized configuration of graphene embedded with a typical transition metal, Au. The optimized structures for graphene embedded with other metal elements have similar structures. As the metal atom is much larger than carbon, the metal atom extrudes outwards from the graphene surface. The height, d, defined as the distance between the Au atom and the graphene plane, is calculated to be 1.87 Å, with the Au-C bond length 2.07 Å, in

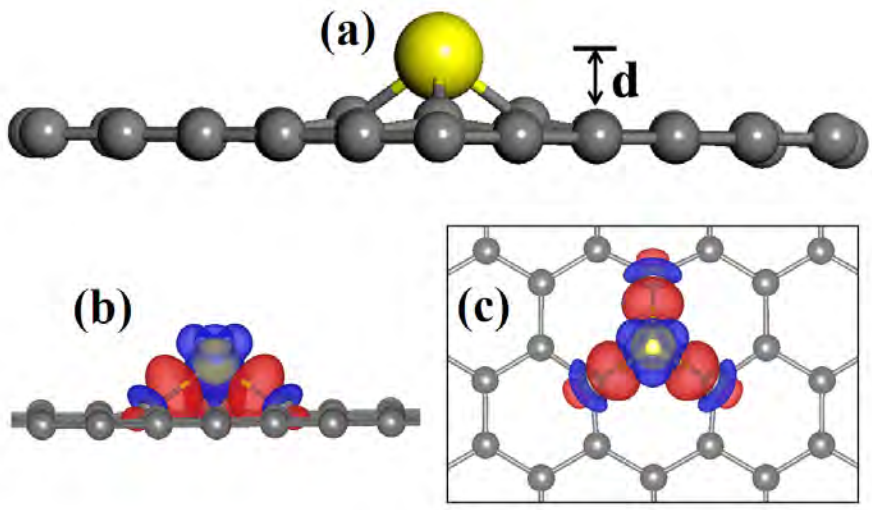


Figure 6.2: (a) Optimized structures for a typical transition metal (Au) embedded graphene, with d the height of TM atom above graphene base plane. (b) and (c) show the side view and top view of charge redistribution plot for Au-embedded graphene. Charge accumulation in red and depletion in blue.

good agreement with previous simulations.[197] It is found that the charge redistribution mainly happens around the Au-C bonds as expected, as shown in the charge redistribution plot in Figs. 6.2(b) and (c), indicating the formation of strong covalent bonds. Here, the charge redistribution, $\triangle\rho$, is defined as

$$\triangle\rho = \rho_{TM-graphene} - (\rho_{TM} + \rho_{graphene}) \tag{6.2}$$

where $\rho_{TM-graphene}$, $\rho_{TM}$, $\rho_{graphene}$ represent the charge densities of the TM-graphene system, the isolated metal atom, and the graphene sheet, respectively. Our calculations show that in this system, Au is positively charged.

In Fig. 6.3, we show the total and local density of states (DOS) for Cu, Ag and Au

embedded graphene. For all cases, the symmetry between spin-up and spin-down channels are broken (see Figs 6.3(a-c)), leading to a magnetic moment of 1.14 $\mu$B, 1.12 $\mu$B, and 1.00 $\mu$B per unit cell for Cu, Ag, Au embedded graphene respectively. As we can see from Figs 6.3(d-f), magnetic moments originate from the depletion of spin-down electrons of both d orbital of the metal atom and p orbital of neighboring carbon atoms. As a result, the high density of spin-polarized states is localized around the Fermi level. These localized states are important to gas molecule adsorption and activate reactants to lower the reaction barrier, as we shall discuss later.

### 6.2.2 Metal-embedded graphene towards small gas molecule adsorption

In this section, we will examine the adsorption of small gas molecules on both pristine and metal embedded graphene. In Fig. 6.4, we show the most stable adsorption configurations of $O_2$, CO, $NO_2$ and $NH_3$ on pristine (Figs. 6.4(a), (c), (e), (g)) and Au-embedded graphene (Figs. 6.4(b), (d), (f), (h)), respectively. Note that the most stable configurations presented here were determined by choosing the lowest-energy one among various adsorption sites and molecular orientations. It is found that on pristine graphene, molecules interact rather weak with the substrate in general, and on metal-embedded graphene, all gas molecules form strong bonds with the embedded atom, with a much shorter adsorption lengths. In following sections, we present in detail the geometrical and electronic properties of the adsorption of these gas molecules in the order of $O_2$, CO, $NO_2$ and $NH_3$.

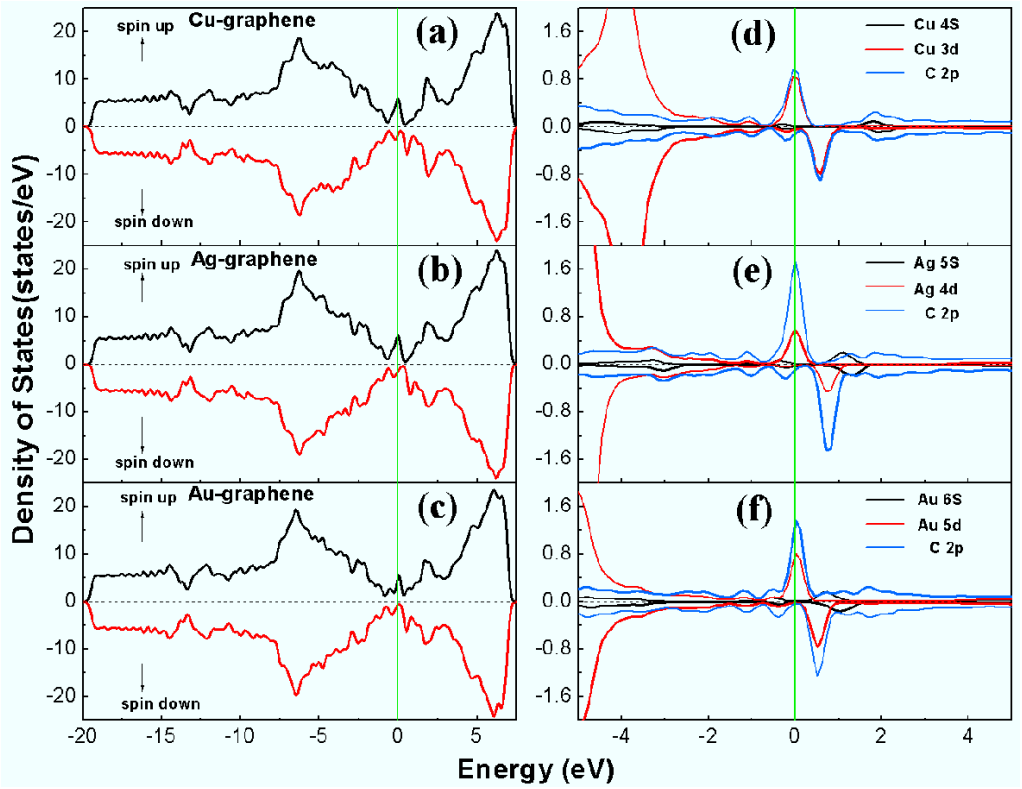


Figure 6.3: (a-c) Spin-polarized total density of states for Cu, Ag and Au embedded grahene. (d-f) Partial density of states projected on s (black curve), d(red curve) orbital of metal atoms and 2p (blue curve) of neighboring carbon atoms for the three cases. Fermi energy is set to zero.

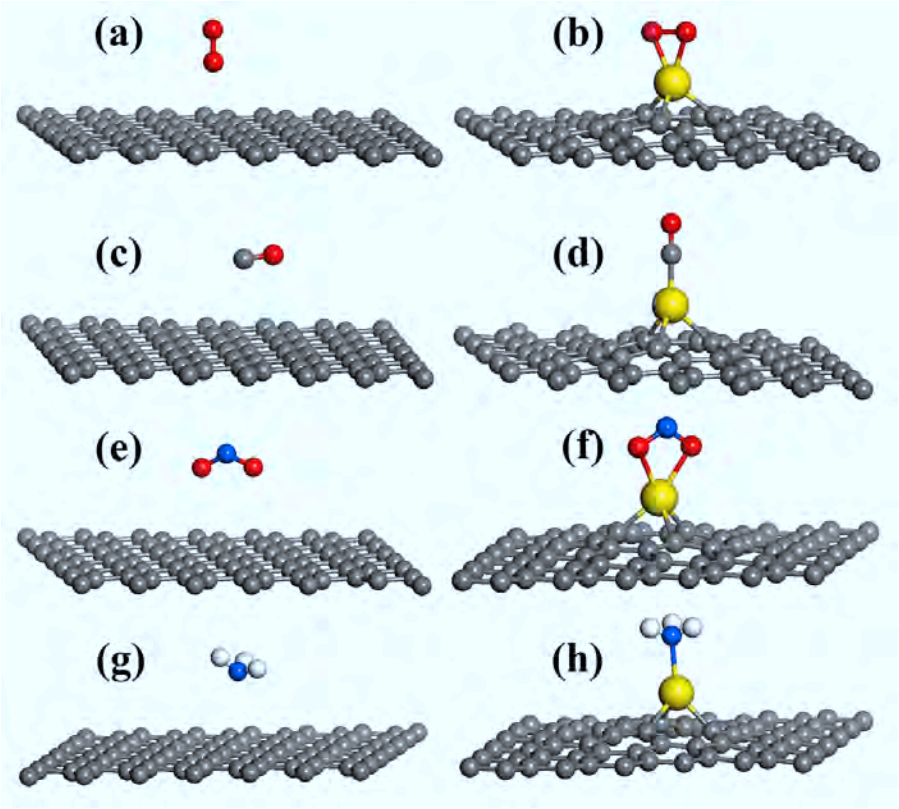


Figure 6.4: Optimized configurations for $O_2$, CO, $NO_2$ and $NH_3$ adsorbed on pristine graphene (left side: (a), (c), (e), (g) and TM-graphene (right side: (b), (d), (f), (h)).Note that various configurations have been considered and we only present here the most stable configurations. Carbon atom in grey, H in white, N in blue, O in red and Au atom in yellow.

**$O_2$ adsorption**

On pristine graphene, $O_2$ is adsorbed on the hollow (H) site with O-O bond perpendicular to the graphene surface, as shown in Fig. 4(a). The adsorption energy is calculated to be less than 0.1 eV. After adsorption, O-O bond length remains almost the same as

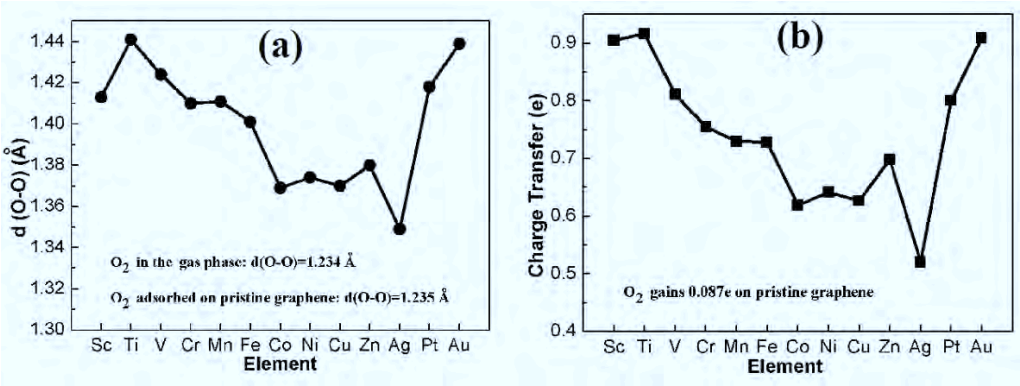


Figure 6.5: (a) $O_2$ bond length d(O-O) after adsorption on various TM-embedded graphene. Note that $O_2$ in the gas phase d(O-O)=1.234 Å, adsorbed on pristine graphene d(O-O)=1.235 Å. (b) Charge transfer from TM-graphene to $O_2$. There is an excess of $0.087e$ for $O_2$ adsorbed on pristine graphene, making $O_2$ acceptor-like.

in the gas phase (1.24 Å), and the adsorption length of $O_2$ on pristine graphene (defined as the shortest molecule-substrate distance) is estimated to be 3.7 Å. The Bader charge population analysis[132] shows that less than $0.1e$ was transferred from the pristine graphene to $O_2$ molecule, indicating a weak physisorption. On metal-embedded graphene, in all cases, $O_2$ molecule is adsorbed with O-O bond lying nearly parallel to the graphene plane (see Fig. 6.4(b)), with greatly increased adsorption energies above 1 eV, and significantly decreased adsorption lengths around 2 Å.

In Fig. 6.5, we show the O-O bond length, d(O-O), and charge transfer for $O_2$ adsorbed on 13 different TM-graphene. Generally, there is a large expansion of O-O bond as shown in Fig. 6.5(a). Judging from this figure, Ti and Au embedded graphene are two most reactive ones in terms of $O_2$ adsorption among all TM-graphene, for both of which the O-O bond of $O_2$ molecule is enlarged to above 1.44 Å, increased over 0.2 Å compared to that of $O_2$ in the gas phase. The charge transfer between TM-graphene and

Table 6.1: $O_2$ adsorption on pristine and Cu, Ag, Cu embedded graphene: the adsorption length ($d$), adsorption energy ($E_{ad}$), bond length of $O_2$ after adsorption (d(O1-O2)), charge transfer from the substrate to $O_2$ ($\Delta$Q) and magnetic moment of the total system (M).

| Configuration | $d$(Å) | $E_{ad}$(eV) | $d$(O1-O2)(Å) | $\triangle Q(e)$ | $M(\mu$B) |
|---|---|---|---|---|---|
| $O_2$ on graphene | 3.65 | 0.031 | 1.235 | 0.087 | 2.00 |
| $O_2$ on Cu-graphene | 1.92 | 1.59 | 1.37 | 0.63 | 0.83 |
| $O_2$ on Ag-graphene | 2.15 | 1.25 | 1.35 | 0.51 | 0.94 |
| $O_2$ on Au-graphene | 2.07 | 1.52 | 1.44 | 0.91 | 0.45 |

$O_2$ (as shown in Fig. 6.5(b)) shows a similar trend. It can be seen from Fig. 6.5(b) that more than $0.9e$ transferred from the Ti or Au-graphene to the adsorbed $O_2$ molecule, causing the significant elongation of d(O-O) in these two cases. The great enlargement of d(O-O) indicates significant weakening of the O-O bond, and is highly desirable for chemical reactions such as CO oxidation or oxygen reduction reactions, for which the breaking or weakening of $O_2$ bond is often regarded as the rate-limiting step.[21, 73, 203] On the other hand, Ag-embedded graphene shows the least reactivity for $O_2$ adsorption, with O-O bond length around 1.35 Å and $0.5e$ charge transfer, while metals such as Cu show reactivity in between. Apart from the characteristics of chemisorption, the magnetic moment of TM-graphene system is also varied upon $O_2$ adsorption. In Table 6.1, we listed in detail calculated results of adsorption length, O-O bond length, adsorption energy, charge transfer, and the magnetic moments of $O_2$ adsorbed on Cu, Ag and Au embedded graphene.

To further understand the bond expansion of $O_2$ on TM-graphene, we plot the partial

density of states (PDOS) of the $O_2$ molecule adsorption on Cu, Ag, Au mebedded graphene, in Fig. 6.6(a), (b) and (c), respectively. For $O_2$ molecule in the gas phase, the LUMO is the spin-down antibonding $2\pi$* orbital. Upon adsorption, electrons populated to initially empty spin-down antibonding $2\pi$*, leading to enlarged O-O bond length. Comparing this figure to Table 6.1, we can see the trend that the more electrons populated to the antibonding $2\pi$* orbital (higher filling rate of the PDOS peak), the more the O-O bond will be expanded. The charge redistribution plot in Fig. 6(d) clearly shows that electrons populated to the anti-bonding $2\pi$* orbital of the $O_2$ molecule are mainly from the metal atom, suggesting the strong effects of the embedded metal atom on chemical reactivity of graphene.

**CO adsorption**

For CO, $NO_2$ and $NH_3$ molecules, we only study their adsorption on Cu, Ag and Au embedded graphene, as these three elements represent typical 3d, 4d and 5d transition metals, respectively. The most stable adsorption site for CO on pristine graphene is at the hollow (H) site, with the CO lying nearly parallel to the graphene surface. The adsorption energy is estimated to be 0.017 eV, and the molecule-substrate distance is found to be about 3.6 Å (physisorption). On TM-graphene, CO is adsorbed with C atom bonded to metal atom in the substrate. Our calculations show that there is a large increase of adsorption energy (to around 2 eV) and charge transfer ($> 0.1e$), with a significant decrease of molecule-substrate distance to around 2 Å.(see Table 6.2) Surprisingly, upon adsorption of nonmagnetic CO molecule, the magnetic moment of TM-embedded graphene is enhanced from 1 $\mu$B (without adsorption) to about 3 $\mu$B.

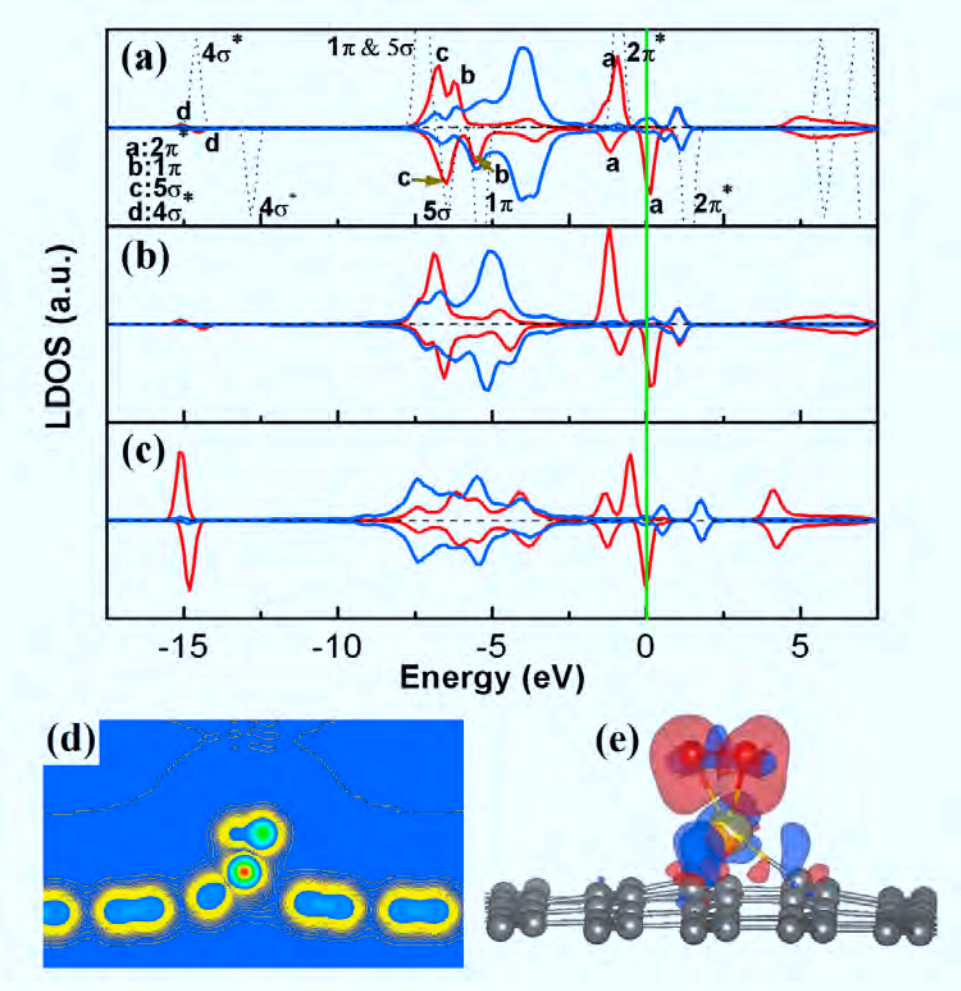


Figure 6.6: (a-c) PDOS for $O_2$ adsorption on Cu, Ag, Au embedded graphene. Black dotted curve: $O_2$ in the gas phase; red curve: $O_2$ in the adsorbed state. Blue curve: d-projected PDOS for Cu, Ag, Au atom respectively. Fermi energy is set to zero. (d) and (e) show the charge density and 3-dimensional density difference plots for $O_2$ adsorption on Au-graphene. Charge accumulation in red and depletion in blue.

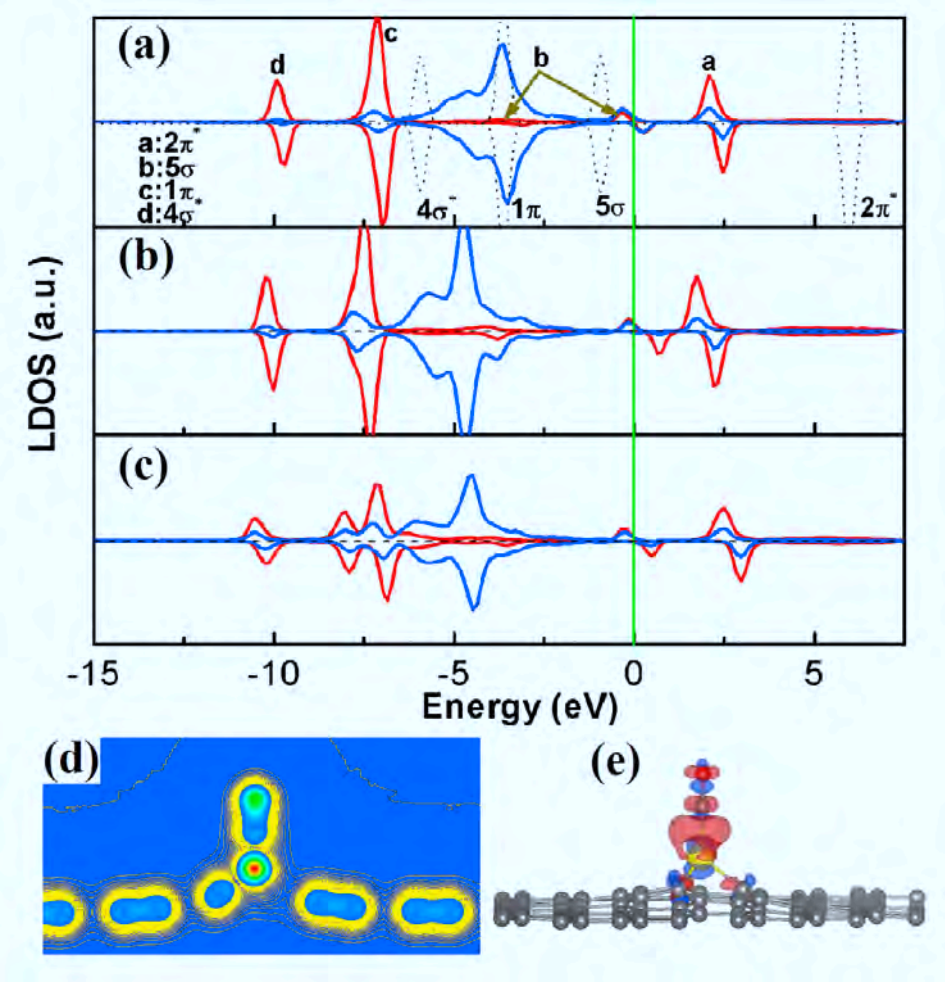


Figure 6.7: (a-c) PDOS for CO adsorption on Cu, Ag, Au embedded graphene. Black dotted curve: CO in the gas phase; red curve: CO in the adsorbed state. Blue curve: d-projected PDOS for Cu, Ag, Au atom respectively. Fermi energy is set to zero. (d) and (e) show the charge density and density difference plots for CO adsorption on Au-graphene. Color scheme is the same as in Fig. 6.6.

Table 6.2: CO adsorption on pristine and Cu, Ag, Cu embedded graphene: the adsorption length ($d$), adsorption energy ($E_{ad}$), bond length of C-O after adsorption (d(C-O)), charge transfer from the substrate to CO ($\Delta$Q) and magnetic moment of the total system (M).

| Configuration | $d$(Å) | $E_{ad}$(eV) | $d$(C-O)(Å) | $\triangle Q(e)$ | $M(\mu$B) |
|---|---|---|---|---|---|
| CO on graphene | 3.60 | 0.017 | 1.144 | -0.001 | 0 |
| CO on Cu-graphene | 1.83 | 1.30 | 1.161 | 0.129 | 2.89 |
| CO on Ag-graphene | 2.01 | 1.01 | 1.157 | 0.151 | 2.94 |
| CO on Au-graphene | 1.98 | 1.37 | 1.166 | 0.140 | 3.00 |

To understand the enhanced adsorption of CO, we plot the PDOS of CO molecule and the charge redistribution for CO adsorbed on Cu, Ag, Ag embedded graphene in Fig. 6.7. As it shows, upon adsorption, the occupied $5\sigma$ orbital (HOMO) of the CO is broadened, shifted far below Fermi level, and strongly hybridize with localized d-orbital of TM atom. The empty antibonding orbital 2 $\pi$* (LUMO) of the CO in the gas phase is also pulled closer to the Fermi level and partially occupied due to the back-donation of d electrons, resulting in slightly increase in the C-O bond length. This can also be seen from the charge density and charge redistribution plots, as shown in Figs. 6.7(d) and(e). The imbalance of spin-up and spin-down electrons of CO molecule at the Fermi level results in an enhancement of magnetic moment.

**$NO_2$ adsorption**

The adsorption of triangular-shaped $NO_2$ molecule is a little bit more complicated than $O_2$ or CO. Three molecular orientations were initially considered, i.e. binding of $NO_2$

Table 6.3: $NO_2$ adsorption on pristine and Cu, Ag, Cu embedded graphene: the adsorption length ($d$), adsorption energy ($E_{ad}$), bond length of $NO_2$ ($d$(N-O)) and bond angle ($\Phi$(O-N-O)), charge transfer from the substrate to $NO_2$ ($\Delta$Q) and magnetic moment of the total system (M).

| Configuration | $d$(Å) | $E_{ad}$(eV) | $d$(N-O)(Å) | $\Phi$(O-N-O)(deg) | $\triangle Q(e)$ | $M(\mu$B) |
|---|---|---|---|---|---|---|
| $NO_2$ on graphene | 3.89 | 0.182 | 1.214 | 133.7 | 0.182 | 0.88 |
| $NO_2$ on Cu-graphene | 2.06 | 2.12 | 1.284 | 110.6 | 0.639 | 1.94 |
| $NO_2$ on Ag-graphene | 2.27 | 2.01 | 1.279 | 112.8 | 0.619 | 0.23 |
| $NO_2$ on Au-graphene | 2.24 | 2.29 | 1.283 | 111.5 | 0.565 | 0.04 |

via a nitrogen atom (nitro configuration), via an oxygen atom (nitrite configuration) and via both oxygen atoms (cycloaddition configuration). On pristine graphene, it is found that $NO_2$ is bound by cycloaddition configuration on the bridge site (see Fig. 6.4(e)), with a moderate adsorption energy of 0.18 eV and an acceptor-like feature ($NO_2$ gains about 0.2$e$), in agreement with Ref [204]. On TM-graphene, the cyloaddition configuration is again preferred, with an adsorption energy about 2 eV, as shown in Fig. 6.4(f), followed by nitro configuration with a weaker adsorption about 1.8 eV (the configurations are not shown here). The preferred adsorption configuration can be readily understood as the cycloaddition geometry favors the interaction between the electron-rich oxygen atoms and the carbon atoms in pristine graphene or TM atoms in metal-embedded graphene.

In Table 6.3, we show the detailed results for structure, adsorption energy, charge transfer and magnetic moment of $NO_2$ adsorption on Cu, Ag and Au embedded graphene.

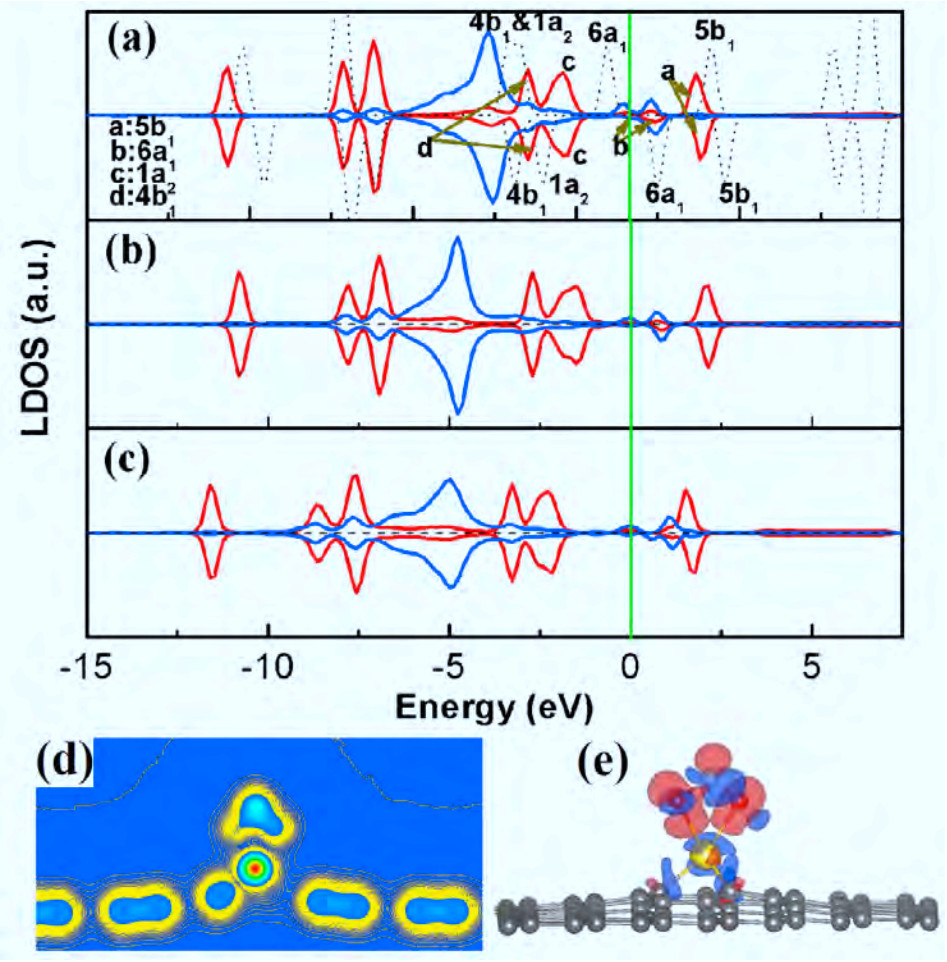


Figure 6.8: (a-c) PDOS for $NO_2$ adsorption on Cu, Ag, Au embedded graphene. Black dotted curve: $NO_2$ in the gas phase; red curve: $NO_2$ in the adsorbed state. Blue curve: d-projected PDOS for Cu, Ag, Au atom respectively. Fermi energy is set to zero. (d) and (e) show the charge density and density difference plots for $NO_2$ adsorption on Au-graphene. Color scheme is the same as in Fig. 6.6.

Compared to the case of pristine graphene, we can see that upon adsorption on TM-graphene, the bond length $d$(N-O) and bond angle $\Phi$(O-N-O) of $NO_2$ changes significantly due to the large charge transfer from substrate to the molecule ($\sim 0.6e$). Figure 6.8 shows the electronic structures: both spin-up $6a_1$ component (HOMO) and spin-down $6a_1$ component (LUMO) are shifted closer to the Fermi level due to the interaction of the molecular orbital and d-orbital of TM atoms. The filling of LUMO ($6a_1$,$\downarrow$) induces an increase of the N-O bond length, which is also demonstrated in charge transfer plot in Fig. 6.8(e). Besides the activation of $NO_2$ molecule, the magnetic properties of TM-graphene system also changes significantly. The magnetic moment of $NO_2$ adsorption on Cu-graphene is calculated to be about 2 $\mu$B; for Ag or Au-graphene, the magnetic mement decreases drastically and nearly diminishes (0.23 $\mu$B, 0.04 $\mu$B), indicating that the magnetic properties of TM-graphene can be efficiently tuned by $NO_2$ adsorption.

**$NH_3$ adsorption**

The lowest-energy configurations for $NH_3$ adsorption on pristine and TM-graphene are shown in Fig. 6.4(g) and (h), respectively. On TM-graphene, $NH_3$ is bound by the nitrogen atom and the underlying metal atom, which is consistent with the generally accepted idea that the chemical bonding in $NH_3$/metal system can be related to the occupied nitrogen lone-pair orbital interacting with the metal valence bands.[206] Compared with CO, $O_2$ and $NO_2$, the atomic structure of $NH_3$, such as the N-H bond length $d$(N-H) and bond angle $\Phi$(H-N-H), is nearly unchanged after adsorption and the adsorption energies are moderate on TM-graphene (see Table 6.4), implying that the desorption of $NH_3$ from NM-graphene can be readily achieved by annealing or short UV irradiation,[205] which is an essential quality for efficient gas sensors.

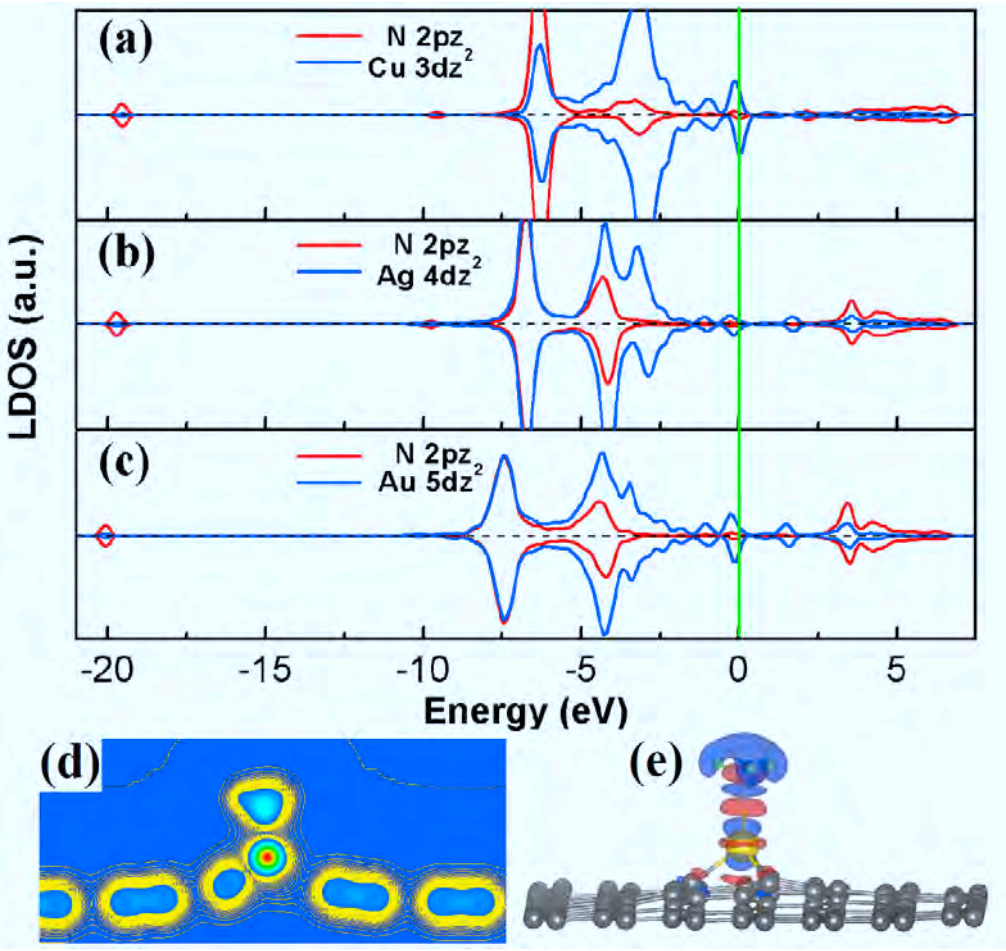


Figure 6.9: (a-c) PDOS for $NH_3$ adsorption on Cu, Ag, Au embedded graphene. The $d_z{}^2$ (blue curve) orbital of TM atoms together with the N $2p_z$ orbital (red curve), lead to a strong hybridization. Fermi energy is set to zero. (d) and (e) show the charge density and density difference plots for $NH_3$ adsorption on Au-graphene. Color scheme is the same as in Fig. 6.6.

Table 6.4: $NH_3$ adsorption on pristine and Cu, Ag, Cu embedded graphene: the adsorption length ($d$), adsorption energy ($E_{ad}$), bond length of $NH_3$ ($d$(N-H)) and bond angle ($\Phi$(H-N-H)), charge transfer from the substrate to $NH_3$ ($\Delta$Q) and magnetic moment of the total system (M).

| Configuration | $d$(Å) | $E_{ad}$(eV) | $d$(N-H)(Å) | $\Phi$(H-N-H)(deg) | $\triangle Q(e)$ | $M(\mu$B) |
|---|---|---|---|---|---|---|
| $NH_3$ on graphene | 3.66 | 0.029 | 1.024 | 106.3 | -0.008 | 0 |
| $NH_3$ on Cu-graphene | 2.07 | 1.03 | 1.024 | 107.4 | 0.646 | 1.03 |
| $NH_3$ on Ag-graphene | 2.26 | 0.94 | 1.024 | 107.4 | 0.568 | 1.00 |
| $NH_3$ on Au-graphene | 2.26 | 0.79 | 1.024 | 107.8 | 0.562 | 1.00 |

Next we discuss the electronic properties and adsorption mechanism for $NH_3$ on TM-graphene. The Schönfies notation for the occupied molecular orbitals of free $NH_3$ is $(1a_1)(2a_1)(1e_1)(3a_1)$. The $3a_1$ orbital has little hydrogen character and is known as nitrogen $2p_z$ lone-pair orbital of ammonia. So here the orbital of interest is in fact the N $2p_z$ orbital. By carefully examining components of TM metal d orbital, it is found that the hybridization mainly happens between N $2p_z$ and Metal $d_z{}^2$. As shown in Figs. 6.9(a-c), there is a strong hybridization between N $p_z$ state and metal $d_z{}^2$ state. A double peak structure of the density of states can clearly be identified, which indicates that the interaction of ammonia lone-pair orbital with the $d_z{}^2$ orbital of TM atoms lead to local bonding and antibonding states. The charge density and density redistribution plots (Figs. 6.9(d-e)) clearly show that electrons are transferred from metal-graphene interfacial region to N-metal bond, resulting in enhanced adsorption. This bonding mechanism suggests that by embedding graphene with appropriate metal atoms, it may have improved sensing ability for $NH_3$, compared to pristine graphene.

### 6.2.3 Au-embedded graphene towards CO oxidation

In light of the enhanced reactivity of graphene embedded with metal atoms, particularly Ti- and Au-embedded graphene towards $O_2$ activation, we studied the chemical reaction of CO oxidation catalyzed by Au-embedded graphene. It is found that Langmuir-Hinshelwood mechanism is more energetically favorable in reaction barrier than Eley-Rideal mechanism. We considered the LH reaction $CO + O_2 \rightarrow OOCO \rightarrow CO_2 + O$ as a starting point, followed by ER type of reaction $CO + O \rightarrow CO_2$. To search for the minimum energy pathway for the CO oxidation, we considered the most stable coadsorption configuration, in which the adsorbed CO molecule is tilted to the graphene plane while $O_2$ is parallel to the plane as initial state. The final state consists of a $CO_2$ molecule physisorbed on Au-graphene system with a chemisorbed atomic O atom on the catalyst. A total of 30 image structures were inserted between the IS and FS, and the calculated MEP profile is showed in Fig. 6.10. The energies are schematically plotted with respect to the reference energy, defined as the sum of the energies of individual Au-embedded graphene and CO, $O_2$ molecule in the gas phase.

The optimized structures for CO oxidation on Au-graphhene at each state along the MEP are displayed in Fig. 6.11. Once CO and $O_2$ are coadsorbed on Au-graphene system, one of the oxygen atoms (O1) in the $O_2$ molecule starts to approach the carbon atom of CO to reach the transition state. The O-O bond length of adsorbed $O_2$ molecule (d(O1-O2)) is elongated to 1.45 Å, while the distance between Au atom and carbon atom of CO decreases about 0.1 Å in an endothermic process.(see Table 6.5) The activation barrier for this step os extimated to be 0.31 eV, and a peroxo-type O2-O1-C-O complex is form over Au atom. Passing over TS, the peroxo-type complex is maitained until a metastable

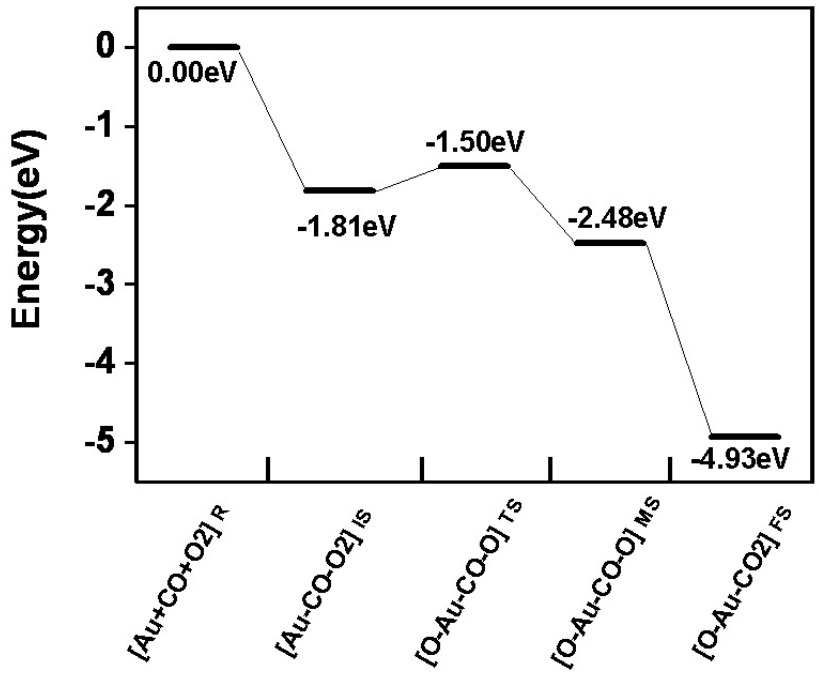


Figure 6.10: Schematic energy profile corresponding to local configurations show in Fig. 11 along the MEP via CO + $O_2$ $\rightarrow$ OOCO $\rightarrow$ $CO_2$ + O route. The energies are given with respect to the reference energy, defined as the sum of the energies of individual Au-embedded graphene and CO, $O_2$ molecule in the gas phase.

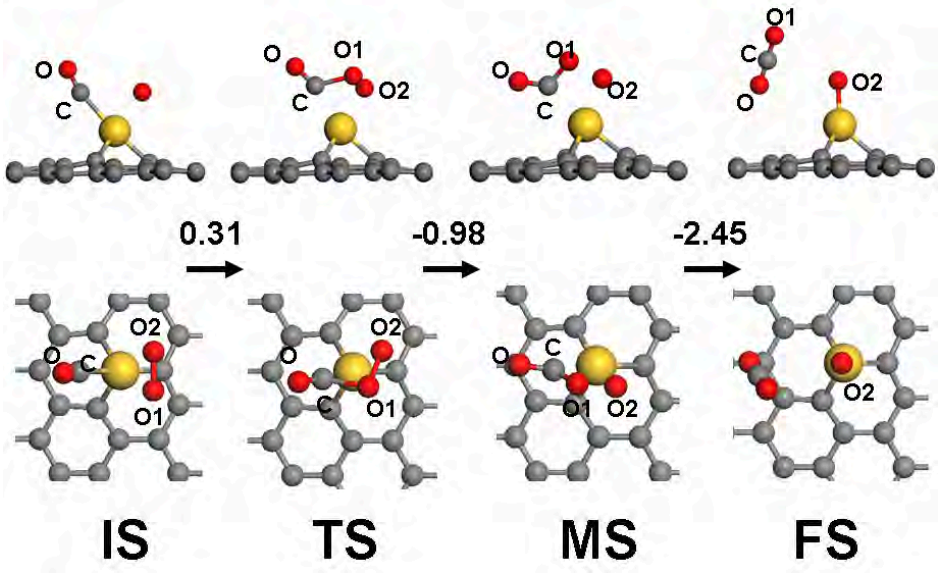


Figure 6.11: Local configurations of CO oxidation catalyzed by Au-graphene at various intermediate states, including the initial state, transition state, metastable state, and final state along MEP. Both side view (upper panel) and top view (lower view) are displayed. Color scheme is the same as in Fig. 6.4.

state is reached and O-O bond length in the O2-O1-C-O is expanded to 1.50 Å. After MS without an energy barrier, a $CO_2$ molecule is formed, leaving an atomic O adsorbed on the Au atom embedded in graphene, The $CO_2$ molecule can be easily desorbed at room temperature due to the weak interaction between $CO_2$ and Au-graphene ($\sim$ 0.1 eV).

After the first $CO_2$ molecule was formed, we checked whether an incoming CO could react with the remaining atomic O ($CO + O \rightarrow CO_2$) is conceivable through ER mechanism. It was found that a relatively small energy barrier of 0.18 eV, about half of the barrier for the first step ($CO + O_2 \rightarrow CO_2 + O$) is needed to activate this reaction, due to the high activity of the atomic O atom. On the basis of the above discussion, we

Table 6.5: Structural parameters for intermediate states along the MEP for the CO oxidation on Au-graphene: $CO + O_2 \rightarrow OOCO \rightarrow CO_2 + O$. IS, TS, MS and FS are displayed in Fig. 6.11.

| Intermediate State | IS | TS | MS | FS |
|---|---|---|---|---|
| d(C-O)(Å) | 1.139 | 1.172 | 1.207 | 1.178 |
| d(C-Au)(Å) | 2.231 | 2.147 | 2.148 | 4.063 |
| d(C-O1)(Å) | 2.755 | 1.694 | 1.355 | 1.173 |
| d(O1-O2)(Å) | 1.388 | 1.449 | 1.501 | 3.374 |
| d(O2-Au)(Å) | 2.175 | 2.144 | 2.081 | 1.849 |
| Φ(O-C-O1)(deg) | 117.2 | 121.0 | 122.8 | 180.0 |

conclude that CO oxidation can readily happen on Au-graphene at room temperature, which may be characterized as a two-step process: the LH mechanism initiates the first step ($CO + O_2 \rightarrow CO_2 + O$) followed by ER reaction of the second step ($CO + O \rightarrow CO_2$).

## 6.3 Chapter summary

In summary, in this chapter, via first principles calculations, we propose the use of metal-embedded graphene as a possible single-atom nanocatalyst with high performance.

We first investigated the structural and electronic structures of typical metal atom embedded graphene. Then, the adsorption of small gas molecules ($O_2$, CO, $NO_2$ and $NH_3$) on pristine graphene and graphene embedded by various transition metal elements were

systematically studied and discussed. Our calculations found that in general, the chemical reactivity of graphene can be significantly enhanced by the embedding of transition metals, leading to activation of adsorbed gas molecules, suggesting the great potential of this material for future applications. Among all kinds of transition metal elements, our study clearly shows that Ti and Au are best in improving the chemical reactivity of graphene towards $O_2$ activation.

By using Au-embedded graphene as model catalytic system and CO oxidation as a benchmark, we explored the reaction mechanism of CO oxidation. Results show that CO oxidation is likely to proceed with LH mechanism at the starting point with a low barrier of 0.31 eV, followed by the ER reaction with a much smaller energy barrier (0.18 eV), indicating that this reaction may occur at room temperature. The high catalytic activity of Au-graphene is attributed to the interaction of d orbitals of Au atom and the antibonding $2\pi^*$ orbital of $O_2$, in which electrons from Au-graphene populated to initially empty antibonding $2\pi^*$ of adsorbed $O_2$, leading to an enlarged of O-O bond. The proposed method transform inert graphene to a highly active material for single-atom catalyst, opening a new avenue to fabricate low-cost catalysts based on carbon. Detailed analysis of electronic structure and magnetic properties of these systems may be also useful in graphene-based gas sensing and spintronics.

# Chapter 7

# Conclusion remarks

To summarize, this thesis aimed to explore and understand supported metal nanocatalysis at an atomic scale by using theoretical approaches. The structural, electronic and catalytic properties of metal clusters deposited on oxides and carbonaceous nonmaterials were studied within the framework of density functional theory, in order to obtain a deep understanding of the catalytic mechanism. Novel and practical methodologies have been proposed to design new catalysts and control their catalytic performance.

First, we investigated the chemical reaction of CO oxidation catalyzed by transition metal oxide supported gold nanoclusters, and special attention was paid to the effects of metal-insulator transition on the adsorption, stabilization and catalytic activity of Au clusters. It is found that the Nb-doping induced MIT in $SrTiO_3$ substrate causes a dimensionality crossover of supported Au nanoclusters (three dimensional structure to two dimensional one), and at the same time, greatly enhances the stability and catalytic activity of these clusters. Underlying the predicted high catalytic activity of Au clusters

towards CO oxidation (reaction barrier $\sim$ 0.2 eV) is the MIT induced interaction between $O_2$ antibonding 2 $\pi$* orbital and Au conduction bands, leading to the population of electrons from Au to the antibonding orbital and chemical activation of $O_2$ molecule. Compared to other techniques such as tuning the thickness of the oxide substrate or applying an electric field, controlling MIT in oxide is of fundamental importance in physics and more practical in industrial implementation due to the mature technology in chemical doping. The present results may provide some insights into the fundamental properties of oxides and oxide-supported metal clusters, and we encourage experimental research in this direction.

Second, motivated by recent advancement in synthesis and characterization of two-dimensional graphene sheet, we studied graphene supported metal particles as nanocatalysts. Graphene itself is chemically inert due to the strong $sp^2$ and $\pi$ binding between carbon atoms in the graphene plane. Consequently, the supported metal clusters are highly mobile and tend to form bigger clusters, which is not wanted for real applications. Also, it is not possible to control the performance of catalytic activity through the underlying substrate due to the weak interaction. In current study, we propose to control the stabilization and catalytic activity of metal nanoclusters supported on graphene via tuning the mechanical strain in graphene. It is showed that a relatively modest tensile strain (10%) applied in graphene greatly increases the adsorption energies of various kinds of metal clusters under study by at least 100%, suggesting the strain-induced stabilization. By using $Au_{16}$ and $Au_8$ clusters on graphene as model catalysts for CO oxidation, it is found that the charge transfer between Au clusters and graphene can be efficiently tuned by strain, and reduces the reaction barrier of catalyzed CO oxidation from around 3.0 eV to less than 0.2 eV. This is the first report on using mechanical strain to control the

performance of heterogeneous nanocatalysts, and it also paves the way for the further development of mechano-chemistry, for which the focus is the interplay between the mechanical force and chemical reactions.

In addition, we studied CO oxidation catalyzed by $Au_8$ or $Pt_4$ clusters on graphene with defects. The simplest single-carbon-vacancy defect in graphene is found to play an essential role in anchoring the supported metal clusters and activating the $O_2$ molecule. The anchoring of the metal clusters is attributed to the strong interaction between the carbon-vacancy defect in graphene and the adsorbed metal clusters originating from the defect-induced hybridization of carbon 2p and Au/Pt 5d orbitals. Moreover, supported metal clusters are catalytic active towards $O_2$ due to electrons populated the anti-bonding $2\pi^*$ orbital of the molecule mainly from metal clusters and the metal/graphene interfacial region. Since the carbon-vacancy defect is inevitable in the experimental preparation of graphene sheets, results presented here may be useful in explaining recent experiments pertaining the enhanced electrocatalytic activity of Pt subnanoclusters in graphene surface,[43] and also valuable for the understanding of the defective graphene supported metal systems.

Finally, we have explored the adsorption of small gas molecules ($O_2$, CO, $NO_2$ and $NH_3$) on pristine and various transition-metal-embedded graphene to see whether the embedded metal may increase the chemical reactivity of graphene. The most stable adsorption geometry, energy, charge transfer, and magnetic moment of these molecules on graphene embedded with different transition metal elements are thoroughly discussed. Our calculations suggest that embedded transition metal elements in general can significantly enhance the interactions between gas molecules and graphene, and for applications of graphene-based catalysis, Ti and Au may be the best choices among all transition metal

elements. By using Au-graphene as model catalyst system and CO oxidation as a benchmark probe, we have studied the catalytic mechanism of this system. It is found that the first step of catalyzed CO oxidation is most likely to proceed with the Langmuir-Hinshelwood reaction ($CO + O2 \rightarrow OOCO \rightarrow CO_2 + O$), and the energy barrier is 0.31 eV. The second step of the oxidation would be the Eley-Rideal reaction ($CO + CO_2 + O$) with a much smaller energy barrier (0.18 eV). The activity of Au-graphene may be attributed to the electronic resonance among electronic states of CO, $O_2$, and the Au atom, particularly, among the d states of the Au atom and the antibonding $2\pi^*$ states of CO and $O_2$. The small loading of metal atoms, together with the high activity render metal-embedded graphene a novel single-atom heterogeneous catalyst towards CO oxidation. The proposed method transforms inert graphene to a highly active material, opening a new avenue to fabricate singe-atom nanocatalysts based mainly on carbon, which is of great significance from both scientific and technological point of view.

My research only focuses on the theoretical predictions. More experiments are needed to verify the theoretical results. It should also be noted that our predictions on supported metal nanocatalysts are based on ideal systems, thus external environment parameters such as pressure, moisture and light are excluded from our simulations. Moreover, regarding to the experimentally synthesized graphene, defects, curvature or strain may coexist in the system, so they may affect the properties of graphene simultaneously. Further research should be attempted to simulate the real experimental conditions to gain a deeper understanding of these systems. A direct extension of this work is to investigate the use of graphene derivatives, such as graphene oxide or hydrogenated graphene (graphane), as supports for metal nanocatalysts, because of their different physical and

chemical properties compared to pristine graphene. Currently the research of graphene-supported metal nanocatalysis is just at the beginning stage, more research work should be done before we can put graphene-based nanocatalysts into industrial applications.

In the long term, research will be conducted in the following several aspects: 1) Study complex metal clusters as nanocatalysts. Bimetallic nanoparticles, metal alloys and core-shell nanostructures will be investigated in detail as these materials show physical and chemical properties different from their monometallic counterparts. Another important direction is to investigate the catalytic properties of ligand-protected metal nanoparticles. As the present work mainly focuses on bare metal clusters that are prepared by physical methods (such as sputtering, physical vapor deposition, etc.), the structural and electronic properties of metal nanoparticles that are synthesized by wet chemical methods remain unknown. We will explore the effects of ligand that are commonly present during chemical synthesis, on the physical and chemical properties properties of metal nanoclusters. In particular, we will study the catalytic properties of thiolated Au clusters and their derivatives, nanostructures that are constructed by using these nanoclusters as building blocks, as well as ligand-protected metal cluster deposited on oxide as hybrid systems. 2) Investigate other typical materials as catalyst supports. In the present study, only oxides and graphene are chosen as model catalyst supports, and other important materials such as metal carbides, nitrides, MOF and biomaterials which have been mentioned in the Introduction part, have not been systematically studied. Future work will be extended to these materials and investigate their applications in catalysis. 3) Explore new experimental techniques to control the catalytic performance of nanocatalysts. These methods include but are not limited to charging, ligand-exchanging, heat, pressure and electric/magnetic field. We expect results presented in this thesis and the

proposed research to shed light in the future design of novel materials with versatile functionalities in heterogeneous catalysis.

# References


[1] J. A. Moulijn, P. W. N. M. van Leeuwen, R. A. van Santen, "Catalysis: An integrated approach to homogeneous, heterogeneous and industrial catalysis", Elsevier, Amsterdam (1993).

[2] P. T. Anastas and J. C. Warner, "Greem Chemistry: Theory and Practice", Oxford University Press, Oxford (1998).

[3] P. T. Anastas, C. A. Farris,"Benign by Design: Alternative Synthetic Design for Pollution Prevention", ACS Sym. Ser. nr. 577, American Chemcial Society Society, Washington DC (1994).

[4] R. A. Sheldon, C. R. Acad. Sci. Paris, IIc. Chimie/Chemistry, **3**, 541 (2000)

[5] C. H. Christensen, J. K. Nørskov, Science **327**, 278 (2010).

[6] J. R. Anderson, "Structure of metallic catalysts", Academic Press, London (1975).

[7] V. Ponec and G. C. Bond, "Catalysis by metals and alloys", Studies in surface science and catalysis Vol. 95. Elsevier, Amsterdam (1995).

[8] G. Ertl, H. Knotziger, F. Schuth and J. Weitkamp, "Handbook of Heterogeneous Catalysis", Wiley, NY, 2nd edn (2008).

[9] N. Mizuno and M. Misono, Chem. Rev. **98**, 199 (1998).

[10] L. Canali and D. C. Sherrington, Chem. Soc. Rev. **28**, 85 (1999).

[11] H. J. Freund, Sur. Sci. **500**, 271 (2002).

[12] M. Haruta, T. Kobayashi, H. Sano, N. Yamada, Chem. Lett. **2**, 405 (1987).

[13] Q. Fu, H. Saltsburg and M. Flytzani-Stephanopoulos, Science **301**, 935 (2003).

[14] D. I. Enache, J. K. Edwards, P. Landon, B. Solsona-Espriu, A. F. Carley, A. A. Herzing, M. Watanabe, C. J. Kiely, D. W. Knight and G. J. Hutchings, Science **311**, 362 (2006).

[15] A. Abad, P. Concepcion, A. Corma and H. Garcia, Angew. Chem.-Int. Edit. **44**, 4066 (2005).

[16] J. K. Edwards, B. Solsona, E. N. N, A. F. Carley, A. A. Herzing, C. J. Kiely and G. J. Hutchings, Science **323**, 1037 (2009).

[17] A. S. K. Hashmi and G. J. Hutchings, Angew. Chem.-Int. Edit. **45**, 7896 (2006).

[18] G. Kyriakou, S. K. Beaumont, S. M. Humphrey, C. Antonetti and R. M. Lambert, ChemCatChem **2**, 1444 (2010).

[19] J. C. Fierro-Gonzalez and B. C. Gates, Chem. Soc. Rev. **37**, 2127 (2008).

[20] Z. P. Liu, S. J. Jenkins and D. A. King, Phys. Rev. Lett. **94**, 196102 (2005).

[21] B. Yoon, H. Häkkinen, U. Landman, A. S. Worz, J. M. Antonietti, S. Abbet, K. Judai and U. Heiz, Science **307**, 403 (2005).

[22] D. Ricci, A. Bongiorno, G. Pacchioni and U. Landman, Phys. Rev. Lett. **97**, 036106 (2006).

[23] M. S. Chen, D. W. Goodman, Chem. Soc. Rev. **37**, 1860 (2008).

[24] M. Valden, X. Lai, D. W. Goodman, Science **281**, 1647 (1998).

[25] M. Haruta, N. Yamada, T. Kobayashi, S. Iijima, J. Catal. **115**, 301 (1989).

[26] M. M. Schubert, S. Hackenberg, A. C. van Veen, M. Muhler, V. Plzak, R. J. Behm, J. Catal. **197**, 113 (2001)

[27] S. Carrettin, P. Concepción, A. Corma, J. M. L. Nieto, V. F. Puntes, Angew. Chem. Int. Ed. **43**, 2538 (2004).

[28] J. A. Rodriguez, P. Liu, F. Vines, F. Illas, Y. Takahashi, K. Nakamura, Angew. Chem. Int. Ed. **47**, 6685 (2008).

[29] R. B. Levy and M. Boudart, Science **181**, 547 (1973).

[30] E. Florez, T. Gomez, J. A. Rodriguez, F. Illas, Phys. Chem. Chem. Phys. **13**, 6865 (2011)

[31] E. Florez, F. Vines, J. A. Rodriguez, F. Illas, J. Chem. Phy. **130**, 244706 (2009).

[32] J. A. Rodriguez, F. Vines, F. Illas, J. Chem. Phys. **127**, 211102 (2007).

[33] A. J. Bird, in: A. B. Stiles, "Catalyst Supports and Supported Catalysts", p. 107, Butterworths, Boston (1987).

[34] O. Wohler F. von Sturm, E. Wege, H. von Kienle, M. Voll, P. Kleinschmit, in: W. Gerhartz, "Ullmann's Encyclopaedia of Industrial Chemistry", p. 95, vol. A5, VCH, Weinheim (1986).

[35] W. Blyth, “Chemical Economics Handbook-Graphite”, SRI International (1997)

[36] P. Gallezot, S. Chaumet, A. Perrard, P. Isnard, J. Catal. **168**, 104 (1997).

[37] M. S. Mauter, M. Elimelech, Environ. Sci. Technol. **42**, 5843 (2008).

[38] H. W. Kroto, J. R. Heath, S. C. O’Brien, R. F. Curl, R. E. Smalley, Nature **318**, 162 (1985).

[39] S.Iijima, Nature **354**, 56 (1991).

[40] K. S. Novoselov, A. K. Geim, S. V. Morozov, D. Jiang, Y. Zhang, S. V. Dubonos, I. V. Grigorieva, and A. A. Firsov, Science **306**, 666 (2004).

[41] K. S. Novoselov, A. K. Geim, S. V. Morozov, D. Jiang, M. I. Katsnelson, I. V. Grigorieva, S. V. Dubonos, A. A. Firsov, Nature **438**, 197 (2005).

[42] Y. B. Zhang, Y. W. Tan, H. L. Stormer, P. Kim, Nature **438**, 201 (2005).

[43] E. Yoo, T. Okata, T. Akita, M. Kohyama, J. Nakamura, I. Honma, Nano Lett. **9**, 2255 (2009).

[44] E. Ganz, K. Sattler and J. Clarke, Surf. Sci. **219**, 33 (1989).

[45] T. Irawan, I. Barke and H. Hövel, Appl. Phys. A: Mater. Sci. Process. **80**, 929 (2005).

[46] Y. J. Gan, L. T. Sun, F. Banhart, Small **4**, 587 (2008).

[47] Z. Zhou, F. Gao, D. W. Goodman, Sur. Sci. **604**, 1071 (2010).

[48] I. Cabria, M. J. Lopez, J. A. Alonso, Phys. Rev. B **81**, 035403 (2010).

[49] M. Eddaoudi, D. B. Moler, H. L. Li, B. L. Chen, T. M. Reineke, M. O'Keeffe, O. M. Yaghi, ACC. Chem. Res. **34**, 319 (2001).

[50] H. L. Li, M. Eddaoudi, M. O'Keeffe, O. M. Yaghi, Nature **402**, 276 (1999).

[51] S. L. James, Chem. Soc. Rev. **32**, 276 (2003).

[52] D. Farrusseng, S. Aguado, C. Pinel, Angew. Chem. Int. Ed. **48**, 7502 (2009).

[53] J. Lee, O. K. Farha, J. Roberts, K. A. Scheidt, S. T. Nguyen, J. T. Hupp, Chem. Soc. Rev. **38**, 1450 (2009).

[54] F. X. Llabrés i Xamena, O. Casanova, R. Galiasso Tailleur, H. Garcia, A. Corma, J. Catal. **255**, 200 (2008).

[55] T. Uemura, R. Kitaura, Y. Ohta, M. Nagaoka and S. Kitagawa, Anew. Chem. Int. Ed. **45**, 4112 (2006).

[56] S. Hermes, M. K. Schroeter, R. Schmid, L. Khodeir, M. Muhler, A. Tissler, R. W. Fischer and R. A. Fischer, Angew. Chem. Int, Ed. **44**, 6237 (2007).

[57] H. L. Jiang, B. Liu, T. Akita, M. Haruta, H. Sakurai and Q. Xu, J. Am. Chem. Soc. **131**, 11302 (2009).

[58] J. M. Campelo, D. Luna, R. Luque, J. M. Marinas, A. A. Romero, ChemSusChem **2**, 18 (2009).

[59] S. J. Tauster, S. C. Fungm R. T. K. Baker, J. A. Horsley, Science **211**, 1121 (1981).

[60] S. J. Tauster, Acc. Chem. Res. **20**, 389 (1987).

[61] Y. W. Chung, G. X. Xiong, C. C. Kao, J. Catal. **85**, 237 (1984).

[62] M. Bowker, P. Stone, P. Morrall, R. Smith, R. Bennett, N. Perkins, R. Kvon, C. Pang, E. Fourre, M. Hall., J. Catal. **234**, 172 (2005).

[63] M. S. Chen, D. W. Goodman, Science **306**, 5694 (2004).

[64] N. Lopez, J. K. Nørskov, Sur. Sci. **515**, 175 (2002).

[65] G. Pacchioni, S. Sicolo, C. D. Valentin, M. Chiesa and E. Giamello, J. Am. Chem. Soc. **130**, 8690 (2008).

[66] A. C. Gluhoi, X. Tang, P. Margineau, B. E. Nieuwenhuys, Top. Catal. **39**, 101 (2006).

[67] M. A. Brown, E. Carasco, M. Sterrer, H. J. Freund, J. Am. Chem. Soc. **132**, 4064 (2010).

[68] M. A. Brown, Y. Fujimori, F. Ringleb, X. Shao, F. Stavale, N. Nilius, M. Sterrer, H. J. Freund, J. Am. Chem. Soc. **133**, 10668 (2011).

[69] C. H. Ahn, K. M. Rabe, J. M. Triscone, Science **303**, 488 (2004).

[70] C. G. Granqvist, Sol, Energy Mater. Sol. Cells **91**, 1529 (2007).

[71] L. Giordano and G. Pacchioni, ACC. Chem. Res. **44**, 1244 (2011).

[72] D. Ricci, A. Bongiorno, G. Pacchioni, U.Landman, Phys. Rev. Lett. **97**, 036106 (2006).

[73] C. Zhang, B. Yoon and U. Landman, J. Am. Chem. Soc. **129**, 2228 (2007).

[74] M. Sterrer, T. Risse, M. Heyde, H. P. Rust, H. J. Freund, Phys. Rev. Lett. **98**, 206103 (2007).

[75] X. Lin, N. Nilius, H. J. Freund, M. Walter, P. Frondelius, K. Honkala, H. Häkkinen, Phys. Rev. Lett. **102**, 206801 (2009).

[76] B. Yoon, U. Landman, Phys. Rev. Lett. **100**, 056102 (2008).

[77] C. Harding, V. Habibpour, S. Kunz, A. N. S. Farnbacher, U. Heiz, B. Yoon, U. Landman, J. Am. Chem. Soc. **131**, 538 (2009).

[78] J. B. Park, J. Graciani, J. Evans, D. Stacchiola, S. Ma, P. Liu, A. Nambu, J. F. Sanz, J. Hrbek and J. A. Rodriguez, Proc. Natl. Acad, Sci, U. S. A. **106**, 4975 (2009).

[79] A. Bongiorno and U. Landman, Phys. Rev. Lett. **95**, 106102 (2005).

[80] O. Lopez-Acevedo, K. A. Kacprzak, J. Akola, and H. Hakkinen, Nat. Chem. **2**, 329 (2010).

[81] H. J. Freund, G. Meijer, M. Scheffler, R. Schlögl, M. Wolf, Angew. Chem. Int. Ed. **50**, 2 (2011).

[82] M. Born and J. R. Oppenhermer, Ann. Physik **84**, 457 (1927).

[83] D. R. Hartree, Proc. Camb. Phil. Sco. **24**, 89 (1928).

[84] M. C. Payne, M. P. Teter, D. C. Allan, T. A. Arias and J. D. Joannopoulos. Rev. Mod. Phys. **64**, 1045 (1992); and references therein.

[85] P. HOHENBERG and W. KOHN, Phys. Rev. B **136**, 864 (1964).

[86] W. KOHN and L. SHAM, Phys. Rev. **140**, A1133 (1965).

[87] I. ROBERTSON, M. PAYNE, and V. HEINE, J. Phys.-Condes. Matter **3**, 8351 (1991).

[88] J. PERDEW, J. CHEVARY, S. VOSKO, K. JACKSON, M. PEDERSON, D. SINGH, and C. FIOLHAIS, Phys. Rev. B **46**, 6671 (1992).

[89] J. P. Perdew and Y. Wang, Phys. Rev. B **45**, 13244 (1992).

[90] M. D. Segall, J. D. Philip Lindan, M. J. Probert, C. J. Pickard, P. J. Hasnip, S. J. Clark and M. C. Payne1 J. Phys.: Condens. Matter **14**, 2717 (2002)

[91] H. MONKHORST and J. PACK, Phys. Rev. B **13**, 5188 (1976).

[92] J. C. Phillips, Phys. Rev. **112**, 685 (1958).

[93] M. L. Cohen and V. Heine, Solid State Phys. **24**, 37 (1970).

[94] M. T. Yin and M. L. Cohen, Phys. Rev. B **25**, 7403 (1982).

[95] D. J. Singh, L. Nordstrom, "Planes, Pseudopotentials and the LAPW Method", Springer (2006).

[96] G. B. Bachelet, D. R. Hamann and M. Schluter, Phys. Rev. B **26**, 4199 (1982).

[97] D. Vanderbilt, Phys, Rev. B **41**, 7892 (1990).

[98] P. E. Blöchl, Phys. Rev. B **50**, 17953 (1994).

[99] N. A. W. Holzwarth, G. E. Matthews, R. B. Dunning, A. R. Tackett and Y. Zeng, Phys. Rev. B **55** 2005 (1997).

[100] M. P. Teter, M. C. Payne, and D. C. Allan, Phys. Rev. B **40**, 1225 (1989)

[101] C. Wert and C. Zener, Phys. Rev. **76**, 1169 (1949).

[102] G. H. Vineyard, J. Phys. Chem. Solids **3**, 121 (1957).

[103] B. Hammer, K. W. Jacobsen and J. K. Nørskov, Phys. Rev. Lett. **69**, 13 (1992).

[104] A. Alavi, P. Hu, T. Deutsch, P. L. Silvestrelli and J. Hutter, Phys. Rev. Lett. **80**, 16 (1998).

[105] H. Jósson, G. Mills and K. W. Jacobsen, "Classical and Quantum Dynamics ub Condensed Phase Simulations", edited by B. J. Berne, G. Ciccotti and D. F. Coker, p. 385, World Scientific, Singapore (1998).

[106] G. Henkelman, B. P. Uberuaga and H. Jósson, J. Chem. Phys. **113**, 9901 (2000).

[107] G. Henkelman and H. Jósson, J. Chem. Phys. **113**, 9978 (2000).

[108] G. Kresse and J. Hafner, Phys. Rev. B **49**, 14251 (1994).

[109] M. Imada, A. Fujimori, Y. Tokura, Rev. Mod. Phys. **70**, 1039 (1998).

[110] C. H. Yang, J. Seidel, S. Y. Kim, P. B. Rossen, P. Yu, M. Gajek, Y. H. Chu, L. W. Martin, M. B. Holcomb, Q. He, P. Maksymovych, N. Balke, S. V. Kalinin, A. P. Baddorf, S. R. Basu, M. L. Scullin and R. Ramesh, Nat. Mater. **8**, 485 (2009).

[111] Kozuka, Y,; Kim, M.; Bell, C.; Kim, B. G.; Hikita, Y.; Hwang, H. Y. Nature **462**, 487 (2009).

[112] K. Ueno, S. Nakamura, H. Shimotani, A. Ohtomo, N. Kimura, T. Nojima, H. Aoki, Y. Iwasa and M. Kawasaki, Nat. Mater. **7**, 855 (2008).

[113] H. Hidaka, I. Ando, H. Kotegawa, T. C. Kobayashi, H. Harima, M. Kobayashi, H. Sugawara, H. Sata, Phys. Rev. B **71**, 073102 (2005).

[114] K. Byczuk, W. Hofstetter and D. Vollhardt, Phys. Rev. Lett. **94**, 056404 (2005).

[115] J. F. Schooley, W. R. Hosler, E. Ambler, J. H. Becker, M. L. Cohen abd C. S. Koonce, Phys. Rev. Lett. **14**, 305 (1965).

[116] Y. Kozuka, M. Kim, C. Bell, B. G. Kim, Y. Hikita, H. Y. Hwang, Nature **462**, 487 (2009).

[117] O. N. Tufte and P. W. Chapman, Phys. Rev. **155**, 796 (1967).

[118] W. Meevasana, P. D. C. King, R. H. He, S. K. Mo, M. Hashimoto, A. Tamai, P. Songsiriritthigul, F. Baumberger, Z. X. Shen, Nat. Mater. **10**, 114 (2011).

[119] A. Spinelli, M. A. Torija, C. Liu, C. Jan and C. Leighton, Phys. Rev. B **81**, 155110 (2010).

[120] Z. Wang, S. Tsukimoto, M. Saito, and Y. Ikuhara, Appl. Phys. Lett. **94**, 252103 (2009).

[121] M. S. J. Marshall, D. T. Newell, D. J. Payne, R. G. Egdell, and M. R. Castell, Phys. Rev. B **83**, 035410 (2011).

[122] J. Son, P. Moetakef, B. Jalan, O. Bierwagen, N. J. Wright, R. Engel-Herbert, S. Stemmer, Nat. Mater. **9**, 482 (2010).

[123] Y. K. Han, J. Chem. Phys. **124**, 024316 (2006).

[124] J. P. Perdew, K. Burke, M. Ernzerhof, Phys. Rev. Lett. **77**, 3865 (1996).

[125] I. V. Solovyev and P. H. Dedrichs, Phys. Rev. B, **49**, 6736 (1994).

[126] M. Cardona, Phys. Rev. **140**, A651 (1965).

[127] C. Zhang, C. L. Wang, J. C. Li, K. Yang, Y. F. Zhang, Q. Z. Wu, Mater. Chem. Phys. **107**, 215 (2008).

[128] A. S. Hamid, Appl. Phys. A-Mater. Sci. Process. **97**, 829 (2009).

[129] F. Lin, S. Y. Wang, F. W. Zheng, G. Zhou, J. Wu, B. L. Gu, W. H. Duan, Phys. Rev. B, **79**, 035311 (2009).

[130] A. A. Herzing, C. J. Kiely, A. F. Carley, P. Landon, G. J. Hutchings, Science **321**, 1331 (2008).

[131] T. Pabisiak and A. Kiejna, Phys. Rev. B, **79**, 085411 (2009).

[132] R. F. W. Bader, "Atoms in Molecules: A Quantum Theory", Oxford University Press, New York (1900).

[133] R. Coquet, K. L. Howard and D. J. Willock,, Chem. Soc. Rev. **37**, 2046 (2008).

[134] L. M. Molina and B. Hammer, Appl. Catal. A, **291**, 21 (2005).

[135] J. M. Valles, A. E. White, K. T. Short, R. C. Dynes, J. P. Garno, A. F. J. Levi, M. Anzlowar, K. Baldwin, Phys. Rev. B **39**, 11599 (1988).

[136] R. Y. Gu, Z. D. Wang, C. S. Ting, Phys. Rev. B. **67**, 153101 (2003).

[137] H. Hidaka, T. Ando, H. Kotegawa, T. C. Kobayashi, H. Harima, M. Kobayashi, H. Sugawara, H. Sata, Phys. Rev. B. **71**, 073102 (2005).

[138] J. R. Kitchin, J. K. Nøskov, M. A. Barteau and J. G. Chen, J. Chem. Phys. **120**, 21 (2004).

[139] M. Mavrikakis, B. Hammer, J. K. Nøskov, Phys. Rev. Lett. **81**, 2819 (1998).

[140] B. Hammer and J. K. Nøskov, Adv. Catal. **45**, 71 (2000).

[141] M. Gsell, P. Jakob and D. Menzel, Science **280**, 717 (1998).

[142] J. H. Sinfelt, “Bimetallic Catalysts: Discoveries, Concepts and Applications”, Wiley, New York (1983).

[143] L. A. Kibler, A. M. EI-Aziz, R. Hoyer and D. M. Kolb, Angew. Chem. Int. Ed. **44**, 2080 (2005).

[144] A. Nilekar, Y. Xu, J. Zhang, M. Vukmirovic, K. Sasaki, R. Adzic and M. Mavrikakis, Top. catal. **46**, 276 (2007).

[145] L. A. Kibler, A. M. El-Aziz, R. Hoyer, D. M. Kolb, Angew. Chem. Int. Ed. **44**, 2080 (2005).

[146] P. Strasser, S. Koh, T. Anniyev, J. Greeley, K. More, C. Yu, Z. liu, S. Kaya, D. Nordlund, H. Ogasawara, M. F. Toney and A. Nilsson, Nat. Chem. **2**, 454 (2010).

[147] S. Alayoglu, A. V. Nilekar, M. Mavrikakis and B. Eichhorn, Nat. Mater. **7**, 333 (2008).

[148] Y. Xu, A. V. Ruban and M. Mavrikakis, J. Am. Chem. Soc. **126**, 4717 (2004).

[149] Y. Suo, L. Zhang and J. Lu, Angew. Chem. Int. Ed. **46**, 2862 (2007).

[150] K. S. Kim, Y. Zhao, H. Jang, S. Y. Lee, J. M. Kim, K. S. Kim, J-H. Ahn, P. Kim, J-Y. Choi, B-H. Hong, Nature **457**, 706 (2009).

[151] C. Lee, X. Wei, J. W. Kysar, J. Hone, Science **321**, 385 (2008).

[152] F. Guinea, M. I. Katsnelson, A. K. Geim, Nat. Phys. **6**, 30 (2009).

[153] V. M. Pereira, A. H. C. Neto, Phys. Rev. Lett. **103**, 046801 (2009).

[154] J. Wang, Z. Liu, Z. Liu, AIP ADVANCES **2**, 012103 (2012).

[155] N. Wei, L. Xu, H. Q. Wang and J. C. Zheng, Nanotechnology **22**, 105705 (2011).

[156] S. Vajda, M. J. Pellin, J. P. Greeley, C. L. Marshall, L. A. Curtiss, G. A. Ballentine, J. W. Elam, S. Catillon-Mucherie, P. C. Redfern, F. Mehmood, P. Zapol, Nat. Mater. **8**, 213 (2009).

[157] S. B. H. Bach, D. A. Garland, R. J. Vanzee, W. Weltner, J. Chem. Phys. **87**, 869 (1987).

[158] V. D'Anna, D. Duca, F. Ferrante, G. La Manna, Phys. Chem. Chem. Phys. **12**, 1323 (2009).

[159] P. J. Roach, W. H. Woodward, A. W. Castleman, A. C. Reber, S. N. Khanna, Science **323**, 492 (2009).

[160] Q. Sun, Q. Wang, P. Jena, Y. Kawazoe, J. Am. Chem. Soc. **127**, 14582 (2005).

[161] P. O. Krasnov, F. Ding, A. K. Singh and B. I. Yakobson J. Phys. Chem. C. **111**, 17977 (2007).

[162] S. Bulusu, X. Li, L. S. Wang, X. C. Zeng, Proc. Natl. Acad. Sci. U. S. A. **103**, 8326 (2006).

[163] Y. Pei, N. Shao, Y. Gao, X. C. Zeng, ACS Nano **4**, 2009 (2010).

[164] I. Gierz, C. Riedl, U. Starke, C. R. Ast, K. Kern, Nano Lett. **8**, 4603 (2008).

[165] O. Ü. Aktürk and M. Tomak, Phys. Rev. B **80**, 085417 (2009).

[166] Y. H. Lu, W. Chen, Y. P. Feng, P. M. He, J. Phys. Chem. B **113**, 2 (2009).

[167] J. T. Sun, Y. H. Lu, W. Chen, Y. P. Feng, A. T. S. Wee, Phys. Rev. B **81**, 155403 (2010).

[168] G. Giovannetti, P. A. Khomyakov, G. Brocks, V. M. Karpan, J. van den Brink and P. J. Kelly, Phys. Rev. Lett. **101**, 026803 (2008).0

[169] L. M. Molina and B. Hammer, J. Chem. Phys. **123**, 161104 (2005).

[170] M. Zhou, Y. H. Lu, C. Zhang and Y. P. Feng, Appl. Phys. Lett. **97**, 103109 (2010).

[171] S. Bhandary, S. Ghosh, H. Herper, H. Wende, O. Eriksson, B. Sanyal, Phys. Rev. Lett. **107**, 257202 (2011).

[172] Elton J. G. Santos, A. Ayuela, D. Sanchez-Portal, J. Phys. Chem. C **116**, 1174 (2012).

[173] C. R. Hickenboth, J. S. Moore, S. R. White, N. R. Scottos, J. Baudry, S. R. Wilson, Nature **446**, 423 (2007).

[174] M. T. Ong, J. Leiding, H. Tao, A. M. Virshup, T. J. Martinez, J. Am. Chem. Soc. **131**, 6377 (2009).

[175] C. Kittel, "Introduction to Solid State Physics", John Willey and Sons, New York (2005).

[176] S. Bae, H. K. Kim, Y. Lee, X. Xu, J. S. Park, Y. Zheng, J. Balakrishnan, T. Lei, H. R. Kim, Y. I. Song et al., Nat. Nanotech. **5**, 574 (2010).

[177] C. Berger, Z. Song, T. Li, X. Li, A. Y. Ogbazghi, R. Feng, Z. Dai, A. N. Marchenkov, E. H. Conrad, P. First et al., J. Phys. Chem. B **108**, 19912 (2004).

[178] C. Berger, Z. Song, X. Li, X. Wu, N. Brown, C. Naud, D. Mayou, T. Li, J. Hass, A. N. Marchenkov et al., Science **312**, 1191 (2006).

[179] N. T. Cuong, A. Sugiyama, A. Fujiwara, T. Mitani, D. H. Chi, Phys. Rev. B **79**, 235417 (2009).

[180] Z. W. Wang, R. E. Palmer, Nanoscale **4**, 4947 (2012).

[181] G. D. lee, C. Z. Wang, E. Yoon, N. M. Hwang, D. Y. Kim, K. M. Ho, Phys. Rev. lett. **95**, 205501 (2005).

[182] O. Cretu, A. V. Krasheninnikov, J. A. Rodriguez-Manzo, L. Sun, R. M. Nieminen, F. Banharf, Phys. Rev. Lett. **105**, 196102 (2010).

[183] A. V. Krasheninnikov, R. M. Nieminen, Theor. Chem. Acc. **129**, 625 (2011).

[184] J. Lahiri, Y. Lin, P. Bozkurt, I. Oleynik and M. Batzill, Nat. Nanotech. **5**, 326 (2010).

[185] Y. R. Yang, Y. Xiao, W. Ren, X. H. Yan and F. M. Pan, Phys. Rev. B **84**, 195447 (2011).

[186] S. Malola, H. Häkkinen, P. Koskinen, Phys. Rev. B **81**, 165447 (2010).

[187] K. Kim, Z. Lee, W. Regan, C. Kisielowski, M. F. Crommie and A. Zettl, ACS Nano, **5**, 2142 (2011).

[188] A. K. Geim, Science **324**, 1530 (2009).

[189] A. Hashimoto, K. Suenaga, A. Gloter, K. Urita, S. Iijima, Nature **430**, 870 (2004).

[190] M. H. Gass, U. Bangert, A. L. Bleloch, P. Wang, R. R. Nair, A. K. Geim, Nat. Nanotech. **3**, 676 (2008).

[191] J. C. Meyer, C. Kisielowski, R. Erni, M. D. Rossell, M. F. Crommie, A. Zettl, Nano Lett. **8**, 3582 (2008).

[192] J. H. Warner, M. H. Rümmeli, L. Ge, T. Gemming, B. Montanari, N. M. Harrison, B. Büchner, G. A. D. Briggs, Nat. Nanotech. **4**, 500 (2009).

[193] M. M. Ugeda, I. Brihuega, F. Guinea, J. M. Gómez-Rodríguez, Phys. Rev. Lett. **104**, 096804 (2010).

[194] A. J. Lu, B. C. Pan, Phys. Rev. Lett. **92**, 105504 (2004).

[195] H. T. Wang, Q. X. Wang, Y. C. Cheng, K. Li, Y. B. Yao, Q. Zhang, C. Z. Dong, P. Wang, U. Schwingenschlögl, W. Yang, X. X. Zhang, Nano Lett. **12**, 141 (2012).

[196] Y. Lei, F. Mehmood, S. Lee, J. Greeley, B. Lee, S. Seifert, R. E. Winans, J. W. Elam, R. J. Meyer, P. C. Redfern, D. Teschner, R. Schlögl, M. J. Pellin, L. A. Curtiss and S. Vajda, Science **328**, 224 (2010).

[197] A.V. Krasheninnikov, P.O. Lehtinen, A.S. Foster, P. Pyykko and R. M. Nieminen, Phys. Rev. Lett. **102**, 126807 (2009).

[198] B. Delley, J. Chem. Phys. **92**, 508 (1990).

[199] B. Delley, J. Chem. Phys. **113**, 7756 (2000).

[200] J. G. Guan, P. Duffy, J. T. Carter, D. P. Chong, K. C. Casida, M. E. Casida and M. Wrinn, J. Chem. Phys. **98**, 4753 (1993).

[201] A. Hellman, B. Razaznejad and B. I. Lundqvist, Phys. Rev. B **71**, 205424 (2005).

[202] A. Hellman and H. Gronbeck, J. Phys. Chem. C **113**, 3674 (2009).

[203] G.T. Babcock and M. Wikstrom, Nature **356**, 301 (1992).

[204] O. Leenaerts, B. Partoens, F. M. Peeters, Phys. Rev. B **77**, 125416 (2008).

[205] T. Ueda, M. M. H. Bhuiyan, H. Norimatsu, S. Katsuki, T. Ikegami, F. Mitsugi, Physica E **40**, 2272 (2008).

[206] M. G. Stachiotti, Phys. Rev. B **79**, 115405 (2009).

# Theoretical Understanding and Design of Supported Metal Heterogeneous Nanocatalysts

**MIAO ZHOU**

**NATIONAL UNIVERSITY OF SINGAPORE**

**2012**